KERNFORSCHUNGSANLAGE JÜLICH
GESELLSCHAFT MIT BESCHRÄNKTER HAFTUNG
Institut für Festkörperforschung

Investigation of the scattering of conduction electrons in copper from interstitial hydrogen using the de Haas-van Alphen effect

by

W. Wampler

Jül - 1300
Mai 1976

Als Manuskript gedruckt

Investigation of the scattering of conduction electrons in copper from interstitial hydrogen using the de Haas-van Alphen effect

by

W. Wampler

D 82 (Diss. T. H. Aachen)

Contents

§1 Introduction

Several years ago evidence from measurement of transport properties in dilute alloys indicated the existence of considerable anisotropy in the conduction electron scattering rate over the Fermi surface, and that the anisotropy was different for different types of defects /3.3/. In more recent years measurement of the dHvA effect has emerged as a useful technique for investigating scattering from lattice defects in metals. It has been shown /2.25/ that the lifetime measured in dHvA experiments is to a good approximation temperature independent, and therefore is due only to impurity scattering. For metals for which the Fermi surface is known in some detail the dHvA effect can be used to determine local values for the electronic lifetime $\tau(\underline{k})$ over the Fermi surface. Furthermore, dHvA lifetimes can be obtained relatively easily from scattering calculations since they are given by the transition probability between Bloch states. A comparison between theory and experiment is therefore relatively easy. In contrast the transport coefficients involve integrals over the Fermi surface and before theory can be compared with experimental results the Boltzmann equation must be solved. This often requires an approximation involving a transport relaxation time which is not the same as the dHvA lifetime.

dHvA investigations of local scattering rates for substitutional defects in noble metals have recently been reported in the literature /5.6, 5.7/ and considerable anisotropy in the scattering rate has been found. The availability of this information has stimulated efforts to develop a suitable theory to describe the scattering of conduction electrons from lattice defects /5.16, 5.13, 5.14, 2.20/.

In order to provide further experimental information it was decided to investigate the scattering rates for hydrogen in copper by means of dHvA measurements. Hydrogen in copper is probably one of the simplest impurities from the theoretical standpoint since the potential for hydrogen can be more easily cal-

culated than for other impurities, and the band structure of copper is relatively well known. Also since hydrogen is an interstitial defect it is expected to have a different scattering anisotropy than substitutional defects.

This experiment can provide information which should lead to a better understanding of the electronic properties of defects in metals, and in particular interstitial defects. The behavior of hydrogen in metals has recently received much attention because of its importance in new technological developments such as reactor materials and the use of hydrogen as a fuel. A better theoretical understanding of hydrogen in metals therefore has important practical applications.

Chapter 2 discusses the physics of the dHvA effect and shows how it can be used to determine the Fermi surface geometry, the Fermi velocities and the local scattering rates. Chapter 3 describes how the Dingle temperature measurements were made and discusses some of the possible pitfalls which could lead to unreliable measurements. The way in which the samples were prepared is described as well in chapter 3. Also discussed here are some aspects of the metalurgical behavior of hydrogen in copper which are relevant to the sample preparation such as solubility, diffusion, precipitation, and trapping at impurities. The experimental results are presented in chapter 4. In chapter 5 the local scattering rates are determined from the results. These are then compared with lifetimes from previously reported measurements on substitutional impurities in noble metals. The experimental results are found to be in excellent agreement with a recent calculation of the scattering rates for hydrogen in copper by Huisman and Weiss /5.8/. The data is also analysed in terms of phase shifts using the Greens function theory of Holtzworth and Lee /5.12/ for scattering from interstitials.

§2 The de Haas-van Alphen effect (dHvA)

In this section the effect of a magnetic field on the motion of the conduction electrons in a metal is discussed. The oscillatory variation of the magnetization of a metal with field (de Haas-van Alphen effect) is discussed and the effects of temperature and finite electronic lifetimes on the dHvA effect are considered. From the Lifshitz-Kosevich expression it is shown how the dHvA effect can be used to obtain information about the electronic states at the Fermi energy.

2.1 The Lifshitz-Kosevich formulation of the dHvA effect

The first formulation of an expression for the amplitude of the oscillatory magnetization of the conduction electrons for metals having a Fermi surface of arbitrary shape was due to Lifshitz and Kosevich /2.1/. An excellent review of this derivation is given by Gold /2.2/. The main physical aspects of this theory can be illustrated semiclassically in the following way. In the absence of a magnetic field $\underline{B}$ the conduction electron eigenstates in a perfect metallic crystal can be labelled by a wave vector $\underline{k}$ and a spin quantum number s. The effect of a magnetic field is to redistribute the states that can be occupied by the conduction electrons. The Lorentz force describes how an electron state $\underline{k}$ changes with time in a magnetic field.

$$\hbar\dot{\underline{k}} = e\underline{v} \times \underline{B} = e\dot{\underline{r}} \times \underline{B} \qquad (2.1)$$

$\underline{v}(\underline{k})$ is the electron velocity in the state $\underline{k}$ and $\underline{B} = \mu_o(\underline{H} + \underline{M})$ (see footnote). The component of motion parallel to the field $\underline{B}$

The SI system of units based on the meter, kilogram, second and ampere is used throughout this work. Here $\mu_o = 4\pi \times 10^{-7}$ newton (ampere)$^{-2}$ is the permeability of free space.

is unaffected by the field. Since a field constant in time does not do work on the electron, the electron moves on a path of constant energy or cyclotron orbit. By integrating Eq. (2.1) one gets

$$\underline{k} = \frac{e}{\hbar}\, \underline{r} \times \underline{B} \tag{2.2}$$

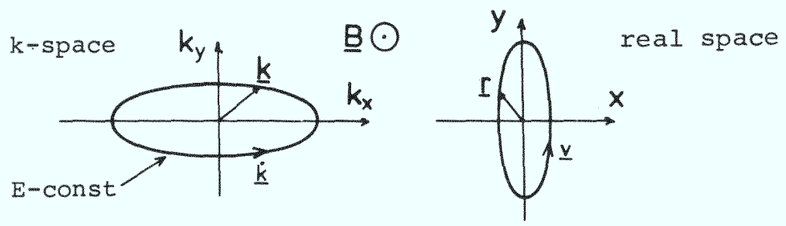

From this it can be seen that a cyclotron orbit in $\underline{k}$ space is related to the corresponding orbit in real space by a scaling factor $\frac{eB}{\hbar}$ and a rotation by $\pi/2$. The angular frequency ω_c for cyclotron motion is given by

cyclotron fequency: $$\omega_c = \frac{eB}{m_c} \tag{2.3}$$

where m_c is the cyclotron mass.

For electrons at the Fermi surface $\underline{v}(\underline{k})$ is the Fermi velocity and the relation between the cyclotron mass and the dispersion curve $E(\underline{k})$ can be seen from the following argument. The cylotron period T_c is given by

$$T_c = \frac{2\pi}{\omega_c} = \oint dt$$

using (2.1) and (2.3)

$$m_c = \frac{\hbar}{2\pi} \oint \frac{dk}{v_\perp(\underline{k})} \tag{2.4}$$

where $v_\perp(\underline{k}) \equiv |\underline{v} \times \hat{\underline{B}}| = \frac{1}{\hbar}\frac{\partial E(\underline{k})}{\partial k_n}$ is the length of the component of $\underline{v}(\underline{k})$ in the orbit plane, and dk_n is the perpendicular distance between two orbits with energy E and E+dE (figure 2.1).

From figure 2.1 it can be seen that this can be written as

$$m_c = \frac{\hbar^2}{2\pi}\oint \frac{\partial k_n \; dk}{\partial E}$$

Cyclotron mass: $$m_c = \frac{\hbar^2}{2\pi}\frac{\partial A}{\partial E} \qquad (2.5)$$

The cyclotron mass is therefore proportional to the energy derivative of the area A of the cyclotron orbit.

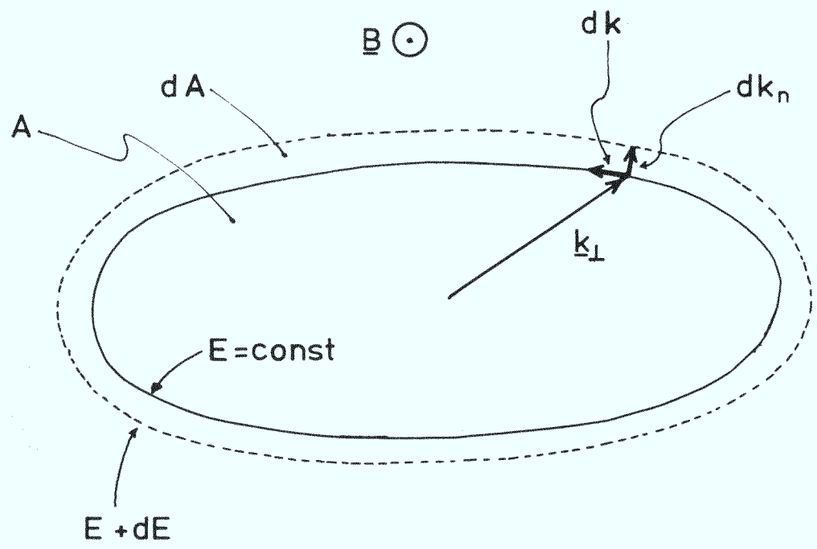

Fig. 2.1 The energy derivative of the area of a cyclotron orbit is proportional to the cyclotron mass (eq. 2.5).

Not all cyclotron orbits are allowed. Only those orbits through which the magnetic flux is a multiple of the fundamental flux quantum $\phi_o = \frac{2\pi\hbar}{e}$ are allowed.

$$\phi_n = \phi_o(n + \gamma)$$

n is an integer and $0 < \gamma < 1$ is a phase factor ($\gamma = 1/2$ for free electrons). This can also be expressed as a quantization of the area of the orbit in real space,

$$S_n = \frac{\phi_o}{B}(n + \gamma)$$

or as a quantization of the area of the orbit in $\underline{k}$-space (from eq. 2.2).

$$A_n = \frac{2\pi eB}{\hbar}(n + \gamma) = \frac{4\pi^2 B}{\phi_o}(n + \gamma) \qquad (2.6)$$

The allowed states lie on a set of cylinders in $\underline{k}$-space (Landau cylinders) which are separated in energy by $\hbar\omega_c$ (figure 2.2). The redistribution of the allowed states changes the density of states as shown in figure 2.3 for free electrons.

The allowed states in a magnetic field (Landau levels) can be labled by n, k_Z (for B in the Z direction) and s the spin quantum number. The degeneracy d of each state is equal to the magnetic flux through the sample in units of the fundamental flux quantum

$$d = \frac{\phi(\text{through sample})}{\phi_o} \qquad (2.7)$$

If the number of Landau cylinders intersecting the Fermi surface is large (Fermi energy $E_f >> \hbar\omega_c$), as is typically the case for metals in experimentally accessable fields, the Fermi surface is essentially unchanged in a magnetic field.

It is the redistribution of the allowed states in a magnetic field, together with the increase in the degeneracy which gives rise to the dHvA effect. This can be seen from the following ar-

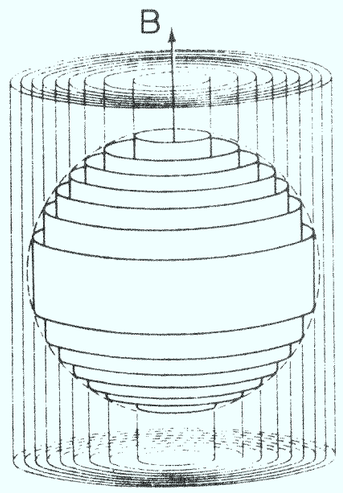

Fig. 2.2 The momentum states for free electrons in a magnetic field form a set of concentric Landau cylinders.

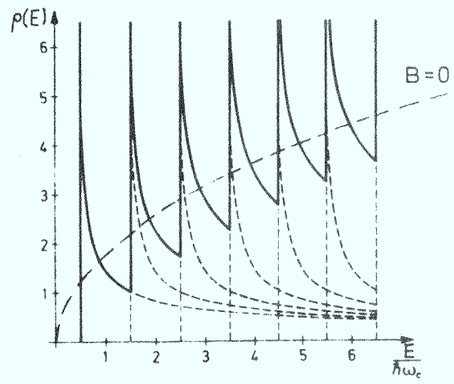

Fig. 2.3 The density of states for free electrons in an applied magnetic field. (Dashed lines show contributions from individual Landau cylinders, long dashes show the density of states in the absence of a field.)

gument. The cross sectional area of the Landau cylinders perpendicular to the field increases linearly with the field (eq. 2.6). Suppose at a certain field the n^{th} Landau cylinder is tangent to the Fermi surface. The states on this cylinder where it touches the Fermi surface will be occupied. As the field is increased this Landau cylinder will move beyond the Fermi surface and the electrons which occupied states on this cylinder must redistribute themselves on the lower lying cylinders. This gives rise to an abrupt change in the free energy and therefore in the magnetization. As the field increases further the $(n-1)^{th}$ and lower cylinders leave the Fermi surface one by one, causing an oscillatory variation in the magnetization. This is the dHvA effect. The oscillations repeat each time the tangential condition is fulfilled, that is, each time the cross sectional area of one of the cylinders is equal to the extremal cross sectional area A_{ext} of the Fermi surface perpendicular to the field.

tangential condition: $$A_{ext} = A_n = \frac{4\pi^2 B}{\phi_o} (n + \gamma)$$

$$n = \frac{\phi_o A_{ext}}{4\pi^2 B} - \gamma$$

The oscillations are therefore periodic in $\frac{1}{B}$ with a frequency proportional to the extremal cross sectional area.

dHvA frequency: $$F = \frac{\phi_o A_{ext}}{4\pi^2} \qquad (2.8)$$

The main contribution to the dHvA oscillations comes from the electrons near extremal cross sections. The contributions from non-extremal cross sections interfere destructively. The width of the band of electrons contributing to the dHvA effect depends on the change in the cross sectional area of the Fermi surface (perpendicular to the field) as the cross section moves away from the extremum. It also depends on the difference in area between neighboring Landau cylinders. The cross sectional area of the Fermi surface perpendicular to the field can be expanded as a Taylor series near the extremal cross section . For B in

the Z direction

$$|\Delta A| = |A(k_Z) - A_{ext}| \simeq \frac{1}{2}\left|\frac{\partial^2 A}{\partial k_Z^2}\right|_{ext} (\Delta k_Z)^2$$

From eq. 2.6 the area between adjacent Landau cylinders is

$$A_n - A_{n-1} = \frac{4\pi^2 B}{\phi_o}$$

The width of the band of contributing electrons Δk_Z is given approximately by

$$|\Delta A| = A_n - A_{n-1}$$

$$\frac{1}{2}\left|\frac{\partial^2 A}{\partial k_Z^2}\right|_{ext} (\Delta k_Z)^2 = \frac{4\pi^2 B}{\phi_o}$$

$$\Delta k_Z = \sqrt{\frac{8\pi^2 B}{\phi_o \left|\frac{\partial^2 A}{\partial k_Z^2}\right|_{ext}}} \qquad (2.9)$$

For a free electron sphere with Fermi wave vector k_s

$$\left|\frac{\partial^2 A}{\partial k_Z^2}\right|_{ext} = 2\pi \quad \text{and} \quad A_{ext} = \pi k_s^2$$

The angular width of the band of electrons (subtended from k = 0) is then

$$\frac{\Delta k_Z}{k_s} = \sqrt{\frac{B}{F}}$$

For metals the phase of the dHvA oscillations ($\sim\frac{F}{B}$) is usually large. For typical experimental conditions ($B \sim 5 \times 10^4$ G) $F/B \sim 10^4$ and the band of electrons contributing to the dHvA oscillations is very narrow ($\frac{\Delta k_z}{k_s} \sim 0.5^o$). This means that the information obtained from dHvA experiments is specific to elec-

trons on extremal orbits on the Fermi surface.

A finite temperature spreads out the cut-off between occupied and unoccupied states at the Fermi energy over a range of the order $k_B T$. The depletion of the states on the last Landau cylinder as it leaves the Fermi surface becomes gradual. This causes a reduction in the amplitude of the dHvA oscillations. The reduction depends on the ratio of $k_B T$ to the separation between cylinders $\hbar\omega_c$. In fact the damping factor depends exponentially on this ratio.

Thermal damping: $\sim \exp(-2\pi^2 \frac{k_B T}{\hbar\omega_c}) = \exp(-\alpha \frac{m_c}{m_o} \frac{T}{B})$

$$\alpha = \frac{2\pi^2 m_o k_B}{\hbar e}$$

From measurements of the temperature dependence of the dHvA amplitude the cyclotron mass can be obtained. Because of the temperature damping, the dHvA effect is usually difficult to observe for $T \gtrsim 4^{o}K$ in metals at fields normally used ($B \lesssim 10^5 G$).

If lattice defects are present the electrons will be scattered. The finite lifetime of the electrons broadens the Landau levels because of the uncertainty relation. The effect on the dHvA amplitude is similar to the smearing of the Fermi surface by a finite temperature. The Landau level width can be expressed in terms of a temperature called the Dingle temperature X. The Dingle temperature is proportional to an orbital average of the local scattering rates $\frac{1}{\tau(\underline{k})}$.

$$X = \frac{\hbar}{2\pi k_B} \left\langle \frac{1}{\tau(\underline{k})} \right\rangle \qquad (2.10)$$

The dHvA amplitude depends exponentially on the ratio of the level width $\sim k_B X$ to the level separation $\hbar\omega_c$.

Lifetime damping factor: $\exp(-2\pi \frac{k_B X}{\hbar\omega_c}) = \exp(-\alpha \frac{m_c}{m_o} \frac{X}{B})$

From the field dependence of the dHvA amplitude the product of the cyclotron mass and the Dingle temperature $m_c X$ can be determined. This is how the Dingle temperatures for Cu-H have been measured in the present work. Because of the lifetime damping the dHvA effect can only be observed in pure materials or dilute

alloys. By measuring X for different orbits the anisotropy of the scattering over the Fermi surface can be investigated.

Lifshitz-Kosevich expression

A general expression for the oscillatory magnetization for a Fermi surface of arbitrary shape can be derived by semiclassical arguments first put forward by Lifshitz and Kosevich (L-K) /2.1/. The oscillatory magnetization $\tilde{M}$ can be expressed as a sum of harmonic components:

$$\tilde{M} = \sum_{r=1}^{\infty} M_r(B,T,X)\sin\left[2\pi r\left(\frac{F}{B} - \gamma\right) \mp \frac{\pi}{4}\right] \qquad (2.11)$$

The amplitude of the r^{th} harmonic is

$$M_r = -\left(\frac{e^2\hbar A_{ext}}{4\pi^4 m_c r^{3/2}}\right)\left(\frac{2\pi eB}{\hbar\left|\frac{\partial^2 A}{\partial k_Z^2}\right|_{ext}}\right)^{1/2} \cos\left(\frac{r\pi g m_c}{2m_o}\right)\left(\frac{\kappa_r T \exp(-\kappa_r X)}{\sinh\kappa_r T}\right)$$

where $\kappa_r = \dfrac{r\alpha m_c}{Bm_o}$

$$\alpha = \frac{2\pi^2 k_B m_o}{\hbar e} = 1.469 \times 10^5 \text{ Gauss}/^oK$$

$$F = \frac{\hbar A_{ext}}{2\pi e}$$

The magnetic moment $g\mu_B s$ associated with the spin s of the electrons causes a splitting of the Landau cylinders into two sets of Landau cylinders, one for each spin direction, separated in energy by $g\mu_B B = \hbar\omega_c \frac{gm_c}{2m_o}$. Here $\mu_B = \frac{\hbar e}{2m_o}$ is the Bohr magneton and m_o the free electron mass. The spin splitting causes a reduction of the dHvA amplitude given by

$$\cos\left(\pi r \frac{gm_c}{2m_o}\right)$$

If experimental conditions are chosen so that the damping terms are large enough so that the higher harmonics $r > 1$ can be neglected equation (2.11) can be written as

$$\tilde{M} = M_1 \sin\left[2\pi\left(\frac{F}{B} - \gamma\right) \mp \frac{\pi}{4}\right] \qquad (2.12)$$

$$M_1 \approx \frac{T}{\sqrt{B}} \exp\left(-\frac{\alpha m_c (T+X)}{m_o B}\right) \text{ xconst}$$

Inspection of equation (2.11) shows that the following information can be obtained from dHvA measurements:

a) Measurement of the dHvA frequency F gives directly the extremal cross-section of the Fermi surface.
b) From (2.12)

$$\ln\left(\frac{M_1}{T}\right) = -\alpha\left(\frac{m_c}{m_o}\right)T/B + \text{const} \qquad (2.13)$$

By measuring the dHvA amplitude M_1 as a function of temperature at constant field and plotting $\ln\left(\frac{M_1}{T}\right)$ versus T one obtains a straight line with the slope $-\frac{\alpha}{B}\frac{m_c}{m_o}$. In this way accurate values for the cyclotron masses can be obtained (see fig. 2.4).

c) Similarly from (2.12)

$$\ln\left(M_1\sqrt{B}\right) = -\alpha\left(\frac{m_c}{m_o}\right)(T + X)/B + \text{const} \qquad (2.14)$$

by measuring M_1 as a function of field at constant temperature and plotting $\ln(M_1\sqrt{B})$ versus 1/B the product $m_c X$ can be obtained from the slope.

d) If $\frac{m_c}{m_o}$ and X are known then from (2.11) the relative amplitudes of the harmonics can give values for the spin splitting terms $\cos\left(\pi\frac{gm_c}{2m_o}\right)$ and hence g.

Some numerical values should illustrate the quantities specified in this section for a free electron metal with the electron density of copper ($8.5\cdot10^{22}$ el/cm^3). For a crystal 1 cm^3 in volume the spacing between neighboring points for B = 0 in k space is

$$\frac{2\pi}{1\text{cm}} \simeq 10^{-7}\ \text{Å}^{-1}$$

On the other hand the Fermi wave vector

$$k_s = 1.36\ \text{Å}^{-1}$$

so that the Fermi surface radius spans about 10^7 states.

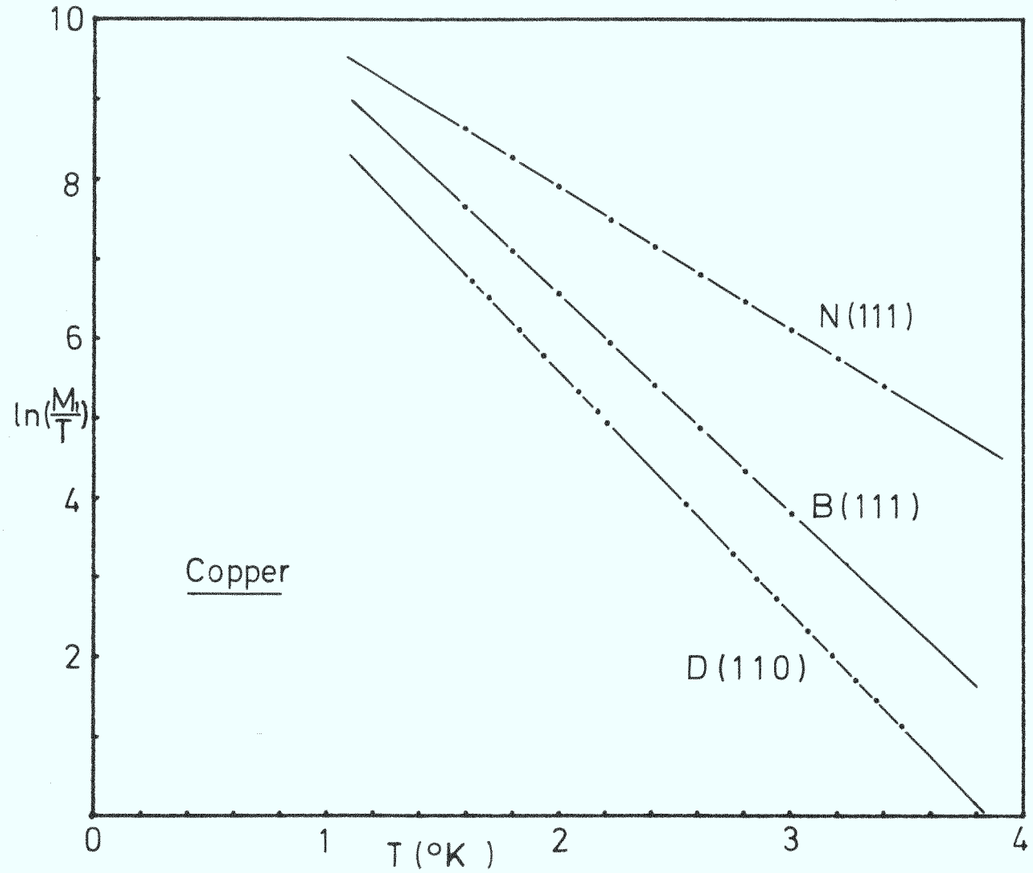

Fig. 2.4 Determination of the cyclotron masses in copper from the temperature dependence of the dHvA amplitude. Each point represents an amplitude measurement. The cyclotron mass is determined from the slope (slope = $-\frac{\alpha}{B}\frac{m_c}{m_o}$). The magnetic field for each mass measurement and the value for m_c/m_o from a least squares fit to the data is given below.

Orbit	B (kG)	m_c/m_o
N(111)	36.54	0.445 ± .001
B(111)	73.08	1.366 ± .002
D(110)	60.90	1.259 ± .002

The dHvA frequency is

$$F = 6 \cdot 10^8 \text{ Gauss}$$

so that typically $B = 5 \cdot 10^4$ Gauss

$$n \simeq F/B = 10^4$$

about 10^4 Landau cylinders intersect the Fermi surface. The degeneracy of the levels (eq. 2.7) is:

$$d = 10^{11}$$

It is this strong reduction of the number of possible states and the high degeneracy of them that makes the dHvA effect detectable. Only the states in a band of angular width (for B = 50 kG, belly orbit: figure 2.5)

$$\frac{\Delta k}{k_s} = \sqrt{\frac{1}{n}} = 0.5^o$$

at the extremal cross section contribute to the effect. The temperature damping of the dHvA oscillations is determined by $k_B T/\hbar\omega_c$. This is 0.086 meV/0.58 meV = 0.15 at 1 K and 50 kG. The effect is therefore hardly observable in a pure metal above 10 K.

2.2 dHvA frequencies and Fermi surface geometry

The high phase of the dHvA oscillations in metals under typical experimental conditions ($n \sim 10^4$) allows very accurate measurements of the Fermi surface cross sections to be made. By measuring the cross sections for different orientations of the crystal in the field, information on the anisotropy of the Fermi surface can be obtained. For certain orbits the frequency is an extremum with respect to orientation, for example at symmetry directions. For these orbits the crystal can be accurately oriented in the field so as to minimize errors due to misorientation. The dHvA frequencies and hence cross sectional areas for these orbits have been measured in the noble metals with a precision of better than $1:10^5$ /2.3/.

If a representation for the Fermi surface is available which allows the radius vectors $\underline{k}$ to be calculated from a set of parameters, then by integrating around an orbit the extremal areas can be calculated. The parameters can then be adjusted so that the calculated areas agree with the experimental areas.

One representation which has been particularly useful for the noble metals is to express the Fermi surface as a Fourier series which has been symmetrized to include the translational and the point group symmetry of the fcc lattice /2.4/.

$$F(\underline{k}) = \sum_{\ell,m,n} C_{\ell mn} \cos(\tfrac{a}{2}\ell k_x) \cos(\tfrac{a}{2} m k_y) \cos(\tfrac{a}{2} n k_z) \qquad (2.15)$$
$$= 0$$

with $\ell + m + n$ even integer and $\sum$ includes permutations of ℓ, m, n. This is the expression for the Fermi surface obtained from the tight binding approximation. Using this representation the Fermi surface can be described by a set of coefficients $C_{\ell mn}$ from which the wave vector $\underline{k} = (k_x, k_y, k_z)$ from $\underline{k} = 0$ to the Fermi surface can be calculated (a is the lattice parameter).

Using this representation the Fermi surfaces of the noble metals have been fitted to an accuracy of $1 : 10^{-3}$ using only five coefficients $C_{\ell mn}$ (see table 2.1) /2.3, 2.4/. Figure 2.5 shows a model of the Fermi surface of copper in the first Brillouin zone. It consists essentially of a distorted sphere (belly) with protrusions contacting the Brillouin zone in the 8 directions <±1, ±1, ±1> (necks). Figure 2.5 shows some typical extremal orbits: the belly and neck orbits B(111) and N(111) with the magnetic field along a direction <111>, the belly orbit B(100) with the field along a direction <100> and two hole orbits, the rosette orbit R(100) and the dogsbone orbit D(110) with the field along a direction <100> and <110> respectively.

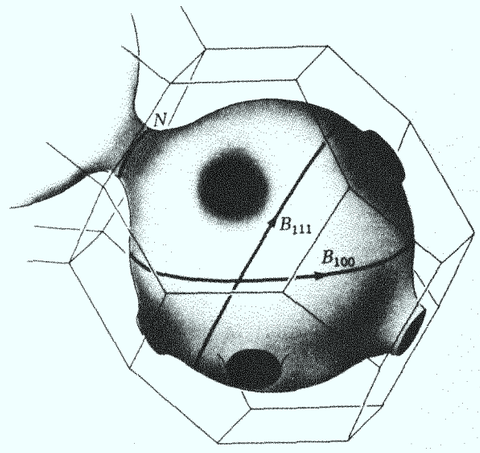

Fig. 2.5 a) The Fermi surface and Brillouin zone for copper with some extremal electron orbits

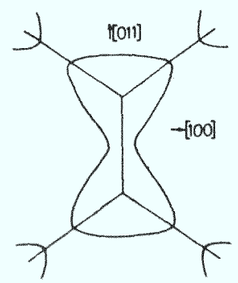

Dogsbone

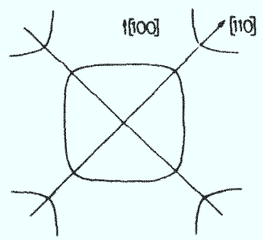

4-Rosette

b) The two main hole orbits for copper. The dogsbone for the magnetic field in the <110> direction, and the 4 cornered rosette for the field in the <100> direction. (Field direction is perpendicular to the page.)

Another parametrization scheme is a band structure calculation using a muffin-tin for the atomic potential. The radial wave functions outside the muffin-tin are expressed in terms of scattering phase shifts η_ℓ. From these phase shifts the radius vectors $\underline{k}$ of the Fermi surface can be calculated and hence the cross-sectional areas. The phase shifts are chosen to give a best fit between calculated and experimental areas. This representation has the advantage that the fitted parameters have a physical interpretation, but the disadvantage that calculation of radius vectors from the phase shifts is considerably more difficult than for the Fourier method. Phase shift fits for copper have been made by Lee /2.5/, "APW" Coenen & Vroomen /2.6/ "KKRZ" Shaw et al. /2.7/ "KKR". They were able to fit the measured areas to within $\sim 5 : 10^{-4}$ using three phase shifts. Agreement between values for the radius vectors $\underline{k}$ from the various fits (Fourier and phase shift) is of the order $1 : 10^3$.

Finally several authors have calculated the band structure for copper using APW and KKR methods and various potentials /2.8, 2.9, 2.10, 2.11/. The Fermi surface for Cu resulting from these calculations is somewhat dependent on the atomic potential assumed but is generally in good agreement with experiment.

2.3 Cyclotron masses and Fermi velocities

The Fourier series representation for the Fermi surface (2.13) can also be used to determine local values for the Fermi velocities from the cyclotron masses which can be obtained from dHvA measurements. Just as the Fermi surface can be represented by a set of coefficients $C_{\ell mn}$, a neighboring surface of constant energy $E_f + \Delta E$ can be represented by a second set of coefficients $D_{\ell mn}$.

The cyclotron mass is given by the energy derivative of the orbit area (eq. 2.5).

$$m_c = \frac{\hbar^2}{2\pi} \left(\frac{\partial A}{\partial E}\right)_{ext}$$

The derivative can be approximated by a small but finite ΔE.

$$m_c = \frac{\hbar^2}{2\pi} \left(\frac{\Delta A}{\Delta E}\right)_{ext}$$

For free electrons $m_c = \frac{\hbar^2}{2\pi} \frac{A_s}{E_s}$ where A_s and E_s are the area and Fermi energy for the free electron sphere.

When making calculations it is convenient to use the dimensionless form

$$\frac{m_c}{m_o} = \frac{\Delta A}{A_s} \frac{E_s}{\Delta E} \qquad (2.16)$$

Therefore if the coefficients for the two surfaces are known, the cyclotron mass can be found by calculating the difference in the area of the orbit on the two surfaces (see fig. 2.1).

The coefficients $D_{\ell mn}$ are chosen for the best fits between calculated and experimental masses. Table (2.1) gives the measured and fitted cyclotron masses for 14 extremal orbits in copper /2.12/. The coefficients for the two surfaces, which differ in energy by $\frac{\Delta E}{E_s} = 0.0006$, are also given in the table (2.1). The values $C_{\ell mn}$ are taken from Halse's paper /2.4/.

From these two surfaces the Fermi velocities $v(\underline{k}) = \frac{1}{\hbar} \nabla_{\underline{k}} E(\underline{k})$ can be calculated from

$$\frac{v(\underline{k})}{v_s} = \frac{1}{2} \frac{\Delta E}{E_s} \frac{k_s}{\Delta k_n} \qquad (2.17)$$

where k_s, v_s, E_s are the free electron values for the Fermi radius, velocity and energy, and Δk_n is the perpendicular distance between the two surfaces. Figure (2.6) shows lines of equal velocities in 1/48 of the Fermi surface in stereographic projection. Velocities are lowest at the neck and everywhere smaller than the free electron value. It will be seen that local values of the Fermi velocity are needed to obtain local lifetimes from dHvA measurements. The success of this inversion scheme for the velocities depends on the existence of a fairly accurate

Table 2.1

Cyclotron masses for Copper and Coefficients for 6 term Fourier fit for Fermi surface and Fermi velocities

Orbit $\underline{B}$ in (110) plane	m_c/m_o measured	fitted
B(100)	1.348 ± .002	1.348
BTP	1.308 ± .003	1.306
B51.74	1.367 ± .004	1.374
B(111)	1.366 ± .002	1.368
B65	1.431 ± .004	1.427
N(111)	0.445 ± .001	0.445
N65	0.478 ± .002	0.481
N75	0.648 ± .004	0.646
D(110)	1.259 ± .002	1.262
D85	1.288 ± .003	1.287
R	1.307 ± .002	1.304
B in (100) plane		
B30.5	1.533 ± .003	1.525
BTP	1.317 ± .003	1.321
D40	1.310 ± .003	1.308

Coefficients for 6 term Fourier fit $\frac{\Delta E}{E_s} = 0.0006$

lmn	C_{lmn}	D_{lmn}
000	0.22262	0.2246960
110	1	1
200	0.00693	0.0071999
211	-0.42501	-0.4240600
220	-0.01679	-0.0169474
310	-0.03772	-0.0378529

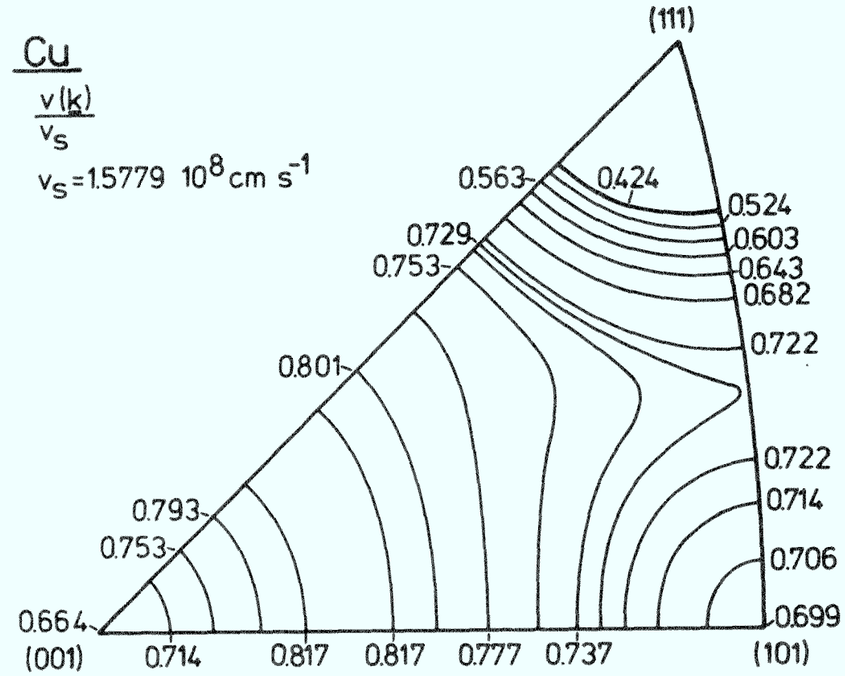

Fig. 2.6 The Fermi velocity for copper plotted as lines of constant velocity over a stereographic projection of the basic 1/48 th of the Fermi surface. v_s is the free electron velocity for Cu.

representation for the Fermi surface. For the noble metals cyclotron masses have been measured to an accuracy of $3 : 10^3$ /2.12/. The inversion scheme described above gives a fit to the data with an accuracy of $\sim 3 : 10^3$ using 5 coefficients.

Once the two neighboring surfaces of constant energy are known, the density of states $\rho(E_F)$ at the Fermi energy, which is essentially the energy derivative of the Fermi surface volume, can be found from the volume ΔV_k between the two surfaces.

$$\frac{\rho(E_F)}{\rho_s(E_F)} = \frac{2}{3} \frac{\Delta V_k}{V_s} \frac{E_s}{\Delta E} \qquad (2.18)$$

Here V_s and ρ_s are the Fermi surface volume and density of states for free electrons. Since the electronic specific heat is proportional to the density of states at the Fermi energy a value for $\frac{\rho(E_f)}{\rho_s}$ can also be obtained from specific heat measurements. For copper

$$\left(\frac{\rho(E_f)}{\rho_s(E_f)}\right)_{dHvA} = 1.380 \qquad /2.12/$$

$$\left(\frac{\rho(E_f)}{\rho_s(E_f)}\right)_{\text{specific heat}} = 1.383 \pm .002 \qquad /2.13/$$

The excellent agreement is evidence that the velocity inversion scheme is fairly good for the case of copper.

2.4 Influence of electron-phonon interaction on the dHvA effect

In section 2.2 it was discussed that the Fermi surface for copper from band structure calculations is in fairly good agreement with experiment. However, these calculations also provide values for the Fermi velocities, cyclotron masses, and electronic specific heat coefficient /2.14, 2.8/ and it is found that the calculated velocities are 10 to 20 % larger than the experimental values and the cyclotron masses and specific heat 10 to 20 % smaller. The explanation of the discrepancy is that the quantities which one measures in the dHvA effect or in the electronic specific heat are affected by the electron-phonon interaction whereas this effect is not included in the calculations. The electron-phonon interaction causes a shift in the energy of states within about $k_B\Theta_D$ of the Fermi energy as illustrated by figure 2.7 (Θ_D is the Debye temperature). Although the states just at the Fermi surface are not shifted in energy the slope of the dispersion curve at the Fermi level is decreased by the electron-phonon interaction /2.15/ (see figure 2.7).

$$E(\underline{k}) - E_F = \frac{E_o(\underline{k}) - E_F}{1 + \lambda(\underline{k})} \qquad |E_o(\underline{k}) - E_F| \ll k_B\Theta_D \qquad (2.19)$$

where $\lambda(\underline{k})$ is a renormalization factor which is $\underline{k}$-dependent

and positive. $E_o(\underline{k})$ is the dispersion relation without electron-phonon interaction. Therefore quantities which depend on the Fermi energy such as the Fermi surface are not affected whereas quantities depending on the derivative of the dispersion curve at the Fermi energy such as the Fermi velocity, cyclotron masses and the density of states are modified.

Since $v(\underline{k}) = \frac{1}{\hbar}\nabla_k E(\underline{k})$ it can be seen that the renormalized Fermi velocity is given by

$$v(\underline{k}) = \frac{v_o(\underline{k})}{1 + \lambda(\underline{k})} \qquad (2.20)$$

where $v_o(\underline{k})$ is the non-renormalized or 'band' velocity. Since the cyclotron mass is the energy derivative of the orbit area at the Fermi surface it will also be affected. From (2.4)

$$m_c = \frac{\hbar}{2\pi}\oint \frac{dk}{v_\perp}$$

$$= \frac{\hbar^2}{2\pi}\oint (1 + \lambda(\underline{k}))\ \frac{dk}{v_{o\perp}} \qquad (2.21)$$

$$= m_c^o\ (1 + \Lambda)$$

where the factor $(1 + \Lambda) \equiv \frac{m_c}{m_c^o} = \frac{\oint (1 + \lambda(\underline{k}))\frac{dk}{v_{o\perp}}}{\oint \frac{dk}{v_{o\perp}}}$

is an orbital mass enhancement factor which is an orbital average of the local renormalization factor $(1 + \lambda(\underline{k}))$.

The spacing between Landau cylinders

$$\hbar\omega_c = \frac{\hbar eB}{m_c} = \frac{\hbar eB}{m_c^o(1 + \Lambda)}$$

is reduced by the electron phonon interaction. This is illustrated in figure 2.8. As can be seen from the L-K expression (2.11) the dHvA amplitude depends on the cyclotron mass through the ratio $k_BT/\hbar\omega_c$. Since $\hbar\omega_c$ is reduced by the electron-phonon interaction but not k_BT it is clear that the cyclotron mass measured in dHvA experiments will be the enhanced value. Cyclotron

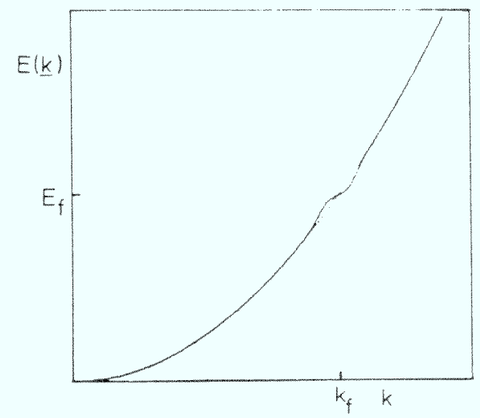

Fig. 2.7 Effect of electron-phonon interaction on dispersion curve for free electrons.

Fig. 2.8 The electron-phonon interaction reduces the Landau level separation at the Fermi energy by a factor 1 + λ.

resonance and electronic specific heat measurements are similarly affected. Figure (2.9) is a contour plot showing the anisotropy of the renormalization factor $1 + \lambda(\underline{k})$ over the Fermi surface obtained by comparison of Fermi velocities from a band structure calculation to those determined experimentally from dHvA measurements /2.14/, $(1 + \lambda(\underline{k}))$ varies in the case of copper from 1.04 to 1.21. One point to note regarding the L-K expression is that the spin splitting factor $\cos(\pi g m_c/2m_o)$ depends on the ratio of the spin energy $\pm\frac{1}{2}g\mu_B B$ to the cyclotron energy $\hbar\omega_c$. Since both energies are renormalized by the same factor $1/(1 + \lambda(\underline{k}))$ the ratio, on which the dHvA amplitude depends, is not affected by the electron-phonon interaction.

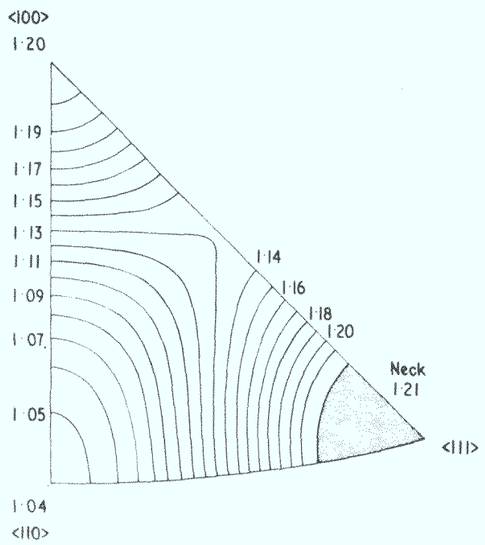

Fig. 2.9 Anisotropy of the electron-phonon enhancement parameter $1 + \lambda(\underline{k})$ over the Fermi surface of copper /5.7/ shown as a contour plot over the basic 1/48 th of the Fermi surface in stereographic projection.

2.5 Dingle temperatures and local lifetimes

In section 2.1 it was shown from the L-K expression (2.11) how dHvA measurements can provide information about the scattering of conduction electrons from impurities in the form of a Dingle temperature. In this section the meaning of this parameter is discussed and it is shown how more specific information about the scattering in the form of local lifetimes can be obtained from it.

2.5.1 Transition probabilities and lifetimes

We consider a metal containing randomly distributed impurities of low concentration (atomic fraction of impurities $c_i \ll 1$). The scattering rate per unit time for scattering of an electron from a state $\underline{k}$ into a state $\underline{k}'$ is given by /2.16/.

$$P_{\underline{k}\underline{k}'} = \frac{2\pi c_i}{\hbar} |T_{\underline{k}\underline{k}'}|^2 \delta(E(\underline{k})-E(\underline{k}')) \qquad (2.22)$$

where $T_{\underline{k}\underline{k}'}$ are matrix elements of the T-matrix given by

$$T_{\underline{k}\underline{k}'} \equiv \int d^3r \Phi^*_{\underline{k}'}(\underline{r}) V(\underline{r}) \Psi^+_{\underline{k}}(\underline{r}) \qquad (2.23)$$

$\Phi_{\underline{k}'}(\underline{r})$ is the unperturbed final state, $\Psi^+_{\underline{k}}(\underline{r})$ is the perturbed initial state and $V(\underline{r})$ the scattering potential. The local electron lifetime $\tau(\underline{k})$ is derived from $P_{\underline{k}\underline{k}'}$ by summing over all possible final states

$$\frac{1}{\tau(\underline{k})} = \sum_{\underline{k}'} P_{\underline{k}\underline{k}'} \qquad (2.24)$$

Since the number of electrons scattered out of the initial state $\underline{k}$ must be equal to the number scattered into all final states $\underline{k}'$ the T matrix satisfies the optical theorem

$$I_m(T_{\underline{k}\underline{k}}) = -\pi \sum_{\underline{k}'} |T_{kk'}|^2 \delta(E(\underline{k})-E(\underline{k}')) \tag{2.25}$$

Therefore the lifetime can be expressed in terms of the T-matrix

$$\frac{1}{\tau(\underline{k})} = -\frac{2c_i}{\hbar} I_m (T_{\underline{k}\underline{k}}) \tag{2.26}$$

The scattering can also be described as a complex energy shift of the Bloch states or self energy /2.17, 2.18, 2.19, 2.20/.

$$\Sigma(\underline{k}) = \Delta(\underline{k}) + i\Gamma(\underline{k}) \tag{2.27}$$

$\Gamma(\underline{k})$ is the half width of the uncertainty in the energy due to the finite lifetime

$$\Gamma(\underline{k}) = \frac{\hbar}{2\tau(k)} \tag{2.28}$$

and $\Delta(\underline{k})$ is a change in the energy of the state $\underline{k}$ due to the scattering. In terms of the T matrix

$$\Sigma(\underline{k}) = c_i T_{kk} \tag{2.29}$$

The density of states can be expressed in terms of the self energy as /2.20/

$$\rho(E) = -\frac{1}{\pi} \sum_{\underline{k}} I_m (E-E_o(\underline{k})- \Sigma(\underline{k}))^{-1} \tag{2.30}$$

where $E_o(\underline{k})$ are the energy eigenvalues for the pure lattice. In the original derivation of the L-K expression (2.11) the effect of scattering was taken into account by the phenomenological assumption that the Landau levels were broadened into a Lorentzian distribution. By using equation (2.30) for the density of states, the L-K expression can be obtained without this assumption. In this treatment the T-matrix in the presence of the magnetic field is approximated by the T-matrix in the absence of a field.

The result to emerge from this treatment is that the Dingle temperature depends on an orbital average of the imaginary part of the self energy which is equivalent to the Lorentzian half width used in the original derivation of equation 2.11. The Dingle temperature can be expressed as

$$X = -\frac{\hbar}{2\pi k_B} \langle \Gamma(\underline{k}) \rangle$$

or in terms of the lifetime

$$X = \frac{\hbar}{2\pi k_B} \left\langle \frac{1}{\tau(\underline{k})} \right\rangle \qquad (2.31)$$

where $\tau(\underline{k})$ here is the same $\tau(\underline{k})$ defined by (2.24). Another result is that the real part of the self energy gives rise to a scattering induced change in the dHvA frequency, an effect which was omitted from the original derivation /2.17, 2.21, 2.22/

$$F = F_o + \Delta F$$

$$\Delta F = -\frac{m_c}{\hbar e} \langle \Delta(\underline{k}) \rangle \qquad (2.32)$$

This frequency change is small in dilute alloys. It was not measured in the dHvA experiment described in the next chapter.

The great advantage of using the dHvA effect to investigate scattering lies in the fact that

a) Only the conduction electrons in a narrow band around the extremal orbit contribute to the average (2.31) so that local lifetimes can be determined.

b) A comparison between measured dHvA lifetimes and theory is relatively easy because of the uncomplicated relation (2.24) between dHvA lifetimes and transition probabilities. In contrast a comparison based on transport properties requires a solution to the Boltzmann equation and is therefore much more difficult.

2.5.2 Effect of electron-phonon interaction on lifetimes

Since the effect of scattering can be described in terms of a shift in the energy of a Bloch state, this shift will be reduced by the electron-phonon interaction according to (2.19) by a factor $1/(1 + \lambda(\underline{k}))$. This means that the reciprocal lifetime is reduced by a factor $1/(1 + \lambda(\underline{k}))$ and since the Fermi velocity is also reduced by the same factor the product $v(k)\tau(k)$ is unaffected. Further the Dingle temperature being an orbital average of the reciprocal lifetime is reduced by the same factor by which the cyclotron mass is enhanced (see eq. (2.21)), thus the product $m_c X$ is also unaffected by the electron-phonon interaction at low temperatures. This cancellation can also be understood by considering figure 2.6. The width $\sim k_B X$ of a Landau level is reduced by the same factor as the level separation $\hbar\omega_c$ and the ratio which enters into the dHvA effect is not affected.

It might be expected that the additional scattering of the electrons from phonons would give rise to a temperature dependent contribution to the scattering rates $\frac{1}{\tau}$ which are measured in dHvA experiments. Such a contribution has been observed in experiments on cyclotron resonance and magnetic surface states in copper /2.23, 2.24/. It has been shown however /2.25, 2.26/ that to a good approximation this temperature dependence does not appear in the lifetimes measured by dHvA effect. The dHvA lifetimes are therefore specifically due to impurity scattering and temperature scattering can be neglected.

2.5.3 Decomposition of Dingle temperatures into local scattering rates

It will now be shown how the local scattering rates $1/\tau(\underline{k})$ can be obtained from the Dingle temperatures which are an orbital average of the lifetime

$$X = \frac{\hbar}{2\pi k_B} \left\langle \frac{1}{\tau(\underline{k})} \right\rangle \qquad (2.31)$$

The orbital average can be written as an integral of $1/\tau(\underline{k})$ around the orbit weighted by the time spent by the $\underline{k}$ vector at each position on the orbit

$$\left\langle \frac{1}{\tau(\underline{k})} \right\rangle = \frac{1}{T_c} \oint \frac{1}{\tau(\underline{k})}\, dt \qquad (2.32)$$

Using eq. (2.1) and figure (2.10) the expression (2.31) can be transformed into an integral over the angle φ characterizing the position of k on the orbit. The product of m_c and X is then given by

$$m_c X = \frac{\hbar^2}{4\pi^2 k_B} \oint d\varphi \, \frac{k_\perp^2}{(\underline{v}\cdot\underline{k}_\perp)} \, \frac{1}{\tau(\underline{k})} \qquad (2.33)$$

where $\underline{k}$ is the component of $\underline{k}$ in the cyclotron plane. The integrand is split into a term $1/\tau(\underline{k})$ characterizing the impurity and a weight factor $k_\perp^2/(\underline{v}\cdot\underline{k}_\perp)$. This factor depends only on the Fermi surface geometry and the Fermi velocities of the host.

In choosing a representation for $\frac{1}{\tau(\underline{k})}$ it is important to take advantage of the symmetry of the problem since this will reduce the number of coefficients needed in the fit. The symmetrized Fourier series is a good choice since it includes the point and the translational symmetry of the lattice. Thus $\frac{1}{\tau(\underline{k})}$ can be represented by a symmetrized Fourier expansion as used for the Fermi surface description (2.13).

$$\frac{1}{\tau(\underline{k})} = \sum_j T_j \Phi_j(\underline{k}) \qquad (2.34)$$

with $\Phi_j(\underline{k}) = \cos(\frac{a}{2}\ell k_x)\cos(\frac{a}{2}m k_y)\cos(\frac{a}{2}n k_z)$
a is the lattice parameter (a = 3.603 Å for Cu)
and j = (ℓ, m, n) where ℓ + m + n is even for an fcc lattice.
The Fourier components are ordered according to increasing $\ell^2 + m^2 + n^2$. This representation together with eq. (2.33) gives an expression for the Dingle temperature in terms of the coefficients T_j and a set of orbital weight factors H_{ij}

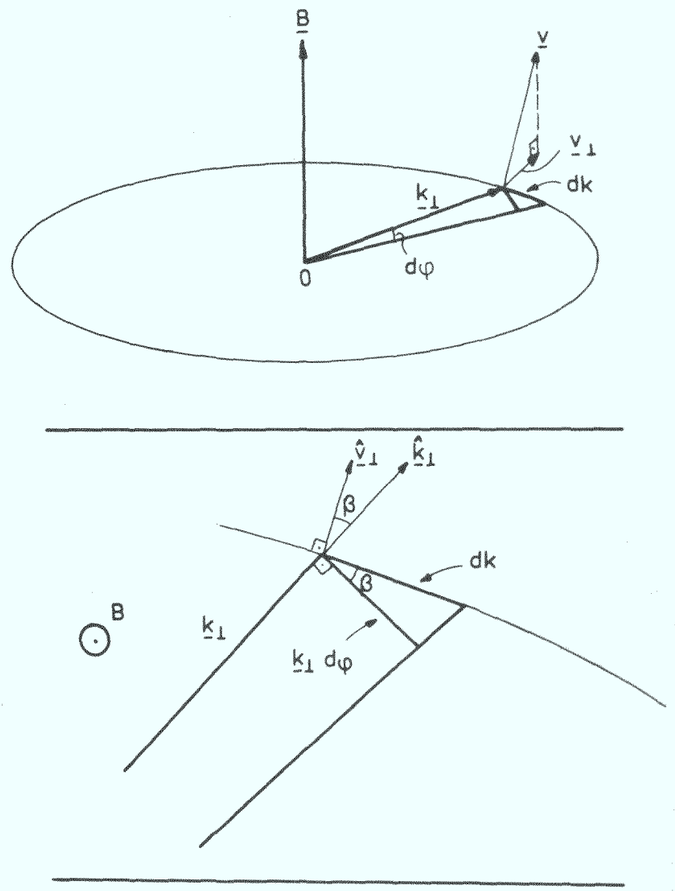

$$\underline{F} = \hbar\dot{\underline{k}} = e\underline{v} \times \underline{B}$$

$$\frac{dt}{T_c} = \frac{\hbar}{2\pi m_c}\frac{dk}{v_\perp}$$

$$= \frac{\hbar}{2\pi m_c}\frac{k_\perp^2\, d\varphi}{(\underline{v}\cdot\underline{k}_\perp)}$$

$$\dot{dk} = \frac{k_\perp\, d\varphi}{\cos\beta}$$

$$= \frac{k_\perp\, d\varphi}{\hat{\underline{v}}_\perp\cdot\hat{\underline{k}}_\perp}$$

$$\hat{\underline{v}}_\perp\cdot\underline{k}_\perp = \hat{\underline{v}}\cdot\underline{k}_\perp$$

Fig. 2.10

$$X_i = \sum_j H_{ij} T_j \qquad \begin{matrix} i \text{ th orbit} \\ j \text{ th Fourier term} \end{matrix}$$

where

$$H_{ij} = \left(\frac{\hbar^2}{4\pi^2 k_B m c_i} \right) \oint_i \frac{k_\perp^2}{(\underline{v} \cdot \underline{k}_\perp)} \Phi_j(\underline{k}) \, d\varphi \qquad (2.35)$$

The orbital weight factors H_{ij} depend on the Fermi surface and the Fermi velocities. In this work the Fermi wave vectors $\underline{k}$ and Fermi velocities $v(\underline{k})$ for copper were calculated from the symmetrized Fourier series representations as described in sections 2.2 and 2.3 using the coefficients $C_{\ell mn}$ and $D_{\ell mn}$ listed in table 2.1.

The coefficients T_j are found by minimizing

$$Q = \sum_i \left(\frac{X_i^f - X_i^m}{\sigma_{Xi}} \right)^2 \qquad (2.36)$$

where X_i^m, σ_{Xi} are the measured Dingle temperatures and the corresponding standard error and X_i^f are the X-values calculated from 2.33. Details on how the fit to the measured data was made are given in the appendix.

The propagation of the experimental errors in X into errors in the local scattering rates is discussed as well as the effect of increasing the number of coefficients on the significance of the fit.

§3 Details of the experiment

3.1 Description of the experiment, dHvA measurements in CuH

The experiment with which this dissertation is mainly concerned consisted of measurements of the dHvA Dingle temperatures for several orbits in a series of copper samples containing dissolved hydrogen. The way in which these measurements were made is described in this section. Also described is the experimental apparatus and the way in which the samples were prepared.

3.1.1 Experimental set-up

3.1.1.1 Field modulation technique

As discussed in the previous section Dingle temperatures and effective masses are determined from measurements of the amplitude of the oscillatory component of the magnetization. To measure this amplitude we have used the field modulation technique which is the method most used for dHvA measurements on metals /3.1, 3.2, 3.3/. A low frequency low amplitude alternating magnetic field is superposed on the larger quasistatic field B_o. (For the moment we neglect the effect of M on B so that $B = \mu_o H$. The effect of a finite M is discussed in section 3.1.4.)

$$B = B_o + b\cos\omega t \qquad b << B_o$$

The alternating magnetic field causes a periodic change in the magnetization of the sample at the modulation frequency which induces a voltage in a pick-up coil surrounding the sample. Considering only the fundamental dHvA component, the oscillatory magnetization can be expressed as:

$$\hat{M} = M_1(B,T,X)\sin\left[2\pi\left(\frac{F}{B} + \gamma\right) \mp \frac{\pi}{4}\right]$$

where M_1 changes slowly with field. In the presence of a modulation field

$$\hat{M}(t) = M_1(B_o,T,X)\sin\left[2\pi\frac{F}{B_o}(1-\frac{b}{B_o}\cos\omega t)+\gamma\mp\frac{\pi}{4}\right] \qquad (3.1)$$

Because of the non-linear magnetization the voltage induced in the pick-up coil is a superposition of harmonics of the modulation frequency:

$$\hat{V}(t) = \sum_{n=1}^{\infty} V_n \sin(n\omega t + n\frac{\pi}{2}) \qquad (3.2)$$

where the amplitude of the n^{th} harmonic is

$$V_n = V_o\, n\omega J_n(2\pi Fb/B_o^2)M_1(B_o,T,X)\sin\left[2\pi(\frac{F}{B_o}+\gamma+\frac{n}{4})\right] \qquad (3.3)$$

J_n is the Bessel function of order n. The amplitude of one of the harmonics, usually the second, is measured by a lock-in technique. This gives an output voltage proportional to the oscillatory component of the magnetization. This output signal from the lock-in is recorded on an X-Y recorder as the larger field is slowly swept. M_1 is then just proportional to the amplitude of the recorded oscillations. If measurements of M_1 at different fields are being compared the modulation current is usually chosen so that the Bessel function is at the first maximum J_n (3.054) so that small deviations from the correct modulation current setting will not cause errors in the measurement of M_1. Experimentally the modulation coil was calibrated in gauss/ma by measuring the amplitude of V_2 as a function of modulation current for a dHvA signal of known frequency. The calibration can then be accurately found from the Bessel function zero crossing points.

3.1.1.2 Pick-up and modulation coils

A split pick-up, modulation coil arrangement was used so that the sample could be rotated during measurement (see figure 3.1). The dimensions of the coil assembly were specified by the size of the sample (1 mm dia x 5 mm) and the requirement of optimum coupling between the sample and the pick-up coil. The modu-

lation coil consisted of 800 turns of 140 μm Cu wire giving ∿ 2 gauss/ma at the sample. The pick-up coil consisted of 3200 turns of 60 μm Cu wire. A balancing coil was wound concentrically with the pick-up coil and consisted of 1200 turns of 60 μm wire. This coil was connected in oppostion to the pick-up coil and the number of turns adjusted to compensate the voltage induced in the pick-up coil when it contained no sample. This compensation is important since a) it greatly reduces the amplitude at the fundamental frequency induced in the pick-up coil which would otherwise saturate the amplifiers, b) the signal at the detection frequency (e.g. 2ω) from harmonic distortion in the modulation current is greatly reduced. c) The noise due to the vibration of the pick-up coil is reduced since the compensation coil is rigidly coupled to it and they move together. The resistance of the pick-up and modulation coils at 4.2 K were 10 Ω and 1 Ω, respectively. The coil former and other parts of the sample holder were machined from a polyimide plastic called "Vespel" from Dupont which has a low coefficient of thermal expansion.

3.1.1.3 Electronic set-up

The layout of the electronics for the experiment is shown schematically in figure 3.2. The electronics consists essentially of three sections. a) The signal processing section from the pick-up coil to the plotter. b) The modulation circuit, c) the magnet control section.

In the signal processing section the voltage induced in the pick-up coil is first transformed by a PAR 190 low noise transformer by a factor of 1:100 and then amplified by a high impedance preamplifier (PAR 113). The signal then goes through a notch filter (PAR 210) adjusted to remove the component at the fundamental frequency. The signal is then detected by a lock-in amplifier (PAR 124) at the 2^{nd} harmonic of the modulation frequency and finally plotted on the vertical axis of the X-Y plotter.

Fig. 3.1 The sample holder for dHvA experiments

S sample
RA rotation axis
WR worm gear for rotation
TA tilt axis
WT worm gear for tilt adjustment
M modulation coil
P pick-up coil with compensation.

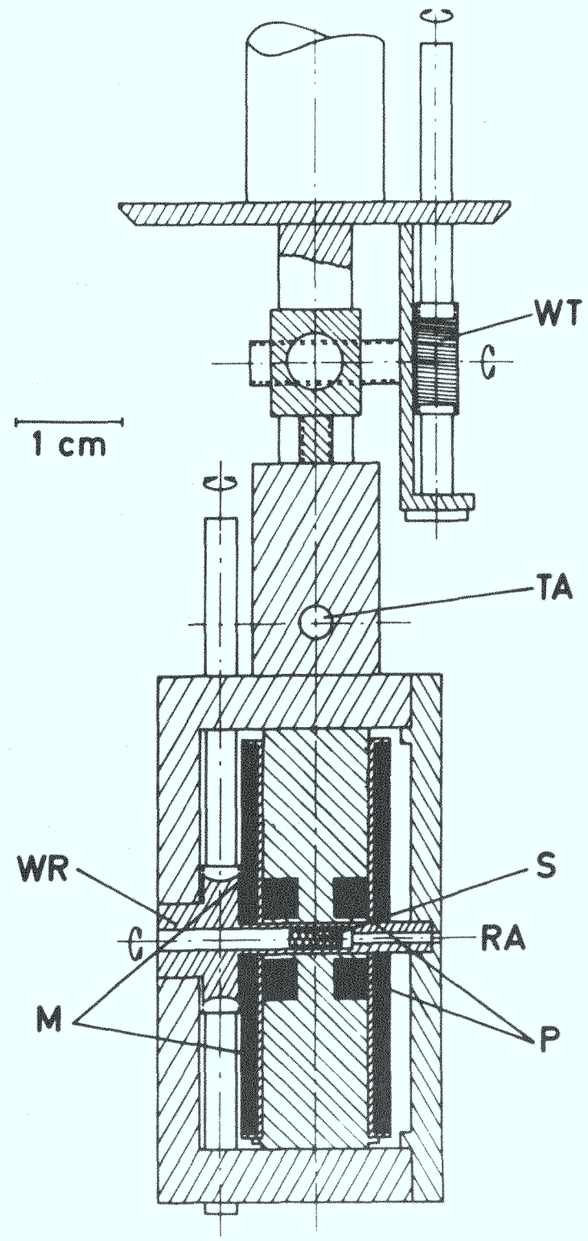

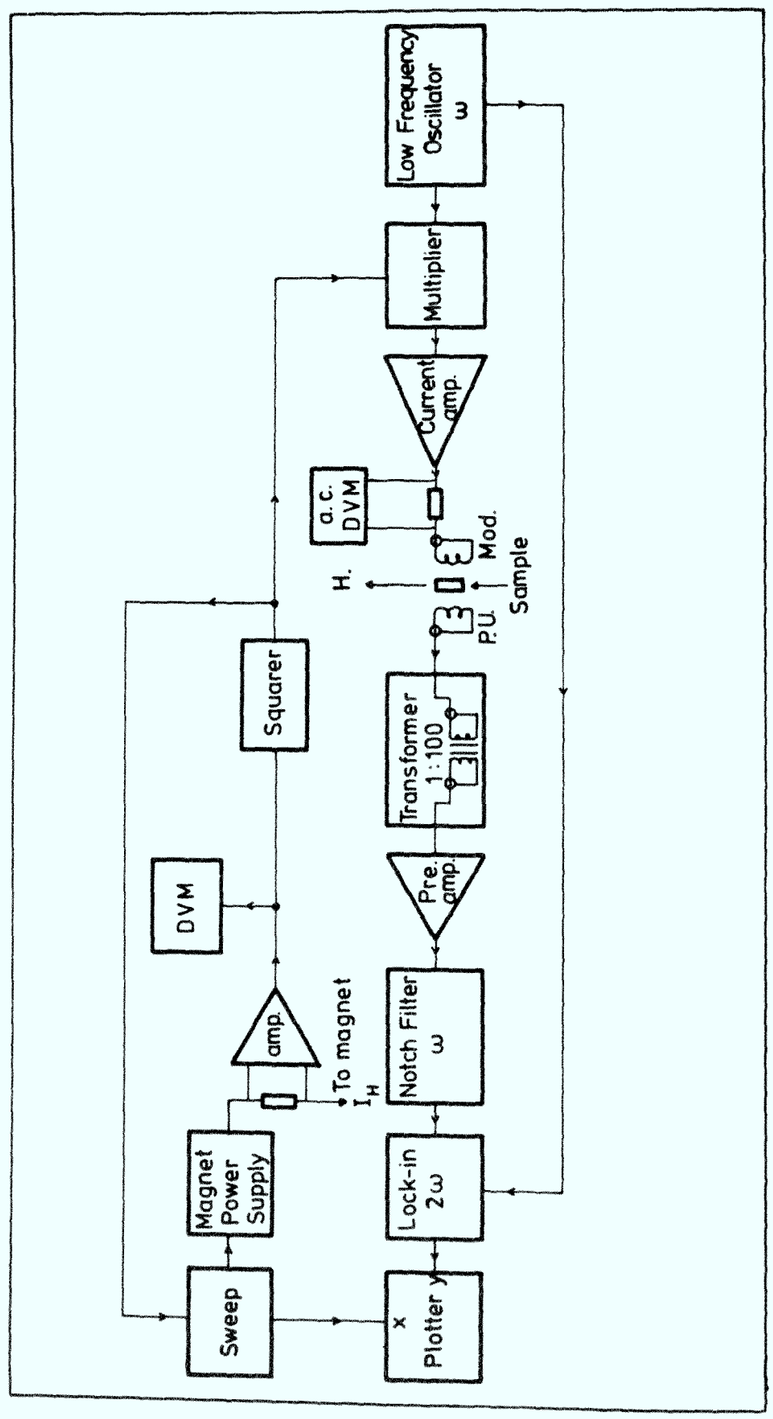

Fig. 3.2 Electronics for the dHvA experiment

In the modulation section a low distortion low frequency ac voltage is generated by an oscillator. This ac voltage was then multiplied by a voltage proportional to B^2 (Analog Devices 424 K, High accuracy multiplier). This signal was then amplified by a low distortion audio amplifier with low output impedance. Typically, modulation currents in the region of a few milliamps to a few hundred milliamps were used. The amplifier output supplied the current to the modulation coil in series with a 10 Ω resistor. The voltage drop across this resistor was used to measure the modulation current. This resistor also protected the modulation coil by limiting the maximum current. It also reduced the changes in modulation current due to the field dependence of the resistance of the modulation coil. The 2^{nd} harmonic distortion of the modulation current must be as small as possible ($\lesssim 2 \cdot 10^{-4}$) since it appears as an offset at the output of the lock-in.

The magnet control section consisted mainly of a high stability low drift current supply for the magnet (Drush, stability $1:10^5$) and a field sweep control unit.
When recording a dHvA signal, the current from the Drush is chosen to give the field B_o at which the measurement is to be made. The current is then slowly swept over a range $\Delta B << B_o$ which gives several dHvA oscillations. The field sweep is controlled by a voltage provided by the sweep unit.

Typical sweep rates give a few oscillation per minute. Since the dHvA oscillations are periodic in $1/B$, in order to have the recorded oscillations periodic in time the field must be swept such that $1/B$ changes linearly with time. This is satisfied if $d\beta/dt \propto B^2$.
But the field consists of a large constant part B_o and a small time dependent part (sweep)

$$B = B_o + B_s(t) \qquad (3.4)$$

The condition for dHvA oscillation periodic in time is then

$$\frac{dB}{dt} = \frac{dB_s}{dt} \propto B^2 \qquad (3.5)$$

That is, the control voltage from the sweep unit must be of the form

$$V_s \propto \int B^2 dt + \text{const} \qquad (3.6)$$

The sweep unit is then essentially a precision integrator with sweep rate and range selection. The magnet current is measured by the voltage drop across a 10^{-4} Ω standard resistor. This voltage, of the order of millivolts, is amplified and displayed on a digital voltmeter. This voltage is also squared (Analog devices 424 K) and fed back to the sweep control unit and to the modulation multiplier.

3.1.1.4 Magnet and cryostat

The magnet was a NbTi superconducting solenoid from BOC, with a maximum field of 76 Kilogauss. The bore of the magnet was 5.0 cm and the homogeneity was specified as $1:10^5$/cm at the center. The magnetic field was measured by measuring the current. The field was calibrated in terms of the current by using the NMR resonance of ^{27}Al nuclei observed with the aid of a marginal oscillator. The linearity of the field vs current curve was found to be $\sim 1:10^4$ and no hysteresis could be observed (hysteresis $\lesssim$ 1 gauss) (B/I = 1.2180 Kg/Amp). The transverse and axial field homogeneity were also measured. The axial field gradient at the center of the magnet was of the order of $1:10^5$ per centimeter. The transverse gradient was found to be $\sim 4:10^5$/cm at the magnet center and was approximately constant over the cross-section. The sample holder was therefore oriented such that the axis of the sample was normal to the transverse field gradient. The total field inhomogeneity over the sample was estimated then to be $5:10^6$ mostly due to the transverse gradient.

The cryostat consisted of an inner helium dewar in which the sample was located, an outer helium dewar for the superconducting magnet, and outside of this a liquid nitrogen jacket. The magnet was operated at 4.2 ^{o}K (atmospheric pressure). By pumping on the inner dewar, the temperature of the inner helium bath could be varied between 4.2 ^{o}K and 1.2 ^{o}K. A backing pump from Alcatel with a pumping speed of 200 m^3/h was used for this purpose.

The primary source of noise in the signal processing circuit was mechanical vibration. For this reason it is important that the sample holder, the inner dewar, and the magnet be rigidly connected to one another. Also the noise level was considerably reduced by mounting the whole cryostat on rubber pads.

3.1.1.5 Field calibration by NMR technique

The circuit diagram for the marginal RF oscillator used for the NMR measurements is shown in Figure 3.3. This is similar to the circuit described by Hill and Huang /3.4/. The circuit is essentially a high frequency oscillator in which the gain can be adjusted until oscillation is just maintained. The small change in the Q of the tank circuit, which occurs when the NMR resonance condition $f = \gamma_{Al} B$ is fulfilled where B is the magnetic field, f is the oscillator frequency and γ_{Al} is the gyromagnetic ratio of the resonant nuclei (see footnote), then causes a relatively larger change in the RF voltage level. The tank circuit consists of a coil containing the NMR sample located in the cryostat, a length of coaxial cable connecting the coil to the oscillator, and at the oscillator end of the coax, a varactor diode. The circuit oscillates at the resonant frequency of the tank circuit. If a transmission line is terminated by a pure reactance X then the impedance as seen at the other end of the line is also a pure reactance X' but transformed by the line according to

$$X' = \frac{Z_o}{\tan\left(\frac{\omega \ell}{v} + \frac{\delta}{2}\right)} \qquad (3.7)$$

Warning: Several of the symbols used in this section (3.1.1.5) have a different definition in the rest of the text.

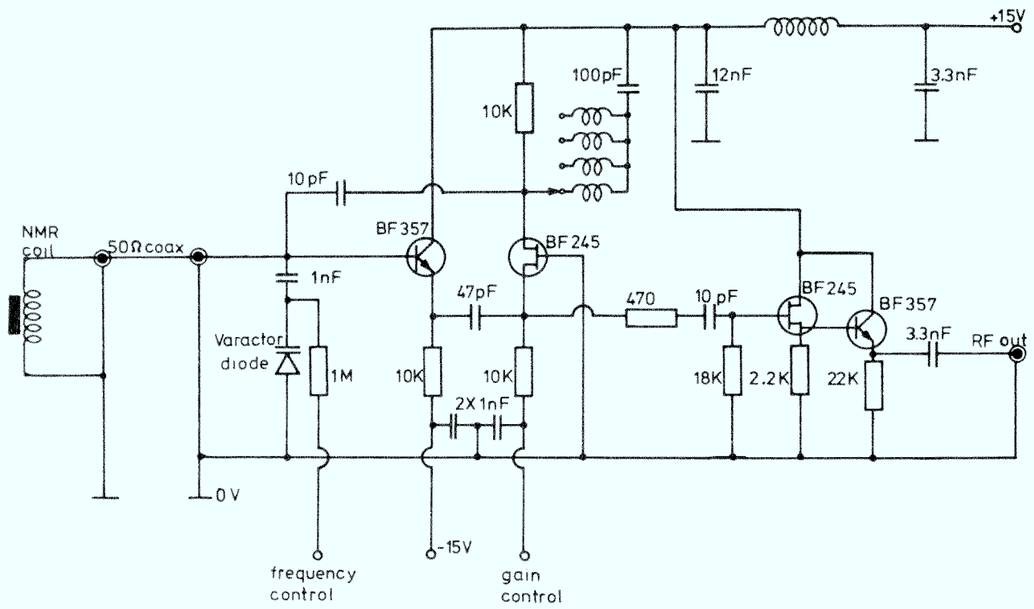

Fig. 3.3 Marginal NMR oscillator used to test field homogeneity of magnet and make the field versus magnet current calibration.

where $\tan\frac{\delta}{2} = \frac{Z_o}{X}$, Z_o is the characteristic impedance of the transmission line, ℓ is the length of the line and v is the propagation velocity of the line. For the present case of termination by a coil $X = \omega L$ the tank circuit is formed by the transformed impedance in parallel with the varactor diode impedance $Z_c = 1/i\omega C$. For resonance

$$\frac{1}{Z_{tank}} = \left(\frac{1}{iX'} + i\omega C\right) = 0$$

i.e. $$X' = \frac{1}{\omega C}$$

(3.8)

or $$\tan\left(\frac{\omega\ell}{v} + \frac{\delta}{2}\right) = Z_o\omega C$$

where $$\tan\frac{\delta}{2} = \frac{Z_o}{\omega L}$$

When $\omega L/v = n\pi$, ie $\ell = n\lambda/2$ the condition for resonance becomes

$$\frac{Z_o}{\omega L} = Z_o \omega C$$

$$\omega = \frac{1}{\sqrt{LC}}$$

Equation (3.8) is an implicit equation for the frequency as a function of L, C, and ℓ. This is a multivalued function since for given values for L, C, ℓ a family of resonant frequencies, or modes are possible. In practice the oscillator tends to operate in the lower modes, that is at the lower frequencies. Increasing the length of the cable lowers the frequency. If the oscillator gain is made frequency selective, the lower modes can be suppressed so that higher frequencies can be obtained. The desired operating frequency is selected by choosing the required mode to cable length combination, and then adjusting the varactor diode capacitance to give the desired frequency. The frequency can be continuously changed over a range of ~10 % by varying the varactor diode bias. The RF output from the oscillator is rectified and fed back via an automatic gain control circuit to the gain input. This insures that the operating level of the oscillator is kept at the desired level as other parameters, e.g. frequency, cable length, etc. are changed. The NMR signal was detected by a lock-in technique. The large magnetic field was modulated by an ac field provided by a small coil surrounding the sample. The modulation amplitude was of the same order as the NMR linewidth which was typically 10 gauss. The detector AF signal is phase sensitively detected by a lock-in amplifier in phase with the modulation frequency. The resonance is observed by changing the field or RF frequency until the resonance condition $f=\gamma_{Al}B$ is fulfilled. A typical resonance curve is shown in Figure 3.4. The signal-to-noise ratio was typically 100. With the frequency adjusted to the center of the resonance, the output of the lock-in is also zero. Deviations from the resonance condition give rise to an error signal at the output of the lock-in which can be fed back to adjust the frequency back to the center of the resonance. Figure 3.5 shows the cir-

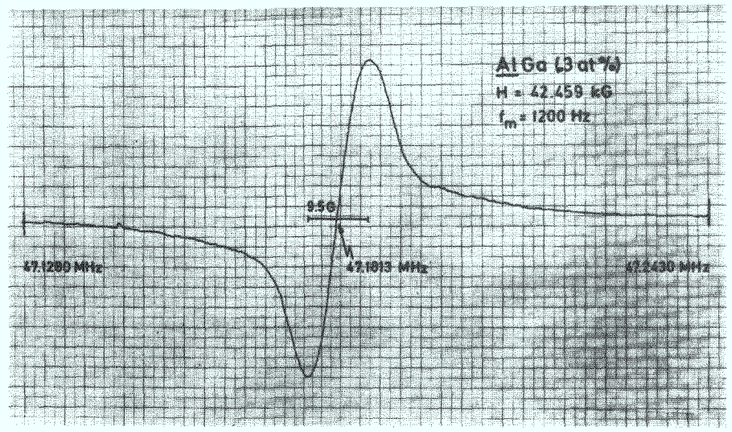

Fig. 3.4 NMR resonance signal using a sample of ^{27}Al with 0.3 at.% Ga to increase skin depth.

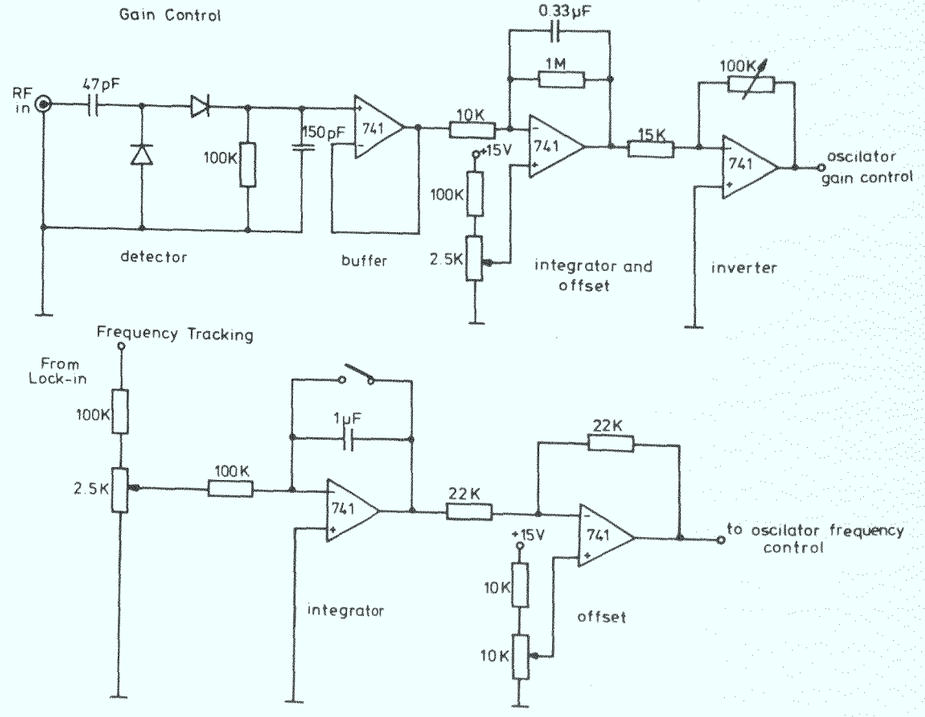

Fig. 3.5 Circuits for automatic gain control and frequency tracking for the NMR oscillator (figure 3.3).

cuit for the frequency lock and the automatic gain control. Using the frequency lock the oscillator would follow a changing field. This feature means that the resonant frequency could simply be read from a counter, as for example, the position of the NMR coil was changed to map the field profile in the magnet. The material used for the NMR probe was finaly divided ($\sim$ 20 μm) aluminum powder bound by epoxy. At a given field the resonance from the ^{27}Al nuclei and from the protons in the epoxy could both easily be observed by changing the oscillator frequency. In this way the ^{27}Al resonance could be accurately calibrated against the proton resonance. The result was

$$\gamma_{^{27}Al} = 1.11122 \pm 0.00002 \quad MH_z/kG$$

using $\gamma_H = 4.2576\ MH_z/kG$ /Varian/. The linewidth of both resonances was found to be 7 or 8 gauss. The shape of the resonance was seen to be slightly asymmetric in pure Al. This asymmetry disappeared when a dilute alloy of 0.3 at.% Ga in Al was used suggesting that the asymmetry was an effect due to skin depth. Using this system the field could be measured absolutely with an accuracy of $5 : 10^6$.

3.1.2 Temperature measurement and control

The temperature of the helium bath in the inner dewar was determined by measuring the helium vapor pressure with a capacitance manometer from Datametrics using the "1958 He Scale of Temperature" NBS monograph 10 (1960). The accuracy of this table is $\pm$ 2 millidegrees. According to specifications the capacitance manometer gives the pressure with an absolute accuracy of 0.5 %. The corresponding uncertainty in the temperature is less than 1 mK. The temperature measurement could also be checked against the known λ transition temperature for liquid helium. The temperature corresponding to this pressure was found to be within 1 mK of the correct value of $T_\lambda = 2.172\ ^oK$. The voltage output from the pressure cell was also used to control the bath temperature. The temperature control circuit is shown in Figure 3.6. The Barocel output is compared to a present voltage correspon-

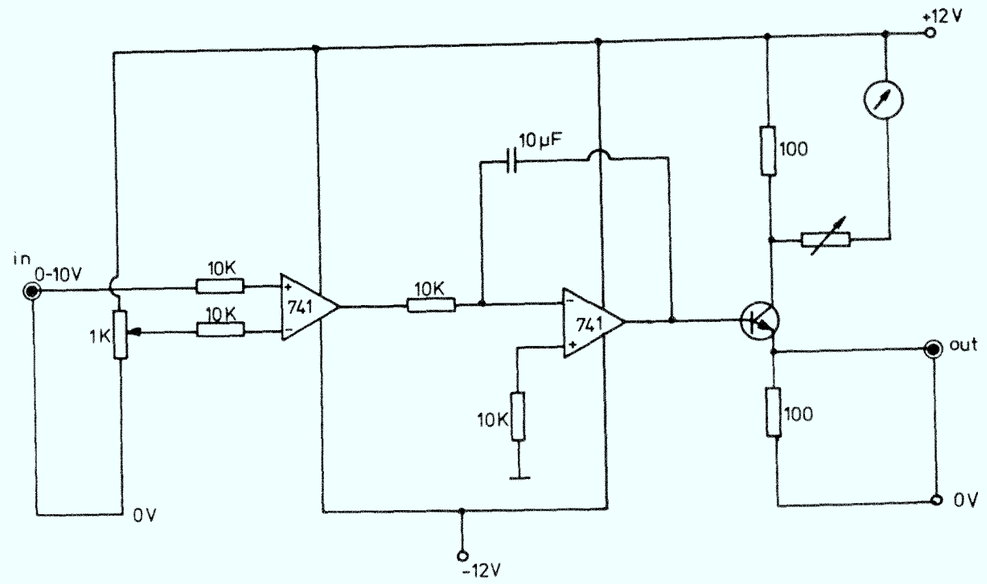

Fig. 3.6 Circuit for regulating the helium bath temperature.

ding to the required pressure. The difference signal controls the current through a heater resistor in the helium bath. The pumping rate is adjusted so that in the absence of heating the pressure decreases very slowly. In this way the temperature of the inner helium bath could be held to within a few mK of the desired temperatures.

Another point to mention is the homogeneity of the temperature in the He bath. For $T < T_\lambda$ the thermal conductivity of the He is so high, that the temperature is uniform throughout the bath. But for $T > T_\lambda$ the thermal conductivity is poor so that strong temperature gradients can exist. At the top of the liquid the temperature corresponds to the vapor pressure in the He gas above the liquid, but below the surface the temperature is higher because of the hydrostatic pressure of the liquid. Since the dHvA sample was typically 20 cm below the surface of the bath the hydrostatic pressure of the liquid above the sample is 2 torr which at $T = T_\lambda$ corresponds to a temperature 20 mK higher than that at the surface. This effect had to be taken

into account when measuring cyclotron masses. Another point to note regarding the homogeneity of the bath temperature is that for $T > T_\lambda$, the liquid density decreases as the temperature increases. Therefore when warming up the bath from a lower temperature to a higher temperature the liquid above the heater resistor will mix by convection while that below the heater being more dense will stay at the lower temperature. Because of this the heater must be located below the level of the sample when measuring above T_λ.

3.1.3 Orientation of the sample in the magnetic field

The sample holder was constructed so that the sample could be rotated through 360° about an axis perpendicular to the field direction. (See figure 3.1) In addition the whole coil assembly with sample could be tipped through several degrees about an axis normal to the rotation axis and the field direction. The samples were prepared so that the axis of the sample was close (within 1°) to the <110> crystallographic direction. By rotating, the sample could be oriented in any direction in a plane (110). This plane contains the three symmetry directions <100>, <110>, and <111>. Because of difficulty in orienting a small sample within the sample holder, in general the axis of rotation and the axis of the sample <110> differed by a few degrees. The tilt setting was used to compensate this so that all measurements were made with the field in the plane (110). The samples were oriented within the cryostat by means of the dHvA effect itself. As a result of the anisotropy of the Fermi surface, the cross sectional areas and hence dHvA frequencies depend on the orientation of the sample in the field. If the dHvA signal is plotted against the angle as the sample is slowly rotated in a static magnetic field, a pattern of oscillations is obtained. (See figure 3.7.) This pattern is symmetric about the direction <100> and <110>, and at symmetry directions $\partial F/\partial\theta = 0$. Figure 3.8 shows on an expanded scale the angular dependence of the dHvA signal for (a) the tip and (b) the rotation adjustment. By setting these adjustments to the center of the patterns the sample can be oriented to within .05 degrees of the symmetry directions.

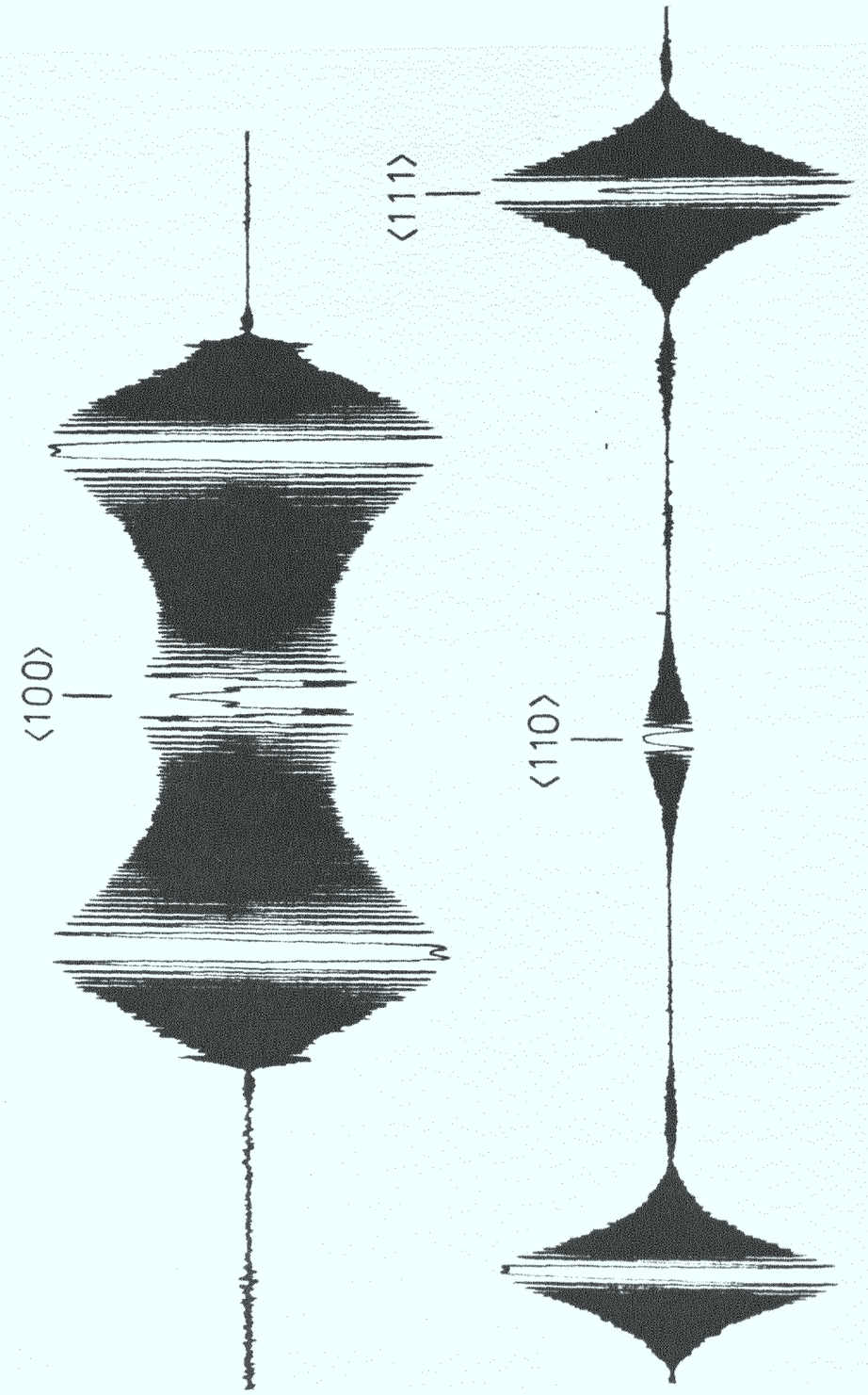

Fig. 3.7 Recording of dHvA signal versus orientation of a Cu sample in the magnetic field in a plane (110).

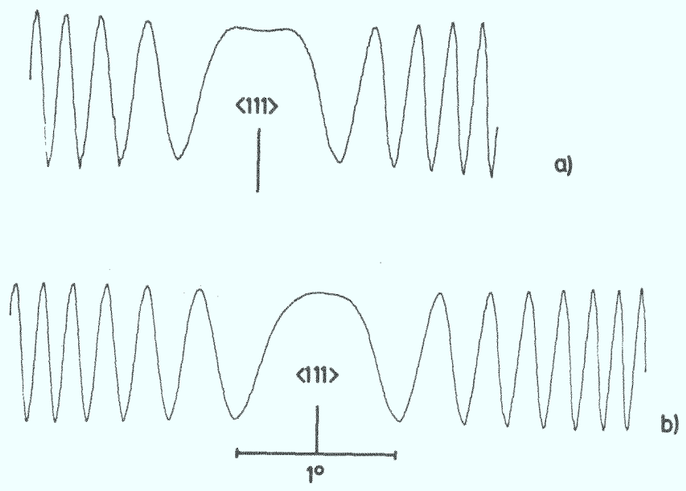

Fig. 3.8 dHvA signal from the belly orbit recorded as the tilt adjustment (a) and then the rotation adjustment (b) were swept through the setting for the crystal direction <111> parallel to the magnetic field.

The rotation pattern also proved to be a sensitive test for the quality of a crystal. Samples which were not good single crystals as a result of having been strained or containing low angle grain boundaries etc., gave rotation patterns very different from that of a good crystal. The lack of symmetry in the pattern near the ⟨100⟩ or ⟨110⟩ directions, or presence of beats in the pattern was evidence that the crystal was not good.

3.1.4 Dingle temperature measurements: Pitfalls to avoid

After orienting a sample in the required direction the Dingle temperature for that orbit is determined by measuring the dHvA amplitude at several field values with the temperature kept constant. The Dingle temperature is then given by the slope of

$$\ell n\left[M_1 \sqrt{B}\ \sinh\left(\frac{\alpha Tm_c}{Bm_o}\right)\right] = -\left(\frac{\alpha Xm_c}{Bm_o}\right) + \text{const}$$

fitted by least squares. Since several effects can give rise to a field dependence of the amplitude a few precautions are necessary to insure that the measured Dingle temperatures give meaningful information about the scattering.

i To insure that the modulation field is uniform throughout the sample the skin depth δ must be greater than the thickness of the sample. In high purity Cu samples the conductivity at He temperature is so large that very low modulation frequencies must be used.
The skin depth δ equals $(\pi\sigma f\mu\mu_o)^{-1/2}$. For pure Cu the conductivity σ is about 10^9 $(\Omega cm)^{-1}$, the permeability $\mu \cong 1$, so that for f = 30 Hz the skin depth δ = 0.3 mm. Typically the sample diameter d is 1 mm, so even at a frequency as low as 30 Hz skin depth can be a problem.
When $\delta \lesssim d$ the modulation field within the sample decreases in amplitude and changes in phase as the depth from the surface increases. Therefore the effective volume of the sample and hence the signal is reduced and the phase of the dHvA signal is shifted. In a magnetic field the conductivity decreases (for pure polycrystalline Cu σ is reduced by a factor of 4 at 30 kG) and the skin depth is correspondingly larger. This gives rise to a spurious field dependence of the dHvA amplitude which can cause errors in Dingle temperature measurements. The field dependent (and orientation dependent) phase shift of the dHvA signal can be used to determine if skin depth is a problem.
In the present experiment it was seen that skin depth phase shifts were present with pure samples ($\rho \sim 0.5$ nΩcm) but not in samples containing hydrogen ($\rho \sim 5$ to 20 nΩcm). Other tests for skin depth are to check that the dHvA amplitude is proportional to the modulation frequency f and to check for field dependence of the amplitude of the fundamental (1ω) component of the voltage induced in the pick-up coil. In pure samples where one expects small Dingle temperatures, measurements gave linear

Dingle plots and typical values of X = 0.05 ^{o}K. Skin depth was therefore not seriously affecting measurements on the pure samples, and was therefore not a problem in the samples containing hydrogen.

ii As can be seen in the L-K equation the dHvA oscillations are a sum of harmonic components. If the damping term is small enough the higher harmonics will be significant and the peak to peak amplitude of the oscillations will not give M_1. These amplitudes can be measured by Fourier analysis. The problem can also be avoided by measuring at a temperature high enough that the higher harmonics can be neglected. For the second harmonic to be smaller than 5 % of the fundamental

$$\exp\left(-\frac{\alpha m_c (T+X)}{B m_o}\right) < .05$$

or

$$\frac{m_c}{m_o}(T+X) > 1 \ ^{o}\text{K for B} \sim 50 \text{ kG}$$

iii Another problem which can arise if the damping terms are too small is that of magnetic interaction (MI). As pointed out by Schoenberg /3.5/, the effective field within the sample is $\underline{B} = \mu_o(\underline{H} + \underline{M}(B))$. Thus the oscillatory magnetization is given implicitly by

$$\hat{M} = M_1 \sin\left(2\pi\left(\frac{F}{\mu_o(H+\hat{M})} - \gamma\right) \mp \frac{\pi}{4}\right)$$

where only the 1st harmonic component is considered for simplicity. For a given dHvA period the waveform will become more distorted towards a sawtooth waveform for larger amplitudes. If the oscillatory amplitude becomes comparable with the period $\mu_o M_1 \sim B^2/4F$ the amplitude will be affected. In the extreme limit of MI the waveform becomes a sawtooth wave with an amplitude $M_1 = B^2/2\mu_o F$ (B^2/F is the period in B).
The easiest way to detect the presence of magnetic interaction

is to observe the dHvA waveform with the modulation current reduced so that the derivative of the waveform is seen. A strongly non-sinusoidal waveform is characteristic of MI. In practice, the problem can be avoided by making the measurement at a temperature high enough that MI effects are absent. Since it is the ratio of amplitude/period which is important it is better to reduce the amplitude by increasing the temperature than by reducing the field since the latter also reduces the period like B^2. Also this means that MI is more of a problem with high frequency orbits such as belly orbits.

iv Phase smearing

Because of the high phase $\xi \cong 2\pi F/B$ of the dHvA effect under normal experimental conditions, relatively small changes in F or B over the sample volume can give rise to phase differences of the order unity over the sample. Since the dHvA signal is the sum of local contributions, such phase differences will cause a reduction in the measured amplitude.

$$\frac{\delta\xi}{\xi} = -\frac{\delta B}{B} + \frac{\partial \ell n F}{\partial \theta}\,\delta\theta + \frac{\partial \ell n F}{\partial c_i}\,\delta c_i \qquad (3.9)$$

δB is the difference in magnitude of the field over the sample, $\delta\theta$ is the difference in angle between field and crystal orientation due to mosaic structure, or field directional inhomogeneity, and δc_i is the inhomogeneity in impurity concentration of a dilute alloy.

Since the terms on the right of eq. (3.9) are roughly field independent, the phase difference $\delta\xi$ is proportional to ξ itself. That is, reductions in amplitude due to phase smearing are field dependent. This can give rise to errors in the measurements of Dingle temperature such as curved Dingle plots. The condition for negligible phase smearing is $\delta\xi << 1$ over the sample. For copper this condition means:

a field homogeneity

$$\frac{\delta B}{B} << \frac{1}{\xi} = \begin{cases} 1.6 \cdot 10^{-5} & \text{for bellies} \quad H = 60\ kG \\ 2.2 \cdot 10^{-4} & \text{for necks} \quad H = 30\ kG \end{cases}$$

This condition is met in our magnet.

b orientational inhomogeneity
There are 6 orbits in the (110) plane for which $\partial F/\partial\theta = 0$. These are the 5 orbits for the field in symmetry directions and a belly orbit 16^{o} from (100) (turning point belly). For these orbits phase smearing from orientational inhomogeneity is not a great problem. For other orbits $\partial F/\partial\theta \neq 0$ and this term becomes important.

It can be shown /3.3/ that if the distribution of orientations is Lorentzian then the Dingle temperature will be enhanced by an amount

$$X = \left(\frac{2\pi\beta m_o}{\alpha m_c}\right) \frac{\partial F}{\partial\theta}$$

where β is the Lorentzian half width of the angular distribution.

The following table gives values for the angular spread β which would give rise to a Dingle temperature enhancement of $\Delta X = 0.1\ ^{o}K$ for some 'tipped' orbits (specified by the angle from <100> axis in the {100} plane).

Orbit	$\frac{\partial F}{\partial\theta}$ (10^6 G/degree)	$\beta(\Delta X = 0.1\ ^{o}K)$ (arc sec)
B9	0.38	29
B65	2.05	6
N65	0.27	15
D85	0.97	11

This shows that the quality of the crystal is very important.

c inhomogeneous impurity concentration: Typically $\partial(\ell nF)/\partial c_i \sim 1$ $(at.fract)^{-1}$ /2.21/ condition (3.9) is satisfied if $\delta c_i << 2 \times 10^{-5} = 20$ ppm.

3.2 Samples used in the investigation

3.2.1 Pure samples

The copper crystals used in the experiment were grown in our material development group by Dr. W. Uelhoff, Mr. M. Abdel Fattah and Mr. G. Hanke. The material from which the crystals were grown was 99.999 % pure ASARCO copper. They were grown by the Czochralski technique as cylinders (1.0 ± 0.1) mm in diameter and 10 cm long. The crystals were cut into (5 ± 1) mm long samples by an electrolytic layer saw technique /3.6/. Counting of etch pits gave a dislocation density of $< 10^3$ cm^{-2}. The mosaic spread was very low (< 10-20 sec) as determined from the width of the Bragg peak using a gamma diffractometer with the 411 keV gold line. All crystals were oriented with the direction <110> along the cylinder axis. The residual resistivity of the samples was 0.6 nΩcm. One of the best tests for the quality of the crystals was the dHvA effect itself. As discussed earlier, the Dingle temperature for orbits for which $\partial F/\partial\theta \neq 0$ are sensitive to small mosaic spreads. Measurements in the pure crystals gave typically the following values

orbit	X (°K)
B ⟨111⟩	0.04 ± 0.01
B TP	0.04 ± 0.01
N ⟨111⟩	0.02 ± 0.01
D ⟨110⟩	0.05 ± 0.02
B 51.74	0.05 ± 0.01
B 65	0.06 ± 0.01

This shows that:

a These low Dingle temperatures are due to the impurities which produce a residual resistivity. The contribution due to dislocations can be neglected.

b The mosaic spread is small $\lesssim$ 5 sec.

c Skin depth is not causing large errors.

3.2.2 Solubility, resistivity, diffusion, and precipitation of H in Cu

From the metallurgical standpoint the most important properties of hydrogen in copper are that it dissolves endothermically and diffuses rapidly.

By heating a copper sample in a hydrogen atmosphere, concentrations up to a few hundred atomic ppm can be dissolved. The equilibrium concentration of dissolved hydrogen c_H is given by

$$\frac{c_H}{c_o} = \left(\frac{P}{P_o}\right)^{1/2} \exp\left(-\frac{\Delta H_s}{k_B T}\right)$$

where $c_H(T_m) \equiv c_o \exp(-\Delta H_s / k_B T_m)$ is the concentration dissolved in thermal equilibrium at the melting point T_m = 1083 ^oC of copper at P_o = 1 atmosphere (definition of c_o) and ΔH is the enthalpy of solution.

The equilibrium concentration of H in Cu as a function of temperature is shown in figure 3.9. The circles represent measurements made in the course of the present work. Copper samples which had been quenched from equilibrium at higher temperatures (from 500 to 800 ^oC) were then outgassed in an evacuated chamber to determine their hydrogen content. Details of the loading and extracting procedure are given in the next section. The samples used were Czochralski grown single crystals from 99.999 % pure ARSACO Cu (residual resistivity 1 nΩcm). The crystals were larger (2 mm dia. x 10 mm long, 0.27 gram) than those used in the dHvA measurements. At each temperature samples were

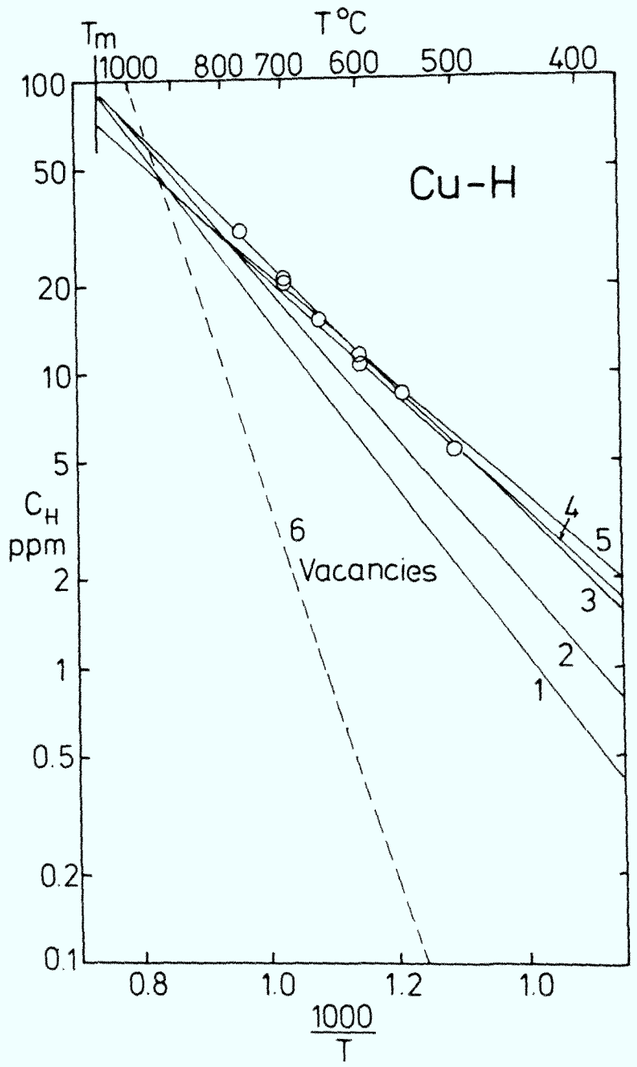

Fig. 3.9 Equilibrium concentration of hydrogen in copper (P = 1 atm) as reported by various authors. The circles are measurements discussed in the text to which curve 3 has been fitted. For comparison curve 6 shows the equilibrium vacancy concentration for copper. For vacancies the value of 200 ± 50 ppm for the concentration at the melting point determined by Simmons and Balluffi /3.19/ has been used. For the energy of formation for vacancies the more recently determined value of 1.29 ± .02 eV /3.18/ has been used. Other references are
Curve 1 /3.14/
2 /3.15/
4 /3.16/
5 /3.17/

loaded at several different pressures up to 90 atm. It was found that the concentration at each temperature was proportional to $\sqrt{P}$ in accordance with Sieverts law (figure 3.10). This clearly shows that the hydrogen dissolves as single atoms in the copper lattice. At each temperature the concentration reduced to one atmosphere was obtained from the slope of c(T,P) plotted versus $\sqrt{P}$. A least squares fit to the data gives ΔH_S = 0.44 ± 0.02 eV for the enthalpy of solution and 92 ± 5 ppm for the equilibrium concentration at the melting point for one atmosphere.

Resistivity

While making the solubility measurements the resistivity of hydrogen in copper was also measured. The residual resistivity was measured before and after loading. The resistivity plotted versus concentration is linear with a slope of ρ_H=1.50±.05 μΩcm/at.% (figure 3.11). The loading temperatures were low enough that the resistivity due to quenched in vacancies was negligible compared to that of the hydrogen. The linear dependence of the resistivity

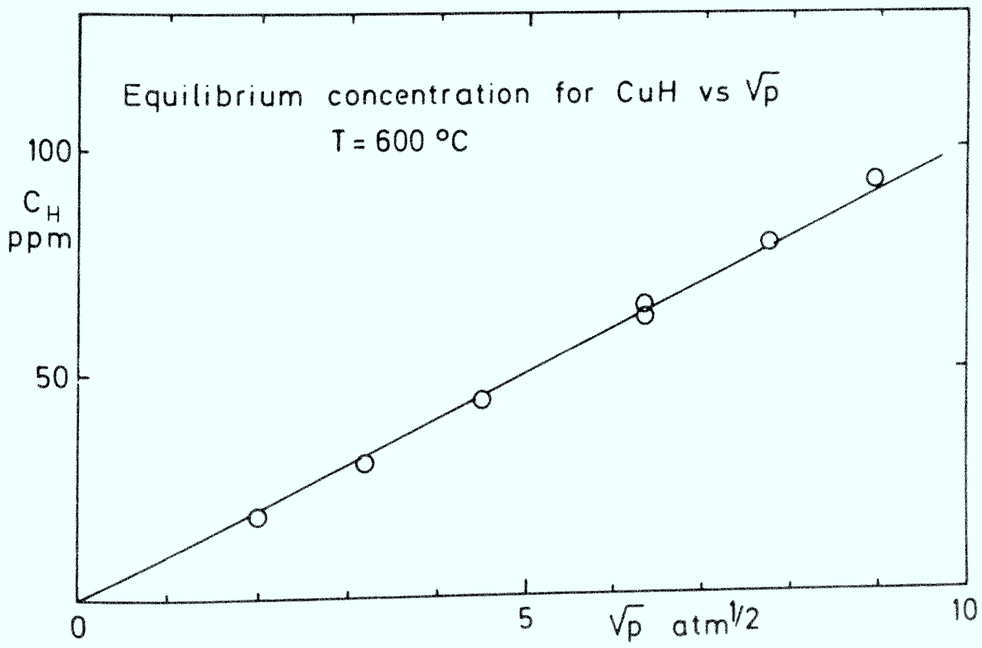

Fig. 3.10 Measurement of pressure dependence of equilibrium concentration of H in Cu showing linear dependence on $\sqrt{P}$.

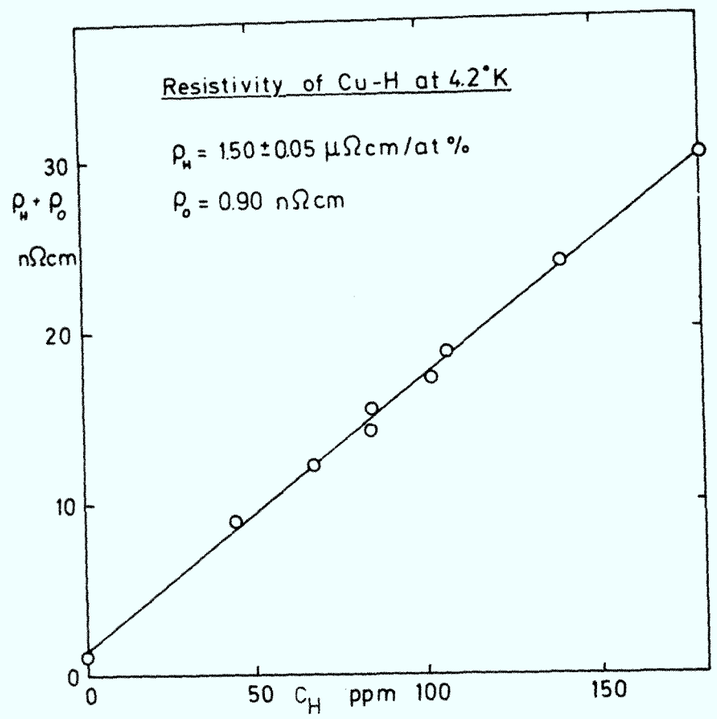

Fig. 3.11 Residual resistivity of a copper single crystal as a function of concentration of dissolved hydrogen.

on the hydrogen concentration shows that the samples were homogeneously loaded.

Diffusion

The diffusion coefficient for H in Cu is given by

$$D = D_o \exp(-E_m/kT)$$

where E_m is the energy of migration. Values for E_m and the prefactor D_o have been determined by measuring the outgassing rate for hydrogen loaded samples as a function of temperature /3.20/ giving

$$E_m = 0.403 \pm .003 \text{ eV}$$

$$D_o = 1.13 \pm 0.04 \times 10^{-2} \text{ cm}^2/\text{s}$$

The low value of 0.40 eV for the migration energy of hydrogen compared to 2.07 eV for the activation energy of self-diffusion in copper below 700 ^{o}C /3.7/ and 0.70 eV for vacancy migration /3.8, 3.9/ in copper shows that the diffusion of the hydrogen in Cu is independent of vacancies and must therefore be between interstitial sites. Neutron diffraction experiments in the fcc metals Ni, Pd show that H occupies the octahedral interstitial site in the hydride phase /3.10, 3.11/. Although it has not been directly shown it is probable that H in Cu also occupies the octahedral interstitial site.

Precipitation

By an appropriate quenching technique, where the sample is quickly cooled to a low enough temperature, the dissolved hydrogen can be frozen into the lattice. To carry out Dingle temperature measurements the hydrogen must be distributed homogeneously in the copper lattice. Because of its endothermal solubility the quenched in hydrogen forms a supersaturated solution, so that it tends to escape the lattice. An extensive investigation of the metallurgical behavior of hydrogen in copper has shown that the hydrogen precipitates from a supersaturated solution into bubbles at room temperature. In impure copper samples it can in addition be trapped by impurities /3.12/. This is illustrated in figure 3.12 where the isochronal annealing curves for two hydrogen loaded copper samples are shown. At each indicated temperature the samples were held for 15 minutes and then cooled to 4.2 K where the residual resistivity $\rho_H(T)$ due to the hydrogen was measured. The circles are the results obtained on a pure Cu single crystal containing 63 ppm hydrogen. Below 0 ^{o}C there is little structure in the recovery of the electrical resistivity. Around room temperature 90 % of the residual resistivity disappears irreversibly. This is due to the precipitation of the dissolved hydrogen into bubbles.

Electron and optical micrographs show that bubbles form at that temperature. The bubbles nucleate preferentially at grain boundaries and dislocations. They grow by dislocation production at a rate which is governed by the diffusion of hydrogen to the bubbles. Figure 3.13 shows a transmission electron micrograph of hydrogen bubbles about 0.3 μm in diameter. The punched-out prismatic loops along [011] formed during growth are clearly visible. Also shown in figure 3.12 is the isochronal annealing curve of a less pure copper sample measured by Lucasson and coworkers /3.13/. The sample contained about 20 ppm of hydrogen and about 100 ppm of unspecified impurities (residual resistivity 200 without hydrogen). In addition to the precipitation stage around room temperature, they observed a second stage around -120 ^{o}C followed by an increase in the resistivity between -100 and -50 ^{o}C. This was identified in /3.12/ as trapping and detrapping of the hydrogen at the impurities. The low temperature recovery stage clearly demonstrates that the hydrogen becomes mobile around -130 ^{o}C as one expects from the diffusion coefficient. The reason why the hydrogen precipitates first at room temperature although it is mobile at much lower temperatures as seen from trapping is that the number of traps $\sim 10^{19} cm^{-3}$ is much greater than the number of bubbles ($\sim 10^{9}$ cm^{-3}) which depends on the dislocation density. The samples used for dHvA investigations were therefore quenched to -150 ^{o}C to insure a homogeneous distribution of the disolved hydrogen.
The quench was quick enough to avoid precipitation during the quench.

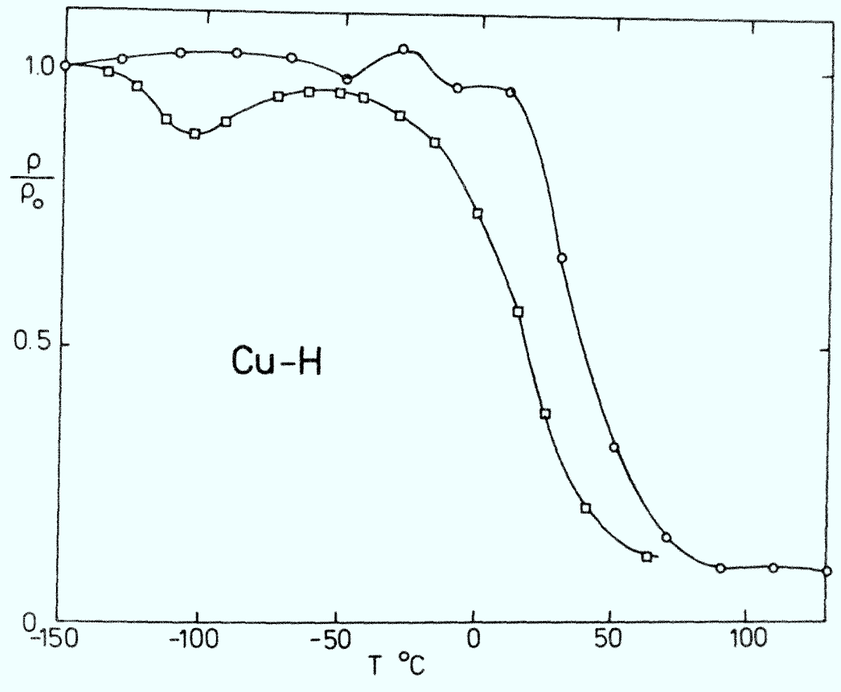

Fig. 3.12 Isochronal annealing of resistivity due to hydrogen in copper. The fraction of the initial quenched in resistivity remaining after annealing is plotted versus the annealing temperature.

○ Copper single crystal quenched from 600 °C and 30 atm.
c_H = 63 ppm, t = 15 min., c_v = 0.5 ppm

□ Copper wire quenched from 735 °C and 1 atm.
c_H = 20 ppm from Budin, Lucasson and Lucasson /3.13/. The temperature coordinate for these points has been adjusted to correspond to an annealing period of 15 minutes so that they can be compared with the other measurement.

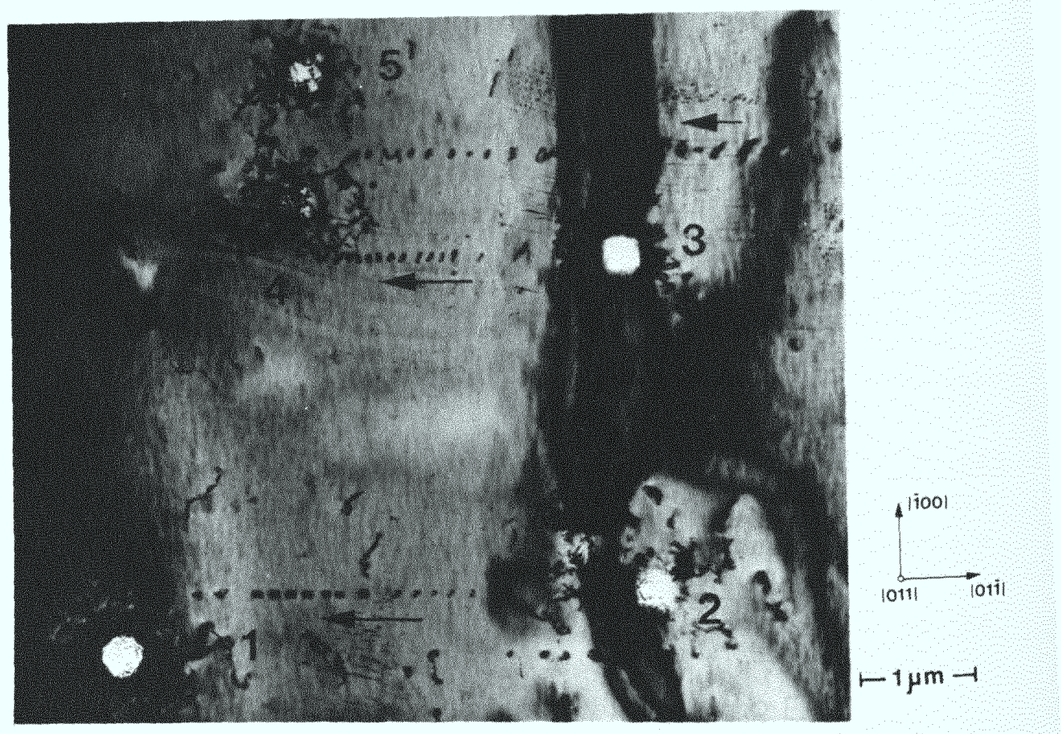

Fig. 3.13 TEM micrograph of hydrogen bubbles (as labled 1 to 5) in copper. Note punched-out prismatic loops along [110] (direction marked by arrows). The bubbles are surrounded by dense tangles of dislocations.

3.2.3 Hydrogen loading and extracting

Figure 3.14 shows a diagram of the apparatus used for loading samples with hydrogen. The loading was done inside a quartz tube 10 mm inside dia., 16 mm outside dia. which was surrounded by a small oven. With this system loading could be carried out for hydrogen pressures up to 50 atmospheres and temperatures up to near the melting point of Cu. The sample itself is held inside a copper cylinder during loading. This was supported by stiff molybdenum wire attached to a piece of iron held in place by a magnet outside the quartz tube. The purpose of the copper block is to prevent the sample cooling while falling from the oven to the quench bath. After the sample had reached equilibrium it was quenched by removing the magnet, allowing the copper block to fall. Just above the quench bath the copper block was stopped by a ledge, but the sample continued downwards into the quench bath.
From the diffusion coefficient one can estimate that below -140 ^{o}C the hydrogen is essentially immobile (jump rate $\nu = D/a^2 \sim 5 \cdot 10^{-3}$ s^{-1}). Therefore the liquid used for the quench bath was isopentane (2- methylbutane, melting point -160 ^{o}C, boiling point 30 ^{o}C) at -150 ^{o}C. The samples were not allowed to become warmer than -150 ^{o}C after quenching until all measurements were completed. After measurements were completed the hydrogen content of the samples could be measured by a heat extraction technique in which the sample was heated in an evacuated volume and the hydrogen evolved determined from the pressure.

The layout of the extraction apparatus is shown schematically in figure 3.15. It was constructed from high vacuum components using only metal and glass to reduce outgassing from the system. The procedure for measuring the hydrogen content of a sample was as follows. The sample was placed in the quartz tube and the system evacuated by a backing pump. Between the backing pump and the high vacuum part was a zeolite trap to prevent contamination from the pump. After rough evacuation the system was further evacuated to $< 10^{-7}$ torr by an ion getter pump. The end of the quartz tube (but not the sample) was then outgassed at

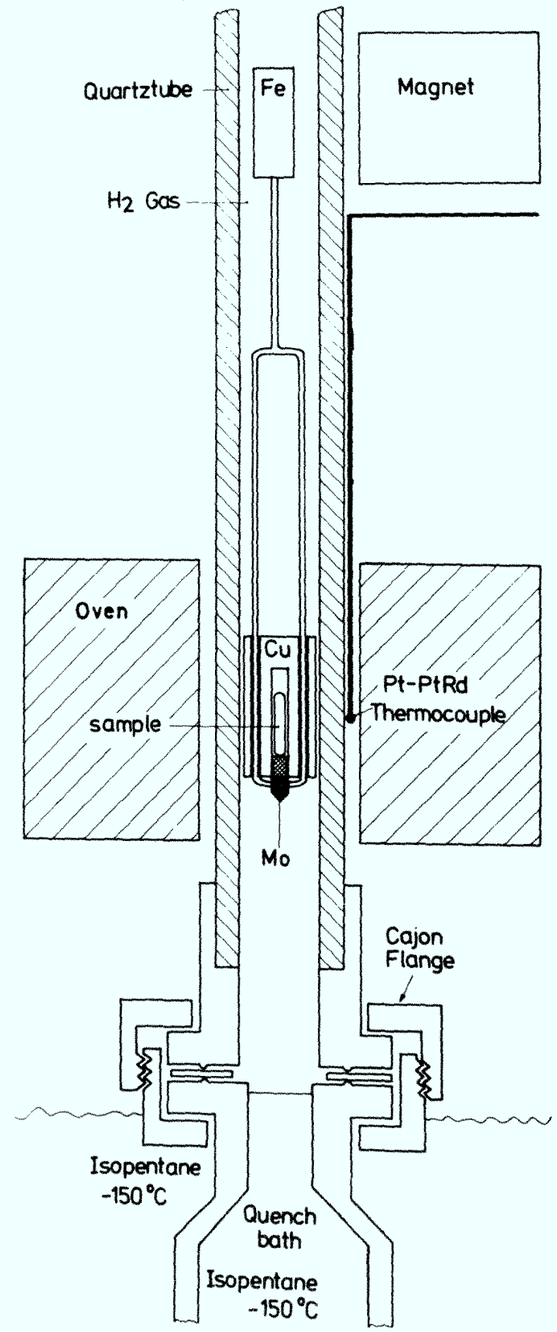

Fig. 3.14 Diagram of apparatus used to load Cu samples with hydrogen as described in the text.

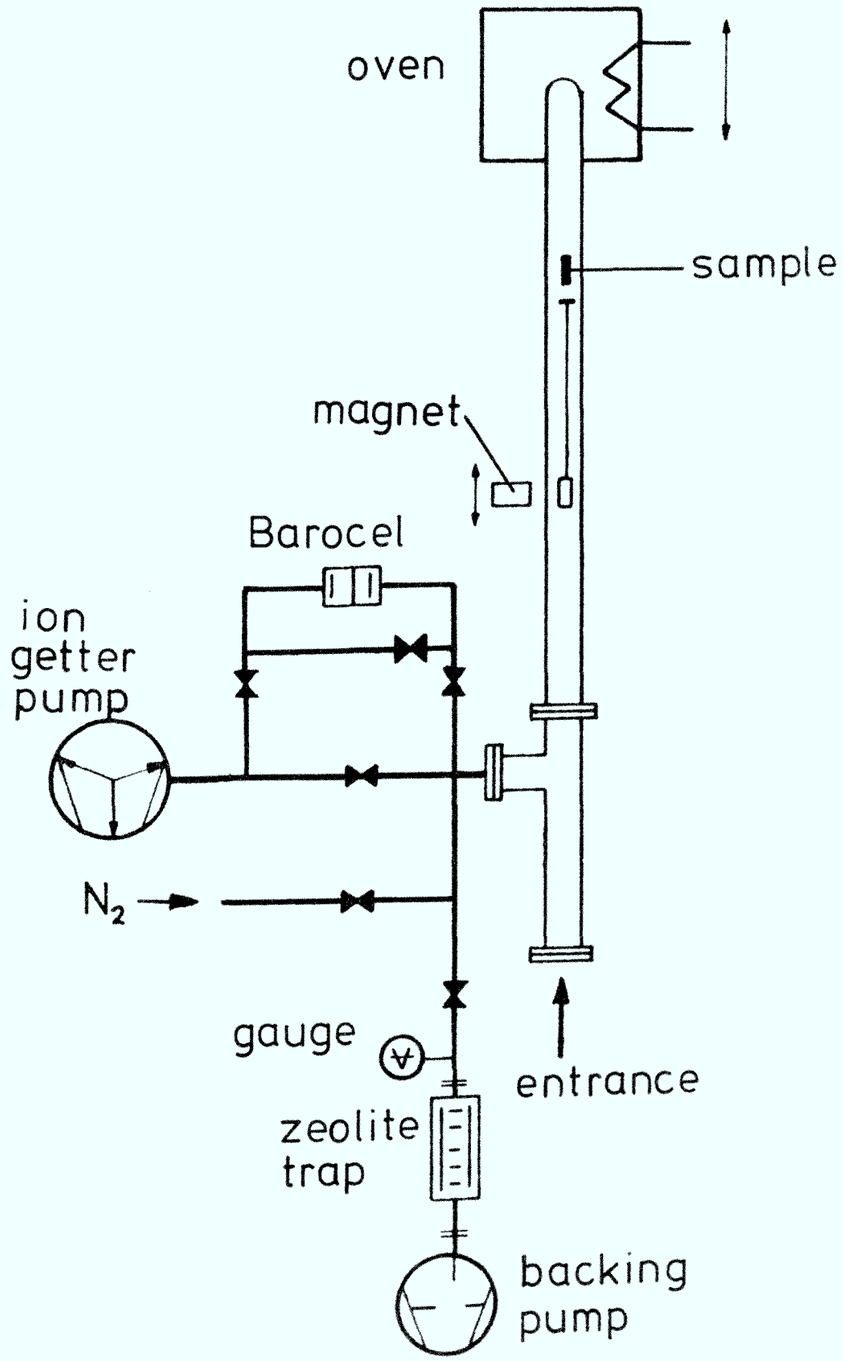

Fig. 3.15 Schematic diagram of hydrogen extraction apparatus

1000 ^{o}C for several minutes to remove gas adsorbed on the glass. The oven temperature was then reduced to 800^{o}C. The system closed off from the pump, and the sample was pushed into the hot end of the tube by a magnetic shover. The pressure was measured by a Barocel capacitance manometer (10 torr maximum range) and recorded versus time on a chart recorder.

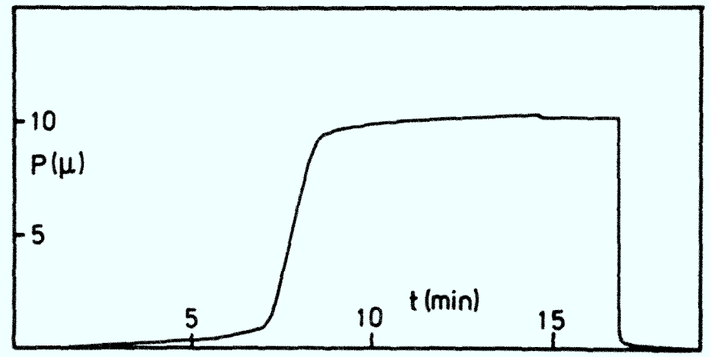

Fig. 3.16 Recording of the pressure cell reading during an extraction run for a 26 mg copper sample containing 110 ppm of hydrogen. The sample was pushed into the oven at the 5 minute mark.

Figure 3.16 shows a typical extraction curve. The amount of hydrogen evolved from the sample was then determined from the pressure. The largest source of error was due to stray outgassing. By taking care to avoid contamination and by outgassing the system at higher temperatures prior to an extraction run, pressures could be determined with an accuracy of $\sim 10^{-3}$ torr. Since the extraction volume was $\sim$ 50 cm^3 this corresponds to $\sim 5 \cdot 10^{-9}$ grams of H_2 or 1 ppm in a 0.3 gm Cu sample. The time for a sample to reach equilibrium during loading or extracting can be estimated from the diffusion coefficient. For a cylindrical sample of radius r the time to reach equilibrium is r^2/D.

§4 De Haas van Alphen lifetime measurements in CuH
Experimental results

The samples were loaded with hydrogen by heating in a hydrogen atmosphere at temperatures between 600 ^{o}C and 730 ^{o}C and pressures of 4 to 45 atmospheres, and then quenching to -155 $\pm$ 5 ^{o}C in an isopentane quench bath. The sample preparation is described in detail in section 3. After quenching, the excess isopentane was removed from the sample and the sample was then placed in liquid nitrogen. This was carried out in a specially designed cold chamber and was done in such a way as to eliminate any possibility of the sample becoming warmer than -150 ^{o}C. The time from quenching until the sample was in liquid nitrogen was typically 20 minutes, during which the sample temperature was between -150 and -160 ^{o}C.

The samples (loaded with hydrogen in the way described in section 3.2.2) were placed in the dHvA sample holder and held in place by small pieces of soft cotton wool at each end of the sample. This was done under liquid nitrogen. The sample holder was then removed from the nitrogen and inserted into the cold (4.2 ^{o}K) helium cryostat. The time for this transfer ($\sim$ 5 sec) being short enough to avoid any increase in the sample temperature. The time the sample spent in liquid nitrogen before transferring to the helium cryostat was typically 20 minutes.

For each sample the Dingle temperatures were measured for 11 orbits with the field in a plane (110) by measuring the dHvA amplitude at several field values (typically eight). The Dingle temperatures were then calculated from a least squares fit of $y = \ln\left[M_1\sqrt{B}\sinh(\alpha m_c T/m_o B)\right]$ plotted versus $x = 1/B$. Typical Dingle plots are shown in figure 4.1. The values for the Dingle temperatures for the 11 samples measured are tabulated in table 4.1 the quoted errors are the standard error of the slope of the linear fit given by: for $y = ax + b$

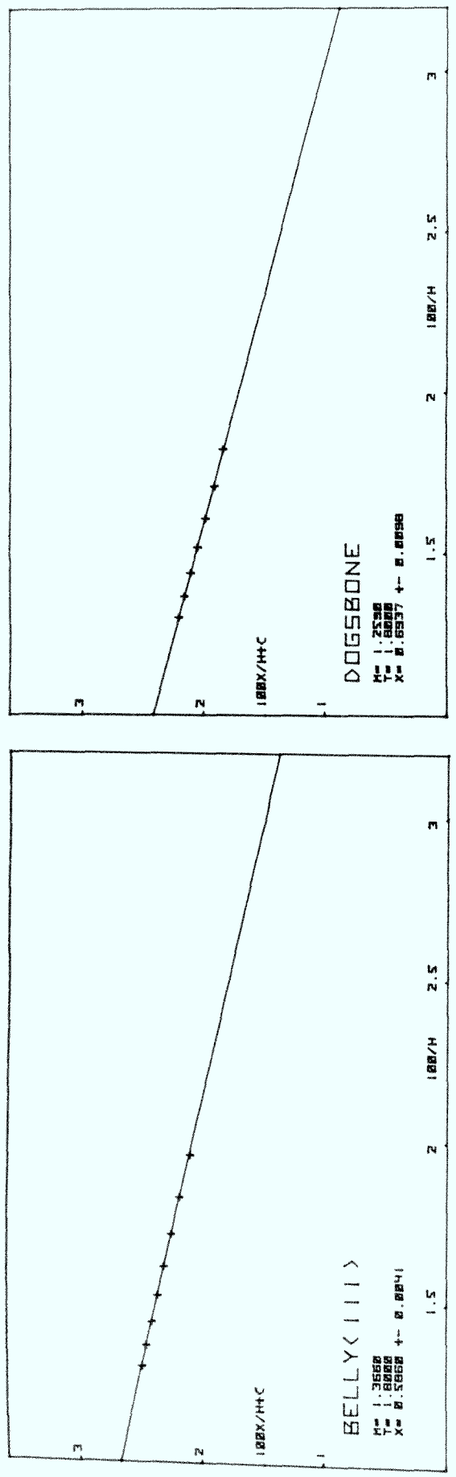

Fig. 4.1
Typical Dingle plots for Cu-H.

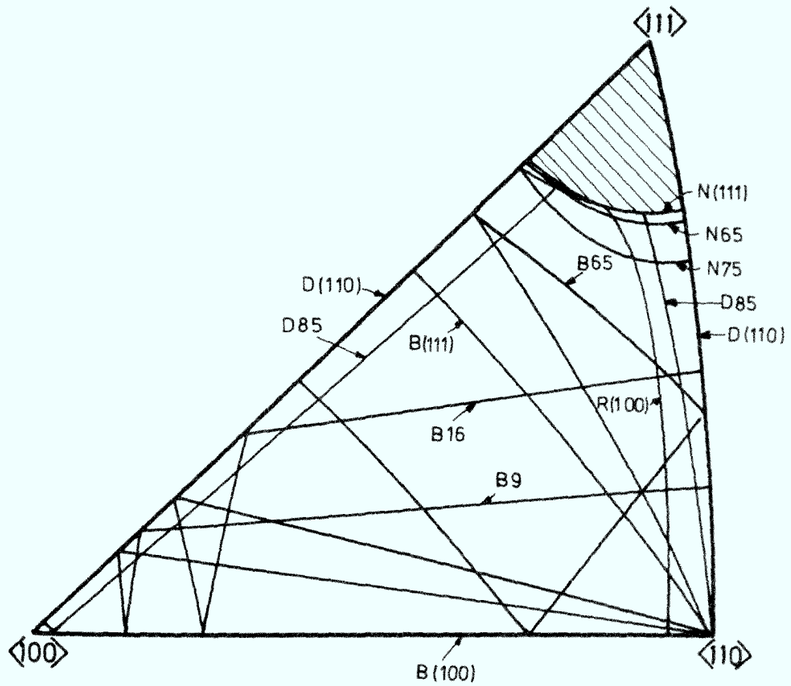

Fig. 4.2 Paths over the Fermi surface of the 11 orbits measured, shown as a stereographic projection of the basic 1/48 th of the Fermi surface.

standard error in slope is σ_a where $\sigma_a^2 = \frac{\sigma^2}{n\sum_i x_i^2 - (\sum_i x_i)^2}$

$$\sigma^2 = \frac{\sum_i (ax_i + b - y_i)^2}{n-2} \qquad (4.1)$$

The values for the cyclotron mass used in the analysis are also listed in table 4.1 /2.12/.
While making the amplitude measurements the sample temperature was kept constant. For a given orbit the temperature was chosen to be high enough to avoid magnetic interaction (MI) and higher dHvA harmonics. For the belly orbit where the most care to avoid MI must be taken the temperature was usually chosen so that the sum of the temperature and Dingle temperature was greater than 2 ^{o}K. In practice the test described in section 3.1.4

Table 4.1

Measured Dingle temperatures for Cu-H (^{o}K)

Sample	ρ_H (nΩcm)	c_H (at.ppm)	B(100)	B9	BTP	B(111)	B65	N(111)	N65	N75	D(110)	D85	R(100)
m_c			1.348 ±.002	1.323 (calc)	1.308 ±.003	1.366 ±.002	1.431 ±.004	0.445 ±.001	0.478 ±.002	0.648 ±.004	1.259 ±.002	1.288 ±.003	1.307 ±.002
158-8	0	0	0.134 ±.007	0.072 ±.004	0.091 ±.006	0.062 ±.01	—	0.123 ±.001	0.276 ±.01	—	0.188 ±.006	0.414 ±.01	0.067 ±.008
158-7	18.12	120.8	0.588 ±.007	0.644 ±.008	0.694 ±.011	0.801 ±.015	0.968 ±.007	1.549 ±.017	1.641 ±.015	1.715 ±.027	—	—	—
158-5	15.92	106.1	0.465 ±.007	0.470 ±.0035	0.545 ±.004	0.686 ±.005	0.715 ±.013	1.213 ±.009	1.234 ±.037	1.198 ±.02o	0.9715 ±.004	0.982 ±.009	1.055 ±.015
158-4	21.45	143.0	0.634 ±.004	0.676 ±.006	0.778 ±.007	1.017 ±.011	1.040 ±.01	1.720 ±.03	1.53 ±.05	1.86 ±.06	1.181 ±.02	1.17 ±.02	—
158-2	19.15	127.7	0.593 ±.007	0.688 ±.008	0.722 ±.007	0.867 ±.008	—	1.532 ±.009	1.47 ±.014	1.56 ±.05	1.163 ±.006	1.332 ±.013	1.236 ±.015
154-6	13.93	92.9	0.417 ±.005	0.444 ±.001	0.499 ±.013	0.586 ±.004	0.625 ±.01	1.055 ±.008	1.031 ±.018	0.907 ±.024	0.691 ±.01	0.707 ±.005	0.778 ±.009
154-4	3.21	21.4	0.156 ±.004	0.135 ±.004	0.187 ±.010	0.167 ±.003	0.168 ±.003	0.312 ±.006	0.342 ±.008	0.261 ±.007	0.259 ±.005	0.224 ±.005	0.176 ±.009
154-2	9.42	62.8	0.348 ±.008	0.357 ±.006	0.386 ±.011	0.432 ±.008	0.430 ±.009	0.698 ±.004	0.697 ±.012	0.576 ±.02	0.526 ±.004	0.493 ±.005	0.465 ±.002
147-5	10.42	69.5	0.278 ±.009	0.298 ±.004	0.342 ±.013	0.387 ±.003	0.414 ±.007	0.720 ±.005	0.7095 ±.005	0.677 ±.007	0.549 ±.004	0.546 ±.006	0.522 ±.01
147-6	5.03	33.5	0.173 ±.002	0.167 ±.002	0.195 ±.006	0.200 ±.002	0.458 ±.007	0.358 ±.005	0.399 ±.005	0.461 ±.007	0.276 ±.005	0.286 ±.002	0.199 ±.008
147-3	8.32	55.5	0.365 ±.004	0.366 ±.008	0.454 ±.003	0.471 ±.006	0.502 ±.009	—	—	—	—	—	0.567 ±.007
X/c_H	(^{o}K/at.%)		37.9 ±3	45.6 ±3.3	48.4 ±3.3	65.0 ±3.7	65.7 ±8.6	112.6 ±5.5	102.3 ±10.0	110.0 ±13.2	77.3 ±6.7	71.0 ±13.3	89.8 ±8.4

was used to check for MI effects and measurements were only made under conditions where MI was not affecting the measurements. Similar precautions were taken to avoid harmonic content when measuring neck oscillations in the purer samples.

In addition to the 6 orbits for which $\partial F/\partial\theta = 0$ (B(100), R(100), BTP, B(111), N(111), D(110)) five additional tipped orbits ($\partial F/\partial\theta \neq 0$) were measured so as to obtain better coverage of the Fermi surface. Figure 4.2 shows the orbits in 1/48 of the Fermi surface in stereographic projection.
After measuring the Dingle temperatures the sample holder was transferred from the dHvA cryostat to a liquid nitrogen bath. The sample was then transferred from the dHvA sample holder to a resistivity sample holder, this being done in the liquid nitrogen bath. The sample was then quickly transferred from the nitrogen bath to a liquid helium dewar where the residual resistance was measured. The sample was thus at 77 ^{o}K during this transfer process. The resistivity sample holder was then removed from the helium dewar and warmed up to room temperature where the room temperature resistance was measured. From the ratio of the resistance at room temperature and at 4.2 ^{o}K the resistivity of the sample can be obtained. Subtracting from this the resistivity of the sample before loading then gives the resistivity due to the dissolved hydrogen which is proportionel to the hydrogen concentration (ρ_H = (1.50±.05) $\mu\Omega$cm/at.%). Also shown in table 4.1 is the resistivity due to the dissolved hydrogen for each sample and the corresponding hydrogen concentration.

Finally the hydrogen content of each sample was measured by the heat extraction method described in section 3. This value was subject to rather large error however, due to the small size of the samples (typically 0.025 grams). The value 1.50$\mu\Omega$cm/at.% for the resistivity of hydrogen in copper was determined in larger samples (0.25 gm) for which the heat extraction results were considerably more accurate due to the greater amount of hydrogen. The hydrogen concentration in the

small dHvA samples was then determined from their resistivity using this value. This was found to be considerably more accurate than the results from heat extraction for the small samples. Therefore in the subsequent analysis the hydrogen concentrations as determined from the resistivity will be used.

To investigate the effect of the quench alone, one sample was quenched from an atmosphere of helium gas, but otherwise handled in the same way as the hydrogen loaded samples.
It should be remarked that the loading temperatures were relatively low. The reasons for this were firstly to insure that the concentration of vacancies quenched in with the hydrogen was as low as possible, and secondly because the lower mobility of the hydrogen during the quench gives more homogeneously loaded samples.

Figures 4.3 show the measured Dingle temperatures plotted against hydrogen concentration for the 11 orbits measured.
There are two types of error which contribute to the scatter of the measured Dingle temperatures from the linear fit against concentration.
Firstly there is the error involved in the measurement of the Dingle temperature. This is fairly well known being given by the standard error of the slope of the Dingle plot. This is the error given in table 4.1. It can be seen that this error is generally quite small. Deviations in the values obtained for repeated measurements of the Dingle temperature for the same orbit in the same sample are of this order.
Clearly this error cannot account for the scatter seen in the X v.s. c_H plots. The other source of error lies in the preparation of the samples. Although great care was taken to reduce error from this source the sensitivity of Dingle temperature measurements to strain and dislocations in the samples means that uncontrollable variations in the loading, quenching, and subsequent handling of the sample could result in variations in Dingle temperatures of the order of 0.1 ^{o}K between samples. For this reason many samples were measured in order to improve the accuracy of the determination of X vs. c_H by statistical

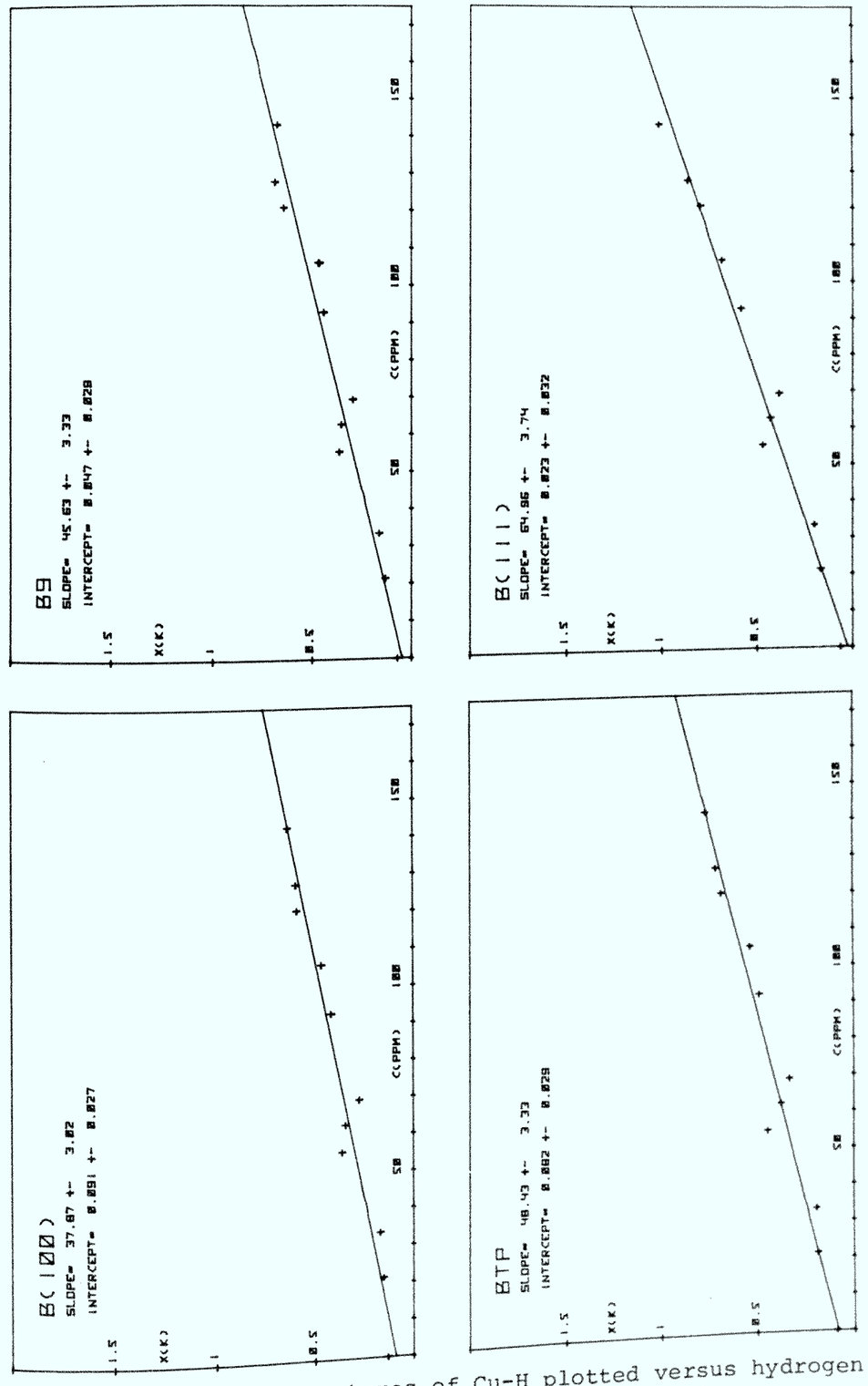

Fig. 4.3 Dingle temperatures of Cu-H plotted versus hydrogen concentration for the 11 orbits measured.

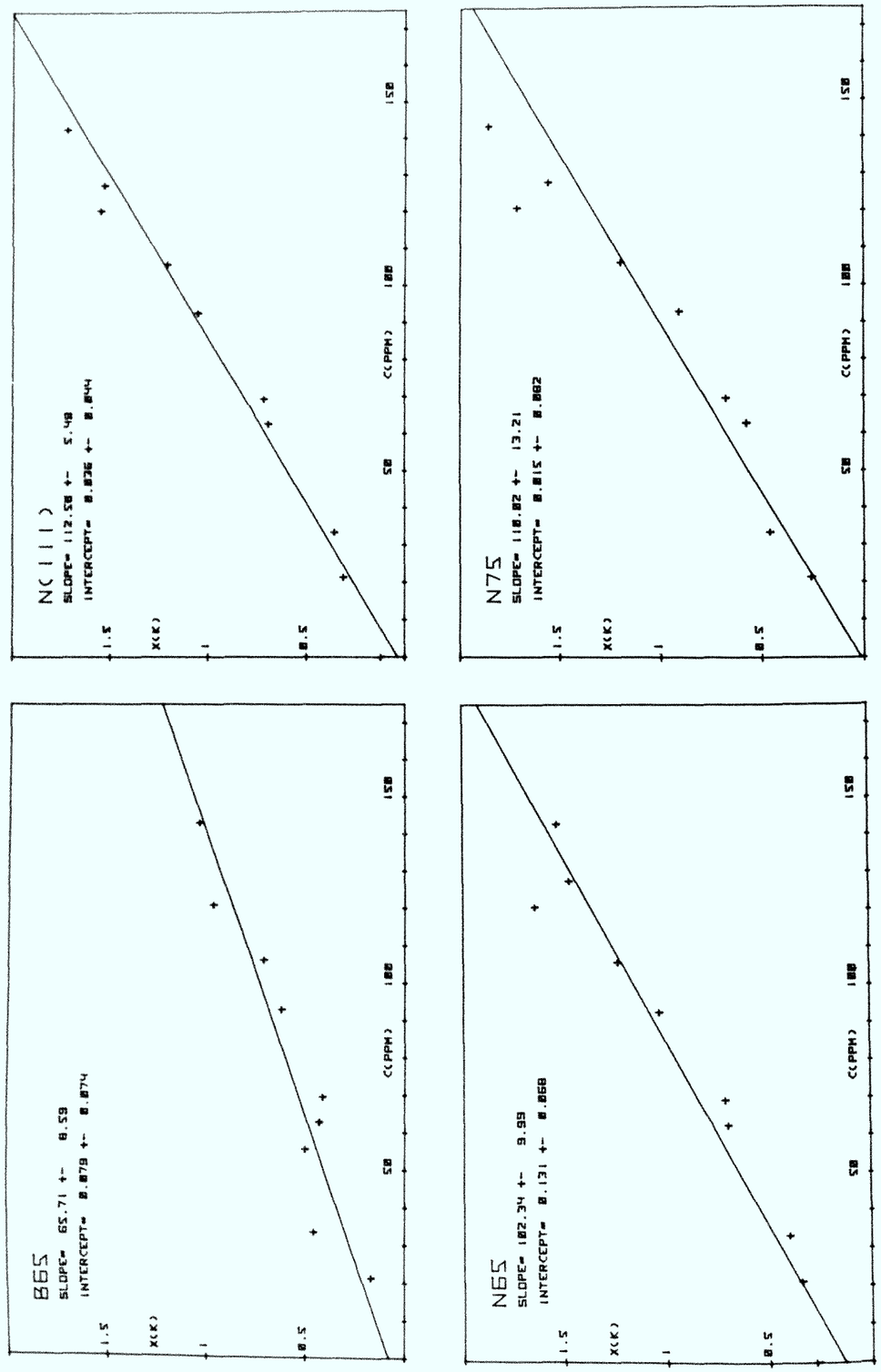

Fig. 4.3 Dingle temperatures of Cu-H plotted versus hydrogen concentration for the 11 orbits measured.

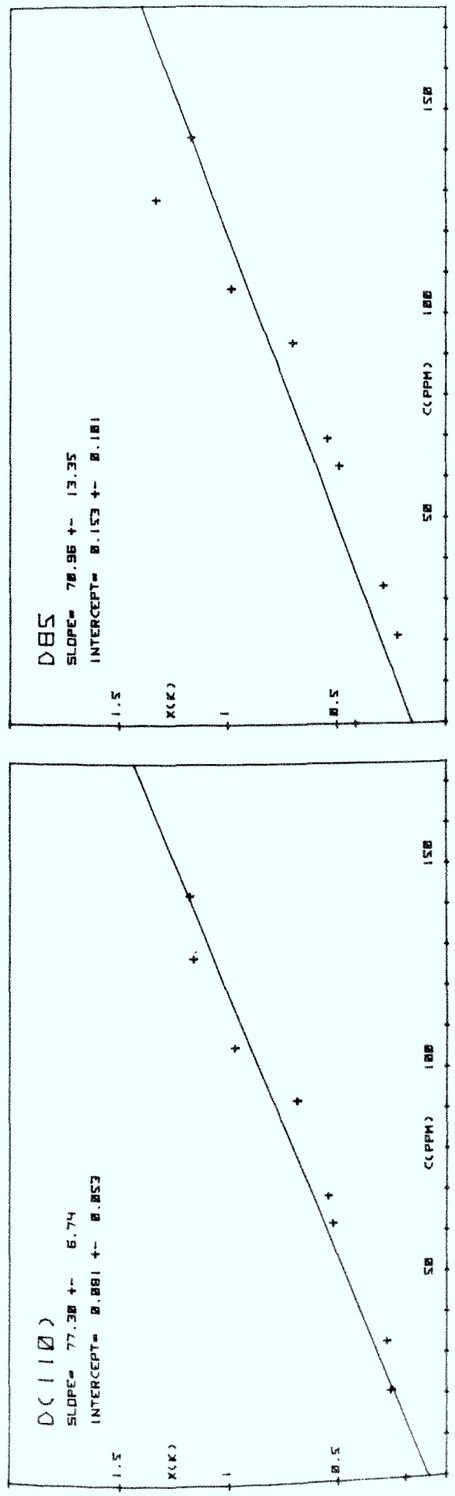

Fig. 4.3

Dingle temperatures of Cu-H plotted versus hydrogen concentration for the 11 orbits measured.

averaging. The mean scatter due to the different dislocation densities should then give rise to an offset in the intercept of the fit and an uncertainty in the slope given by the standard error of the slope, but no systematic error in the mean value of the slope. It should be pointed out that previously reported measurements of Dingle temperatures for substitutional defects in noble metal hosts usually consist of measurements at only one concentration. The reliability of such results is therefore not as good as when several samples over a range of concentrations are measured.

The Dingle temperatures for each orbit for unit concentration of hydrogen were obtained from the slope of a least squares fit of X versus concentration, the values are listed in table 4.1. For a few of the measured Dingle temperatures the Dingle plots were curved, these points were unreliable and not included in the fit of X vs. c_H.
The experimental errors of the values for X/c_H in table 4.1 are in the region of 5 to 10 % and are unavoidably larger than the errors in dHvA frequency and cyclotron mass measurements since the Dingle temperatures are much more sensitive to the condition of the samples. Also frequency and mass measurements are made on pure samples which can be prepared in a more well defined state than dilute alloys.

The results presented in table 4.1 contain the desired information about the scattering of the conduction electrons from the hydrogen. In the next section the theory discussed in section 2 is used to obtain more specific information about the scattering from the dHvA data.

§5 Discussion of the results

5.1 Local scattering rates in Cu-H

In section 2.5.3 it was shown how the local scattering rates $\frac{1}{\tau(\underline{k})}$ can be obtained from the measured Dingle temperatures and that they can be represented by a symmetrized Fourier series. This representation has been used for the analysis of the measured data. The details of this analysis are given in the appendix. It was found that the most significant fit to the data was obtained by using three coefficients in the fit. The 3-coefficient representation for the local scattering rates together with the values of the coefficients for Cu-H are:

$$\frac{1}{\tau(\underline{k})} = T_{000}+T_{110}\left[\cos(\tfrac{a}{2}k_x)\cos(\tfrac{a}{2}k_y)+\cos(\tfrac{a}{2}k_y)\cos(\tfrac{a}{2}k_z)+\cos(\tfrac{a}{2}k_z)\cos(\tfrac{a}{2}k_x)\right]$$
$$+T_{200}\left[\cos(ak_x)+\cos(ak_y)+\cos(ak_z)\right]$$

$$T_{000} = -\ 2.004 \times 10^{13}\ s^{-1}(at.\%)^{-1}$$
$$T_{110} = -19.041 \times 10^{13}\ s^{-1}(at.\%)^{-1}$$
$$T_{200} = -\ 3.601 \times 10^{13}\ s^{-1}(at.\%)^{-1}$$

Where $a = 3.6030$ Å is the lattice parameter for Cu and $\underline{k} = (k_x,k_y,k_z)$ is the vector from $\underline{k} = 0$ to the Fermi surface. The 6 term Fourier representation of Halse /2.4/ (eq. 2.15 with coefficients $C_{\ell mn}$ given in table 2.1) for the Fermi surface was used.

The local scattering rates from this fit are plotted in figure 5.1 as a contour map of the scattering rate over a stereographic projection of the basic $1/48^{th}$ of the Fermi surface. It can be seen that the scattering rate is the lowest near the <100> direction, somewhat larger in the <110> direction and largest at the neck. The maximum anisotropy is a factor of ~ 3.5 between <100> and the neck. This anisotropy reflects the systematic trend observed in the measured Dingle temperatures that values for the belly orbits increased with increasing angle from <100>. Comparison of fig. 5.1 and 4.2 shows that as the angle from <100> increases, the belly orbit comes closer to the neck where the scattering is larger.

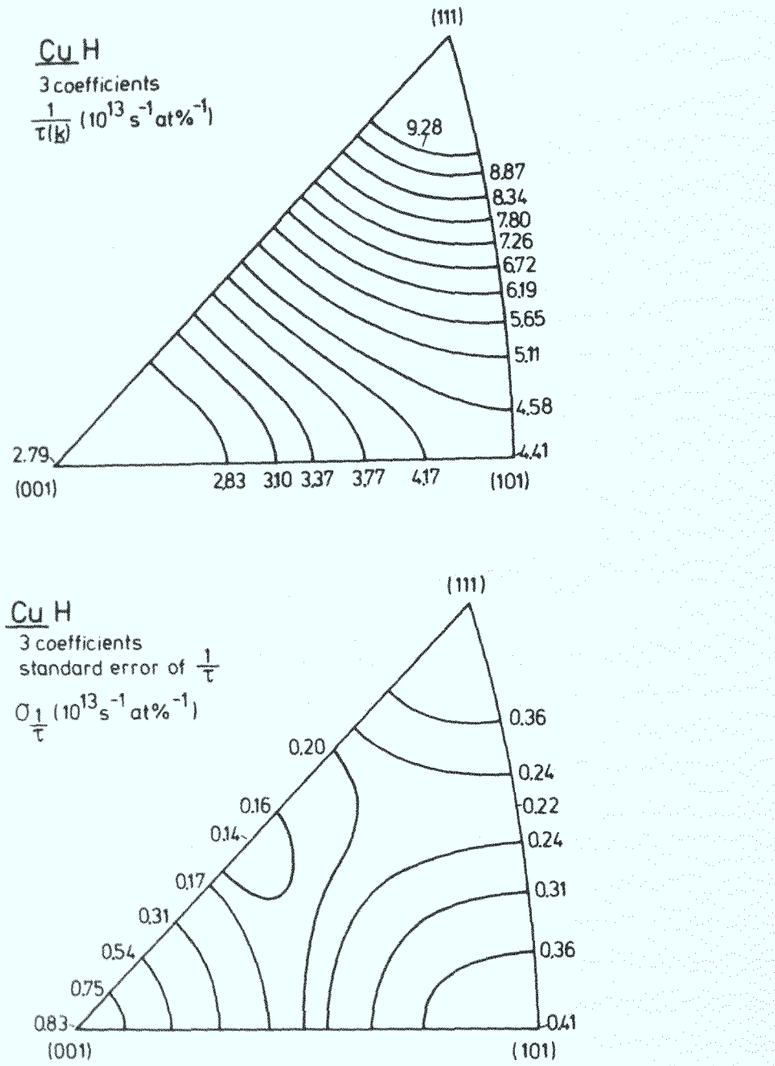

Fig. 5.1 Contour plot of the local scattering rate $\frac{1}{\tau(\underline{k})}$ for Cu-H, and the corresponding standard error, over a stereographic projection of the basic 1/48th of the Fermi surface.

5.2 Discussion of the local scattering rates in Cu-H and comparison with scattering from substitutional impurities

The anisotropy of the local scattering rates for different defects in the noble metals can be qualitatively understood from the fact that the electron wave functions change in character over the Fermi surface. That means that the probability density $|\psi_{\underline{k}}(\underline{r})|^2$ to find an electron at $\underline{r}$ in real space depends on the wave vector $\underline{k}$ of the corresponding state. For example the probability density for the electrons ocupying states at the neck has a node at the lattice sites and a maximum in the interstitial regions /2.8/. These states are therefore said to be p-like by analogy with atomic orbitals /5.1/. On the other hand the electrons at the belly regions of the Fermi surface have a maximum probability density at the lattice sites and are therefore predominantly s-like. As a consequence a substitutional defect with a well localized scattering potential should scatter the belly electrons more strongly than the neck electrons. On the other hand a defect localized on an interstitial site should scatter the neck electrons more strongly. The degree of localization of the scattering potential depends on the valence of the defect and on the local volume change $(\frac{\Delta V}{V})_{loc}$ produced by the defect. Defects with a small valence difference ΔZ and small $(\frac{\Delta V}{V})_{loc}$ are well localized and have strong scattering anisotropy. This is illustrated qualitatively by some alloys for which the scattering rates have been determined from dHvA measurements. Figure 5.2 shows contour plots of the scattering rates over the basic $1/48^{th}$ of the Fermi surface for four substitutional defects in copper and gold. For comparison the following table shows values for the change in lattice parameter $\Delta a/a$ which is proportional to the local volume change, and for the residual resistivity of these defects. The relative strength of the scattering produced by the defect is indicated by the resistivity ρ. The ratio of the neck and belly (110) Dingle temperatures indicates the scattering anisotropy.

	site	ΔZ	$\frac{\Delta a}{a}$	ρ ($\mu\Omega$cm/at%)	$\frac{Xneck}{XB(100)}$
Cu-Au	subst.	0	0.15	0.55	0.60
Cu-Ni	subst.	-1	-0.028	1.14	0.56
Cu-H	interst.	+1	(Pd-H 0.057)	1.50	3.0
Au-Ag	subst.	0	-0.005	0.36	0.29
Au-Zn	subst.	+1	-0.045	0.95	0.69

$\frac{\Delta a}{a}$ /5.5/ and for Pd-H /5.17/ (for one atomic fraction)
ρ /5.4/, CuH this work
X /5.6, 5.7/

Defects with larger valence difference have stronger over all scattering and defects with small $\frac{\Delta a}{a}$ (eg Au-Ag) have stronger scattering anisotropy. In each case the scattering for the substitutional defects is stronger in the belly region and weaker at the neck. For hydrogen in copper the scattering is stronger at the neck. This difference is due to the different location of the defect in the lattice.

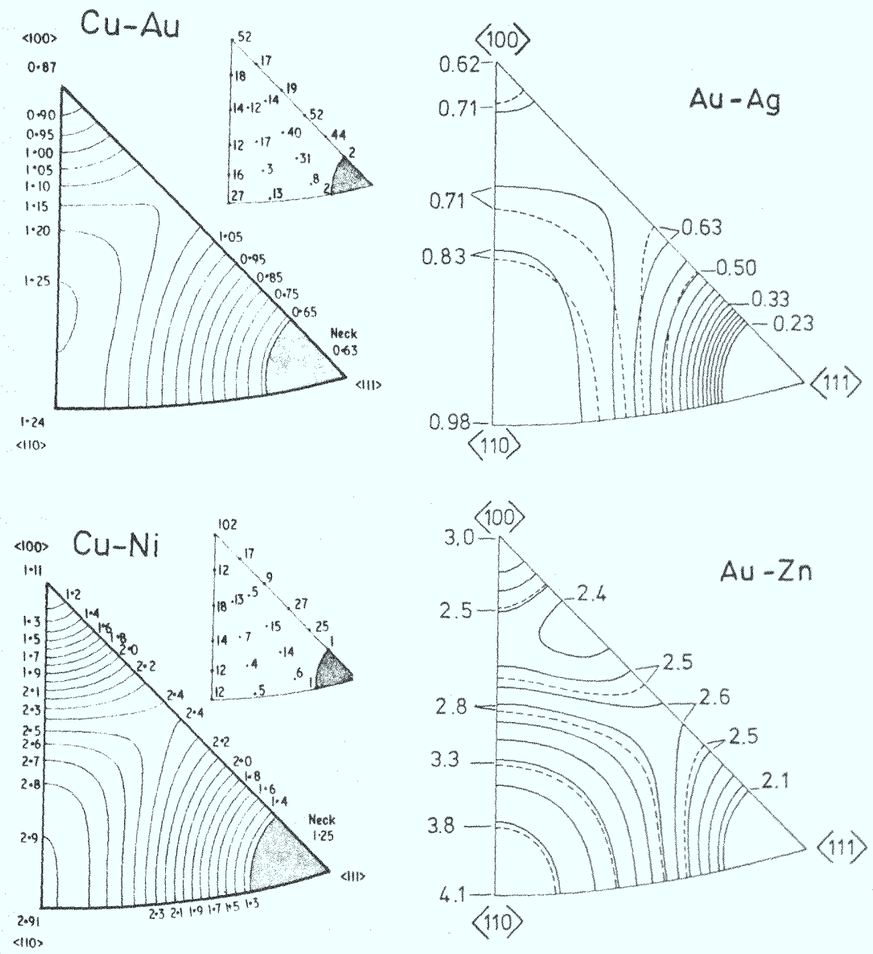

Fig. 5.2 Contour plots of scattering rates in four noble metal-substitutional impurity systems shown as a stereographic projection of the basic 1/48th of the Fermi surface. The units are $(10^{13} s^{-1} (at.\%)^{-1})$. The uncertainty in the fit is shown for the copper alloys in the small pictures in percent, and for the gold alloys this is represented by the difference in the solid and dotted lines /5.6, 5.7/.

5.3 Comparison between theory and experiment

5.3.1 Phase shift analysis of the scattering

For a spherically symmetric scattering potential in free space the wave function for an electron can be expressed as

$$\psi_E(\underline{k},\underline{r}) = \sum_{\ell m} c_{\ell m}(\underline{k},E) R_{E\ell}(r) Y_{\ell m}(\hat{\underline{r}})$$

$Y_{\ell m}(\hat{\underline{r}})$ are spherical harmonics and $R_{E\ell}$ is the radial wave function. In the asymptotic limit (V(r) = 0) the radial wave function can be written as

$$R_{E\ell}(r) = j_\ell(\kappa r) + t_\ell i h_\ell^+(\kappa r) \qquad (5.1)$$

where $\kappa = \sqrt{\frac{2m_o E}{\hbar}}$

$t_\ell \equiv \sin \eta_\ell \, e^{i\eta_\ell}$ (diagonal elements of the transition matrix).

j_ℓ and h_ℓ^+ are spherical Bessel and Hankel functions and η_ℓ are the phase shift between the incident plane wave j_ℓ and the scattered spherical wave h_ℓ^+.

In an ideal crystal the potential can be represented in the muffin-tin approximation by an array of non-overlaping spherically symmetric potentials at the lattice sites with V(r) = 0 outside the muffin-tin sphere. In a crystal all the scattered waves emerging from the different lattice sites must superpose to reproduce the incident wave. Using a Green's function procedure to obtain a solution to the wave equation in a muffin-tin lattice Korringa /5.18/ and Kohn and Rostoker /5.19/ (KKR) have shown that this superposition requires that

$$\det\left| A_{\ell m \ell' m'}(\kappa,\underline{k}) + \kappa \cot \eta_\ell \, \delta_{\ell\ell'}\delta_{mm'} \right| = 0 \qquad (5.2)$$

The $A_{\ell m \ell' m'}$ are structure factors which depend on the electron energy (κ) and $\underline{k}$ and on the lattice structure but not on the scattering potential. The atomic potential appears only through

the phase shifts η_ℓ. The band structure $E(\underline{k})$ is therefore determined by a set of energy dependent phase shifts $\eta_\ell(E)$ and the energy E through equation 5.2. From the experimentally determined Fermi surface, values for $\eta_\ell(E_f)$ and E_f can be found. Using three phase shifts (ℓ = 0,1,2) the Fermi surface cross sectional areas for copper have been fitted to an accuracy of $1:10^4$ /2.7/.

Colerdige, Holtzwarth and Lee /5.12, 5.13, 5.14/ have developed a modle to describe impurity scattering in dilute alloys based on the KKR theory in which the correct band structure for the host lattice (host phase shifts η_ℓ^h fitted to the Fermi surface) is included. They have obtained an expression for the scattering rates in terms of effective phase shifts ϕ_L of the defect /5.12, 5.14/ for each angular momentum ℓ and the different representations Γ of the cubic group belonging to the different ℓ.

$$\frac{1}{\tau(\underline{k})} = \frac{2c_i}{\hbar} \sum_{L \equiv \ell,\Gamma} d_L(\underline{k}) \sin^2\phi_L \qquad (5.3)$$

The weight factor d_L depends only on host lattice properties and is calculated from the band structure. The ϕ_L are called Friedel phase shifts. This phase shift has two contributions. First the phase shift between the wave incident on the defect and the scattered wave caused by the defect (η_ℓ^i for an interstitial defect, $\Delta\eta_\ell = \eta_\ell^i - \eta_\ell^h$ for a substitutional defect). The second contribution is a phase shift, produced by the defect in the incident wave due to backscattering from the surrounding lattice. The scattering wave emerging from a defect contributes differently through backscattering to the incident wave than the scattered wave emerging from a host atom. This effect produces a change in amplitude and in phase in the wave incident on the defect. This phase shift is the second contribution to ϕ_L. Since the screening charge around the defect depends on the total phase shift produced by the defect it is the Friedel phase shift ϕ_L which enters the Friedel sum /5.14/

$$\mathcal{F} = \sum_{L=\ell,\Gamma} 2g_L \frac{\phi_L}{\pi} \qquad (5.4)$$

g_L is the degeneracy of the representation Γ. An expression for the dHvA Dingle temperatures in terms of the Friedel phase shifts can be found from eq. 5.3 and eq. 2.33

$$m_c X = \frac{\hbar c_i}{2\pi^2 k_B} \sum_{L=\ell\Gamma} \langle d_L(\underline{k}) \rangle \sin^2 \phi_L \qquad (5.5)$$

The orbital weight factors $\langle d_L(\underline{k}) \rangle$ are an orbital average of the local weight factor $d_L(\underline{k})$ in eq. 5.3. These have been calculated for several orbits in the noble metals for substitutional defects /5.13/ and for interstitial defects in copper /5.12/ from the KKR band structure. From eq. (5.5) the Friedel phase shifts ϕ_L can be found from the measured Dingle temperatures. Using the data for Cu-H presented in chapter 4 and the $\langle d_L \rangle$ from Holtzwarth and Lee /5.12/ the ϕ_L for hydrogen in copper were found from a least squares fit. The results of the fit are presented in table 5.2. Since the ϕ_L enter the fit quadratically, the sign ($\pm$) cannot be determined from the fit. The possible combinations of the ϕ_L give Friedel sums of $\pm(0.88\pm0.06)$ and $\pm(0.42\pm0.09)$. Since the Friedel sum is equal to the charge of the defect to be screened the value $\mathcal{F} = 0.88\pm.06$ is closest to the valence $\Delta Z = +1$ of the defect. Therefore the correct sign of the phase shifts is both positive. The fit therefore shows that the hydrogen produces strong s wave scattering with the p scattering an order of magnitude weaker and the d scattering negligible. This is consistent with the short range of the potential as calculated by Friedel /5.15/ using the Thomas-Fermi approximation, the Born approximation and for the free electron modle (screening length $\simeq$ 1 Bohr radius).

Friedel's sum differs from +1 indicating that the local volume change produced by the hydrogen contributes to the effective charge to be screened. The charge ΔZ_{eff} to be screened by the conduction electrons consists of two contributions

$$\Delta Z_{eff} = \Delta Z - \left(\frac{\Delta V}{V}\right)_{loc} \qquad (5.6)$$

Table 5.1 Shown are the results of a phase shift fit to the Dingle temperatures in Cu-H based on the analysis of Holtzwarth and Lee. The fit used the 6 orbits (for B in the (110) plane) for which the orbital host parameters $\langle d_L \rangle$ have been evaluated, and included s, p, and d phase shifts. The error parameter Q is discussed in the appendix.

orbit	$X_{(meas)}$	$X_{(fit)}$
N(111)	112.6 ± 5.5	120.7
B(111)	65.0 ± 3.7	61.2
B(100)	37.9 ± 3.0	40.3
R(100)	89.8 ± 8.4	78.5
D(110)	77.3 ± 6.7	68.7
BTP	48.4 ± 3.3	48.4

L	ϕ_L
s	1.032 ± 0.035
p	0.115 ± 0.037
d_{12}	0
d_{25}	0

$$Q = \sum \left(\frac{X_{(fit)} - X_{(meas)}}{\sigma_X} \right)^2$$

$$= 7.3$$

ΔZ is for substitutional impurities the chemical valence difference between the impurity and an host atom and for an interstitial impurity it is the valence of the impurity (+1 for H in Cu). The second contribution, first introduced into the Friedel sum by Blatt /5.3/ takes into account the volume change of the lattice in the vicinity of the defect. For simplicity the crystal is considered as an isotropic continuum. According to Eshelby /5.2/ a defect in an infinite crystal producing a local volume change $(\frac{\Delta V}{V})_{loc}$ changes the volume of the whole crystal by $(\frac{\Delta V}{V})_{loc}$ as well, i.e. the crystal is only sheared and not compressed. This is no longer true in a finite crystal. In fact, the material surrounding a finite volume in an infinite crystal acts as an extermal pressure. If the material is removed the free surface can relax so that a defect producing a volume change $\Delta V_{loc} = \Delta V_{\infty}$ in an infinite crystal produces instead a volume change $\Delta V > \Delta V_{loc}$ in a finite crystal. The ratio $\frac{\Delta V}{\Delta V_{loc}}$ can be expressed in terms of Poisson's number ν

$$\frac{\Delta V}{\Delta V_{loc}} = \frac{3(1-\nu)}{1+\nu} = 1.44 \text{ for Cu} \quad /5.3/$$

The volume change ΔV in the finite crystal can be measured by the lattice parameter change $\frac{\Delta a}{a}$ due to the defect.

$$\frac{\Delta V}{V} = 3\frac{\Delta a}{a}$$

Therefore $(\frac{\Delta V}{V})_{loc} = \frac{1}{3}\,\frac{1+\nu}{1-\nu} \cdot 3\frac{\Delta a}{a}$.

The lattice parameter change $\frac{\Delta a}{a}$ has not yet been measured in the system CuH. To get the right order of magnitude the value for PdH can be taken. $\Delta a/a$ was found for this system to be $\Delta a/a = 5.7\ 10^{-4}$/at.% /5.17/. This gives $(\frac{\Delta V}{V})_{loc} = 0.25$ and a Friedel sum of 0.75 which somewhat smaller than the experimental value of 0.88±.06 for hydrogen in copper. The discrepancy is not too significant since the assumption of an isotropic medium is not very good for copper. Also a local volume change is inconsistent with the KKR method of scattering calculations which assumes a periodic lattice outside the defect muffin-tin.

From equation 5.2 the local lifetimes can be obtained from the Friedel phase shifts if the structure factors $d_L(\underline{k})$ are known. Although these have been calculated by Holtzwarth and Lee /5.12/ when calculating the orbital weight factors $\langle d_L \rangle$, the local $d_L(\underline{k})$ have not been published in a form which allows calculation of local lifetimes. It would be very desirable to calculate other quantities from the fitted phase shifts, which have also been determined experimentally, for instance the residual resistivity ρ_H due to hydrogen in Cu or the low field Hall coefficient. This would provide a check of the consistency of the phase shift analysis. For this purpose the mean free path $\Lambda(\underline{k})$ has to be calculated /5.13/

$$\frac{1}{\Lambda(\underline{k})} = \frac{a^3 c_H}{16\pi^2 \hbar v(\underline{k})} \int_{FS} |T_{\underline{k}\underline{k}'}|^2 (1-\cos\theta_{\underline{v}\underline{v}'}) \frac{dS_{\underline{k}'}}{\hbar v(\underline{k}')} \qquad (5.7)$$

$\theta_{\underline{v}\underline{v}'}$ is the angle between $\underline{v}(\underline{k})$ and $\underline{v}(\underline{k}')$. The T matrix $T_{\underline{k}\underline{k}'}$ and $|T_{\underline{k}\underline{k}'}|^2 \cos\theta_{\underline{v}\underline{v}'}$, can be expressed in terms of the phase shifts ϕ_L and by using the band structure of Cu. Once $\Lambda(\underline{k})$ has been calculated the residual resistivity ρ_H and the low field Hall coefficient R_H^o are evaluated according to

$$\frac{1}{\rho_H} = \frac{e^2}{12\pi^2\hbar} \int_{FS} \Lambda(\underline{k})\, dS_k \qquad (5.8)$$

$$R_H^o = \frac{12\pi^3}{e} \left(\int_{FS} dS_k \Lambda^2(\underline{k}) \kappa_m \right) \left(\int_{FS} \Lambda(\underline{k})\, dS_k \right)^{-2} \qquad (5.9)$$

κ_m is the mean local curvature of the Fermi surface at $\underline{k}$. The experimental values of ρ_H and R_H^o are (1.50±0.05) μΩcm/at.% and $-8.0\ 10^{-5}$ $cm^3/(Coulomb)$.

5.3.2 Calculation of the local scattering rates in Cu-H by Huisman and Weiss

Local scattering rates for hydrogen in copper have been calculated by Huisman and Weiss /5.8/. The technique used for calculating the scattering involves an extension to NaCl type lattices of the KKR method employed by Bansil et al. for α Cu-Zn /5.11/. In the model the hydrogen atoms were located at the octahedral interstitial sites in the copper lattice forming an fcc sublattice which was treated as a binary alloy of hydrogen and hydrogen vacancies (Cu muffin-tin zero potential). In the stochiometric limit Cu_1H_1 this is an NaCl type lattice. The main difference between this model and the phase shift analysis of Holtzwarth, Coleridge and Lee lies in the representation of the atomic potentials. In the phase shift formulation, the potentials of the host lattice and defect are represented by scattering phase shifts which are fitted to the experimentally determined Fermi surface and defect scattering rates. In the model of Huisman and Weiss the potential at the occupied octahedral sites was taken to be that of a neutral hydrogen atom, and the potential used for the copper was a renormalized atom potential /5.10/ (ℓ dependent potential). This approach is similar to that used by Segall /2.8/ for the band structure of Cu.

The results of the calculation are given in table 5.2 and shown in figure 5.3 (solid line) as the scattering rate $\frac{1}{\tau(\underline{k})}$ for $\underline{k}$ in the (100) plane from ⟨110⟩ to ⟨100⟩ and then in the (110) plane from ⟨100⟩ through ⟨111⟩ to ⟨110⟩ (i.e. the perimeter of the basic 1/48th of the Fermi surface). The scattering rates calculated by Huisman and Weiss do not contain electron-phonon enhancement effect. Therefore before comparison between experimental and calculated scattering rates can be made the calculated scattering rates must be divided by the local electron-phonon enhancement factor $(1+\lambda(\underline{k}))$ (figure 2.9). The results of Huisman and Weiss modified in this way (electron-phonon renormalized) can then be compared directly with the values deduced from the measured Dingle temperatures (figure 5.3). In view of the fact that the theory contains no fitted parameters it must be concluded that the agreement between theory and experiment

Table 5.2

Band Structure Calculation for Scattering from Interstitial Hydrogen in Copper

Orbit	Calculated* X ^{o}K/at.%	el-ph correction+	Calculated (el-ph corrected) X ^{o}K/at.%	Measured X ^{o}K/at.%
B(100)	45 ± 5	1.107	40.7	37.9 ± 3
D(110)	85 ± 5	1.146	74.2	77.3 ± 6.7
N(111)	140 ± 5	1.230	113.8	112.6 ± 5.5
	$\frac{1}{\tau}$ $10^{13}s^{-1}at\%^{-1}$		$\frac{1}{\tau}$ $10^{13}s^{-1}at\%^{-1}$	$\frac{1}{\tau}$ $10^{13}s^{-1}at\%^{-1}$
$\underline{k}$(100)	2.31	1.211	1.91	2.8 ± 0.8
$\underline{k}$(110)	5.16	1.038	4.97	4.4 ± 0.4
Neck	11.6	1.219	9.49	9.3 ± 0.36

+Lee /2.14/

* Huisman and Weiss /5.8/

is very good, the discrepancies being for the most part within the experimental error limits. The excellent agreement indicates that the assumption that the hydrogen occupies the octahedral site is probably correct and that the neutral atom potential used for the hydrogen is a good approximation. As a further check on the consistency of the model further comparisons with experiment should be made, for example using transport coefficients.

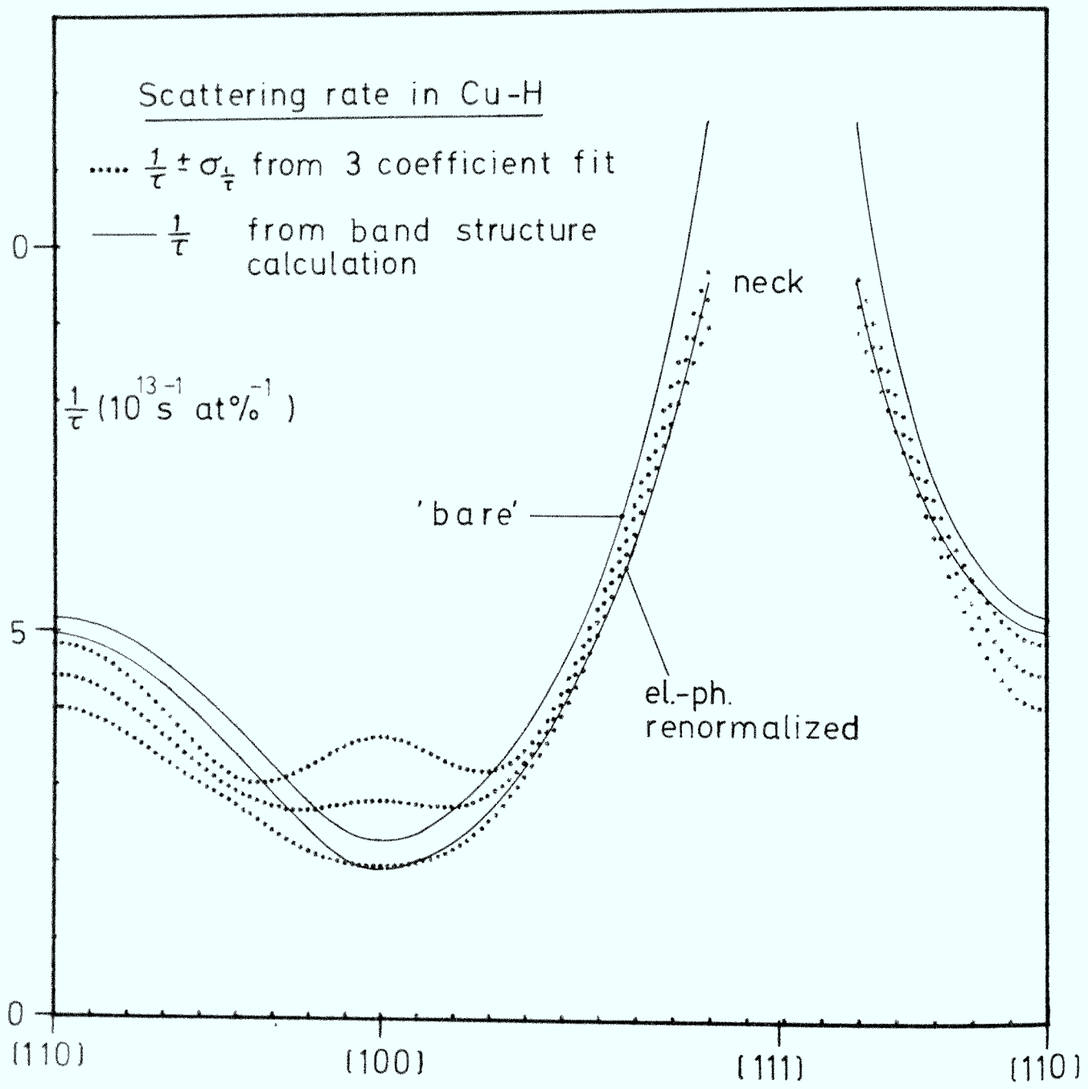

Fig. 5.3 Values on the perimeter of the basic 1/48th zone of the Fermi surface for the experimentally determined scattering rate in Cu-H with error band (dotted lines) are plotted together with the scattering rates for Cu-H calculated by Huisman and Weiss /5.8/ (solid line). Since the scattering rates calculated by Huisman and Weiss did not include the electron-phonon interaction the calculated values have been corrected to include this effect /2.14/ so that they can be directly compared with the experimental values.

Table 5.2

Band Structure Calculation for Scattering from Interstitial Hydrogen in Copper

Orbit	Calculated* X ^{o}K/at.%	el-ph correction+	Calculated (el-ph corrected) X ^{o}K/at.%	Measured X ^{o}K/at.%
B(100)	45 ± 5	1.107	40.7	37.9 ± 3
D(110)	85 ± 5	1.146	74.2	77.3 ± 6.7
N(111)	140 ± 5	1.230	113.8	112.6 ± 5.5
	$\frac{1}{\tau}\ 10^{13} s^{-1} at\%^{-1}$		$\frac{1}{\tau}\ 10^{13} s^{-1} at\%^{-1}$	$\frac{1}{\tau}\ 10^{13} s^{-1} at\%^{-1}$
$\underline{k}$(100)	2.31	1.211	1.91	2.8 ± 0.8
$\underline{k}$(110)	5.16	1.038	4.97	4.4 ± 0.4
Neck	11.6	1.219	9.49	9.3 ± 0.36

+Lee /2.14/

* Huisman and Weiss /5.8/

is very good, the discrepancies being for the most part within the experimental error limits. The excellent agreement indicates that the assumption that the hydrogen occupies the octahedral site is probably correct and that the neutral atom potential used for the hydrogen is a good approximation. As a further check on the consistency of the model further comparisons with experiment should be made, for example using transport coefficients.

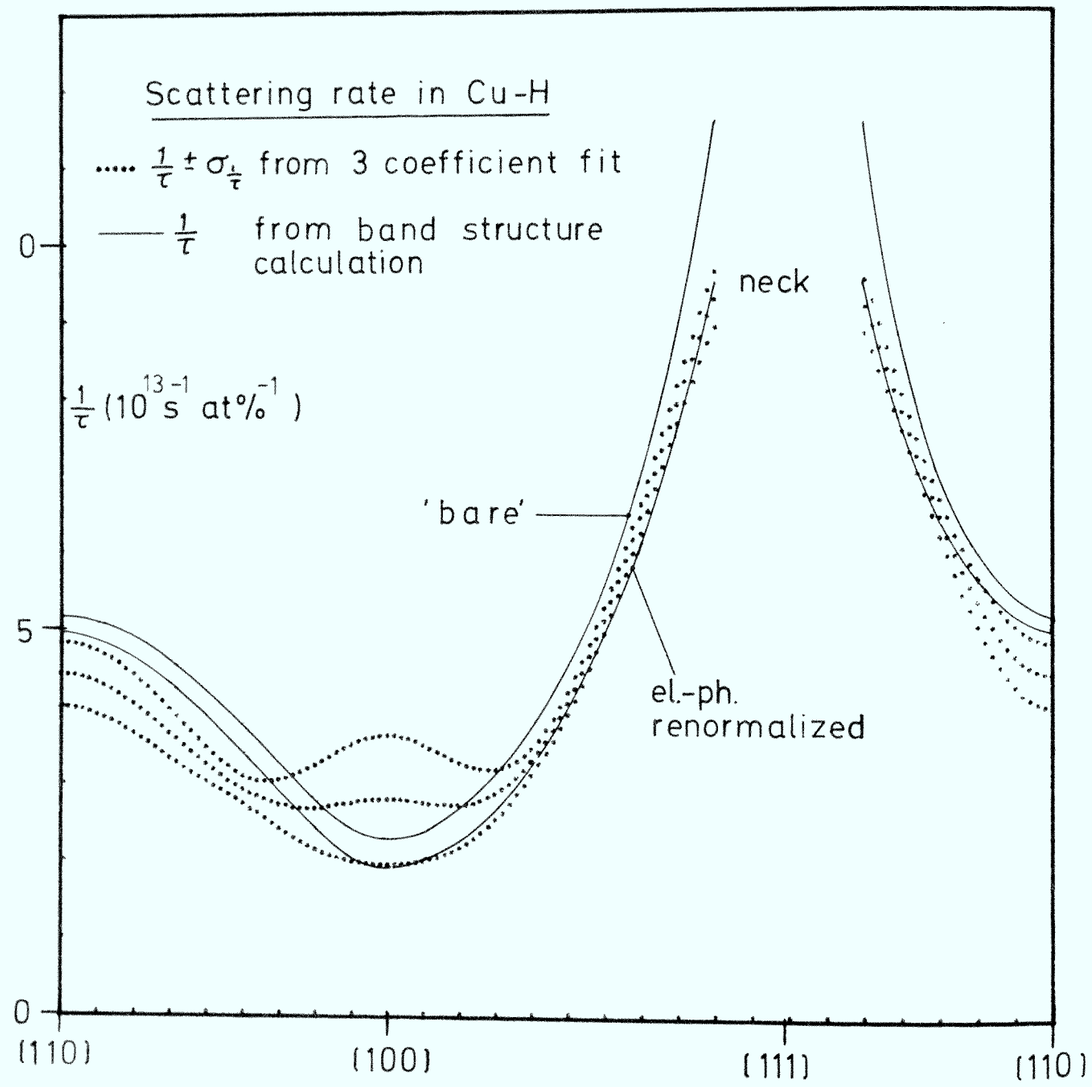

Fig. 5.3 Values on the perimeter of the basic 1/48th zone of the Fermi surface for the experimentally determined scattering rate in Cu-H with error band (dotted lines) are plotted together with the scattering rates for Cu-H calculated by Huisman and Weiss /5.8/ (solid line). Since the scattering rates calculated by Huisman and Weiss did not include the electron-phonon interaction the calculated values have been corrected to include this effect /2.14/ so that they can be directly compared with the experimental values.

Conclusions

The interaction between the conduction electrons in copper and lattice defects can be described by a scattering rate which varies over the Fermi surface. The anisotropy of the scattering rate depends on the type of defect. The dHvA effect provides a way to determine experimentally the local scattering rates. This technique has recently been used to investigate the scattering rates for substitutional defects in noble metal hosts. In this work we have extended the knowledge about scattering rates to include interstitial hydrogen in copper. Dingle temperatures were measured in 11 samples covering a hydrogen concentration range from 0 to 143 ppm. For each sample 11 orbits were measured to obtain good coverage of the Fermi surface. Special attention to the metallurgical behavior of hydrogen in copper was necessary when preparing the samples to insure that the hydrogen was uniformly distributed within the samples.

Values for the local scattering rates $1/\tau(\underline{k})$ were obtained from the measured Dingle temperatures by using a symmetrized Fourier series to represent the local scattering rates. The scattering rate was found to be strongly anisotropic with a maximum of 9.3×10^{13} $s^{-1}(at.\%)^{-1}$ at the neck and a minimum of 2.7×10^{13} s^{-1} $(at.\%)^{-1}$ at <100>. On the other hand it has previously been found that for a well localized substitutional defect the scattering rate is smallest at the neck. The anisotropy arises from the fact that the probability density of the electrons occupying states at the neck has a node at the lattice site. These electrons are therefore strongly scattered by an interstitial defect but only weakly scattered by a defect localized at the substitutional site.

Analysis of the measured Dingle temperatures in terms of scattering phase shifts based on muffin-tin potentials and a KKR, band structure calculation shows that the s-component of the incident wave is most strongly scattered, the p scattering is an order of magnitude less and the d scattering is negligible. This is consistent with a scattering potential well localized at the octahedral interstitial site.

Huisman and Weiss have recently calculated the local scattering rates for Cu-H based on a KKR band structure calculation. The hydrogen potential was assumed to be that of a neutral hydrogen atom located at the octahedral interstitial site. The scattering rates from this experiment were found to be in excellent agreement with those calculated by Huisman and Weiss. Bearing in mind that the calculation contains no free parameters this is a remarkable result. It shows that at least for hydrogen in copper, the scattering is described fairly well by the model of Huisman and Weiss. Using this model one should try to calculate other quantities such as the transport coefficients and the heat of solution and by further comparison with experiment provide a check of the consistency of the model.

Appendix

Calculation of local scattering rates from the measured Dingle temperatures

In section 2.5.3 it was shown how the local scattering rates can be obtained from the measured Dingle temperatures using a symmetrized Fourier series to represent the local scattering rates.

$$\frac{1}{\tau(\underline{k})} = \sum_j T_j \Phi_j(\underline{k}) \qquad (2.34)$$

$$\Phi_j(\underline{k}) = \cos(\tfrac{a}{2}\ell k_x)\cos(\tfrac{a}{2}m k_y)\cos(\tfrac{a}{2}n k_z)$$

where a is the lattice parameter, $\underline{k}$ is the Fermi wave vector and $j = (\ell,m,n)$ are ordered according to increasing $\ell^2+m^2+n^2$ and $\ell+m+n$ is even for the fcc lattice. In this section the results of the fit to the measured data given in chapter 4 are presented. The propegation of the experimental errors in the Dingle temperature data into error limits on the scattering rates will be discussed and the effect of increasing the number of coefficients used in the fit is considered.

The Dingle temperatures are determined by the coefficients T_j and a set of orbital parameters H_{ij}

$$X = \sum_j H_{ij} T_j \qquad (2.36)$$

where $H_{ij} = \left(\frac{\hbar^2}{4\pi^2 k_B m c_i}\right) \oint_i \frac{k_\perp^2}{(\underline{v}\cdot\underline{k}_\perp)} \Phi_j(\underline{k})\, d\varphi$

The coefficients are found by minimizing

$$Q = \sum_i \left(\frac{X_i^f - X_i^m}{\sigma_{X_i}}\right)^2 \qquad (2.37)$$

where X_i^m, σ_{X_i} are the measured Dingle temperatures and the corresponding standard error, and X_i^f are the values calculated from 2.34.

The minimizing condition $\frac{\partial Q}{\partial T_j} = 0$ can be expressed in matrix notation as:

$$(H^T W H)\underline{T} = H^T W \underline{X}$$

with the solution

$$\underline{T} = V H^T W \underline{X} \qquad \text{(A1)}$$

for the coefficients T_j where $\underline{X}$ is the data vector of the measured X_i^m, W is a diagonal matrix with elements $W_{ij} = \left(\frac{1}{\sigma_{X_i}}\right)^2 \delta_{ij}$.

The matrix $V \equiv (H^T W H)^{-1}$ describes how the experimental errors in X_i propagate into the coefficients T_j. The diagonal element $V_{jj} = \sigma^2_{T_j}$ are the variance of the coefficients T_j. If det V becomes very large there is a strong correlation between the coefficients T_j implying that a fit with one less coefficient will give a similar Q value. The calculation of the coefficients T_j thus consists of

a) Calculating the orbital parameters H_{ij} (eq. 2.35) for which $\underline{k}$ and $\underline{v}(\underline{k})$ must be known. (See sections 2.3, 2.4 and 2.5) Values for H_{ij} for copper for the 11 orbits measured are listed in table A1.
b) Finding V by inverting $(H^T W H)$
c) T_j are then given by eq. A1

The experimental errors σ_{X_i} in the measured X_i values give rise to an uncertainty in the fitted values for $\frac{1}{\tau}$. That is, there is a range in the choice of the coefficients T_j and hence in $\frac{1}{\tau}$ which will lead to variations in the fitted X_i values within the uncertainty σ_{X_i}. The uncertainty $\sigma_{\frac{1}{\tau}}$ in the fitted $\frac{1}{\tau}$ values depends on the uncertainty σ_{X_i} in the measured X_i through the matrix V.

$$\sigma^2_{\frac{1}{\tau}}(\underline{k}) = \sum_{\ell,m} \Phi_\ell(\underline{k}) V_{\ell m} \Phi_m(\underline{k}) \qquad \text{(A2)}$$

This quantity describes the uniqueness of the fit and depends on the σ_{X_i} but not on the values of X_i themselves. The meaning of σ_{X_i} and $\sigma_{\frac{1}{\tau}}$ is that if the same experiment and fit were repeated many times the mean of the results $\bar{X}_i$ and $(\frac{1}{\tau(\underline{k})})$ has a 63 % probability of being within σ_{X_i} and $\sigma_{\frac{1}{\tau}}$ of the original data sets X_i and $\frac{1}{\tau(\underline{k})}$ respectively.

If $\sigma_{\frac{1}{\tau}}$ is small this does not however mean that the fit is good in the sense that Q is small since this also depends on the suitability of the representation for $\frac{1}{\tau}$. If the fitted X_i^f values are within σ_{X_i} of the measured X_i^m values, i.e. $Q \lesssim n$ (n = number of X values) then the representation is good one.

The physical significance of the fitted $\frac{1}{\tau}$ values therefore depends on two conditions
a) that the representation for $\frac{1}{\tau}$ is a good one i.e. Q is small
b) that the uncertainty in the fit $\sigma_{\frac{1}{\tau}}$ is small.

In fitting the X data for Cu-H it was found that one or two coefficients were not enough to provide an adequate representation. A three coefficient fit however gave Q = 4.86, that is the calculated X_i agreed fairly well with the measured values (see table A2). The coefficients for the 3 coefficient fit and the error propagation matrix V are given in table A3. The values for $\frac{1}{\tau}$ from the 3 coefficient fit and the uncertainty $\pm\sigma_{\frac{1}{\tau}}$ are shown in figures A1 and 5.3. Figure A1 is a stereographic projection of lines of equal scattering rates in 1/48th of the Fermi surface. Figure 5.3 shows the scattering rate $1/\tau(k)$ for $\underline{k}$ values on the border of the basic 1/48th unit of the Fermi surface. Increasing the number of coefficients from 3 to 5 brought only a slight decrease in Q from 4.86 to 4.60 indicating that the representation for $\frac{1}{\tau}$ was not being significantly improved. However, as the number of coefficients was increased beyond 4 the correlation between the coefficients strongly increased and the uncertainty in $\frac{1}{\tau}$ became larger. For fits with 3 to 5 coefficients it was found that the error band of each fit lay entirely within those of fits with more coefficients. These considerations led to the choice of the three coefficient fit as being the

the best fit to the data since, of the fits which were adequate representations of the X data (number of coefficients $\geq$ 3) it had the smallest uncertainty in $\frac{1}{\tau}$.

Table A1

Orbital parameter matrix H_{ij} for Cu

	000	110	200	211	220	310
B(100)	12.15669	-4.885175	7.862645	-5.819140	0.471052	9.031713
BTP	12.15669	-3.983405	0.820984	-3.987344	0.176890	11.136142
B(111)	12.15669	-1.950178	-14.828333	1.020337	-1.841478	6.638539
N(111)	12.15669	-1.256854	-31.442110	1.255793	26.938166	6.503584
D(110)	12.15669	-3.228591	- 9.145812	-2.519729	10.293341	8.276575
R(100)	12.15669	-1.581216	-21.081929	1.581216	6.533092	5.223802
B65	12.15669	-2.064950	-15.128524	0.560500	1.358548	7.297480
N65	12.15669	-1.267166	-31.142330	1.257798	26.380408	6.510934
D85	12.15669	-3.203024	- 9.367206	-2.463454	10.330471	8.263112
N75	12.15669	-1.315699	-29.718018	1.271890	23.711076	6.515368
B9	12.15669	-4.558050	5.425198	-5.162745	0.0695091	10.039171

$$H_{ij} = \left(\frac{\hbar^2}{4\pi^2 k_B m_{c_i}} \right) \oint_i \left(\frac{k_\perp^2}{(\underline{v} \cdot \underline{k}_\perp)} \right) \Phi_j(\underline{k}) \, d\varphi \qquad \text{units } 10^{13}\ {}^{o}\mathrm{Ks}^{-1}(\text{at.}\%)^{-1}$$

The H_{ij} were calculated using the symmetrized Fourier series representations for the Fermi surface and Fermi velocity discussed in sections 2.2 and 2.3 and the coefficients listed in table 2.1 (Halse Cu5 Fermi surface /2.4/).

Table A.2 Values of Dingle temperatures from various fits X_i^r (^oK/at.%)

orbit	X_i^m (^oK/at%)	σ_{X_i}	2 coeff	3 coeff	3 coeff (6 non-tipped orbits only)	4 coeff	5 coeff
B(100)	37.9	3.0	37.8	40.3	38.9	39.8	38.9
B9	45.6	3.3	42.6	42.9	-	43.0	42.7
BTP	48.4	3.3	51.1	48.5	47.6	49.3	49.2
B(111)	65.0	3.7	81.1	66.2	66.6	66.0	66.2
B65	65.7	8.6	79.4	69.4	-	69.4	69.1
N(111)	112.6	5.5	91.4	112.8	115.3	112.8	112.4
N65	102.3	10.0	91.2	111.9	-	112.0	111.7
N75	110.0	13.2	90.5	107.7	-	107.7	107.9
D(110)	77.3	6.7	62.3	70.0	70.3	70.0	72.2
D85	71.0	13.3	62.6	70.4	-	70.3	72.4
R(100)	89.8	8.4	86.6	81.7	82.8	81.0	79.6
Q			47.09	4.860	2.44	4.776	4.596
det V			1.7×10^{-2}	5.3×10^{-3}	1.19×10^{-2}	1.16	1.2×10^{3}

Table A3

T_j are the Fourier coefficients for the scattering rates from the 3 and 4 coefficient fit to the measured Dingle temperatures. V is the error propegation matrix for the 3 coefficient fit (see text).

	Coefficients T_j for $\frac{1}{\tau}$ ($10^{13} s^{-1} at.\%^{-1}$)		V_{ij} for 3 coefficient fit		
j	3 coeff	4 coeff			
(000)	- 2.004	1.232	3.005	9.191	0.942
(110)	- 19.041	- 4.924	9.191	28.256	2.883
(200)	- 3.601	- 3.088	0.942	2.883	0.307
(211)		- 4.319			

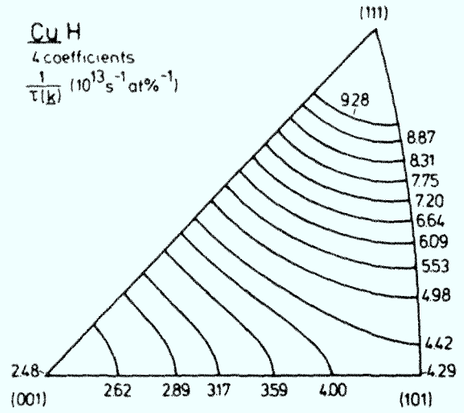

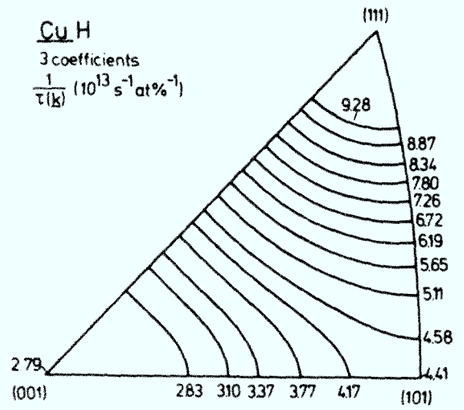

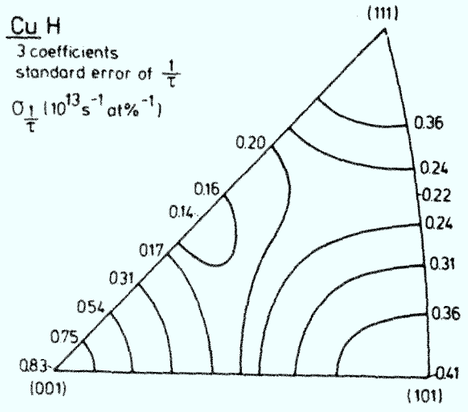

Fig. A1 Contour plots of the local scattering rate $1/\tau(\underline{k})$ for Cu-H over the basic 1/48th of the Fermi surface in stereographic projection. Shown are the scattering rates from the three and four coefficient fits as discussed in the text and the standard error in $1/\tau(\underline{k})$ for the three coefficient fit.

Index to symbols used in text

Symbol	Definition
$\hbar$	Planks constant
e	electronic charge
m_o	electron mass
μ_o	permeability of free space (SI units)
$\phi_o = \frac{2\pi h}{e}$	fundamental flux quantum
k_B	Boltzmans constant
$\mu_B = \frac{he}{2m_o}$	Bohr magneton
$\underline{r}$	position vector
$\underline{k}$	wave vector or Fermi wave vector
$\underline{v}$	velocity or Fermi velocity
T	temperature
$\underline{B} = \mu_o(\underline{H}+\underline{M})$	Magnetic field
$\underline{H}$	Magnetic field
$\underline{M}$	Magnetization
$\omega_c = \frac{eB}{m_c}$	cyclotron frequency
a	lattice parameter (for Cu a = 3.603 Å)
m_c	cyclotron mass (2.5)
$T_c = \frac{2\pi}{\omega_c}$	cyclotron period
ϕ	magnetic flux
$v_\perp, k_\perp$	components of v and k perpendicular to the magnetic field
$E(\underline{k})$	Energy of electron with wave vector $\underline{k}$
E_f	Fermi energy
S	area of cyclotron orbit in real space

A	area of cyclotron orbit in k space or cross sectional area of the Fermi surface perpendicular to the magnetic field
A_{ext}	extremal cross-sectional area
n	quantum number of a Landau cylinder or specifically the outermost cylinder intersecting the Fermi surfac
γ	phase factor $0 < \gamma < 1$
d	degeneracy of Landau levels (2.7)
F	dHvA frequency (2.8)
ξ	dHvA phase
$\alpha \equiv \frac{2\pi^2 m_o k_B}{he}$	
X	Dingle temperature (2.10)
X_i^m	measured Dingle temperatures
X_i^f	fitted Dingle temperatures
$\tau(\underline{k})$	lifetime of an electron in state $\underline{k}$
$\frac{1}{\tau(\underline{k})}$	scattering rate
$\langle \quad \rangle$	denotes average around an extremal orbit (2.32)
$\hat{M}$	oscillatory component of magnetization (2.11)
M_1	amplitude of 1^{st} harmonic component of $\hat{M}$ (2.12)
g	g factor
s	spin quantum number
$\rho(E)$	density of states
k_s, v_s, E_s, A_s, V_s, ρ_s	Subscript's' denotes value for free electron sphere (Fermi wave vector, Fermi velocity, Fermi energy, cross-sectional area, Fermi surface volume, density of states)
θ_D	Debye temperature
$E_o(\underline{k})$, $v_o(\underline{k})$, m_c^o	Subscript o denotes value in absence of electron phonon effect or 'band' value

$1+\lambda(\underline{k})$	electron phonon renormalization factor
$1+\Lambda$	orbital average of $1+\lambda(\underline{k})$ (2.21)
$T_{\underline{kk}'}$	transition matrix elements (2.23)
$P_{\underline{kk}'}$	transition probability from initial state $\underline{k}$ to final state $\underline{k}'$ (2.22)
$\Phi_j(\underline{k})$	cosine terms in symmetrized Fourier series (2.34)
T_j	scattering rate coefficients (2.34)
H_{ij}	orbital weight factors, 1^{st} orbit, j^{th} Fourier term (2.35) and table A1
$V_{\ell m}$	matrix describing error propegation from measured X's into fitted scattering rates $\frac{1}{\tau}$ and coefficients T_j
Q	error parameter for fit to Dingle temperatures (2.36)
σ_x	standard error of measured Dingle temperature (4.1)
$\sigma_{\frac{1}{\tau}}$	standard error in fitted scattering rate (A2)
b	amplitude of modulation field
$\omega = 2\pi f$	modulation frequency
δ	skin depth (§ 3.1.4)
ρ	residual resistivity
$\sigma = \frac{1}{\rho}$	conductivity
ρ_H	residual resistivity due to dissolved hydrogen
ρ_o	residual resistivity of sample containing no hydrogen
c_i	impurity concentration
c_H	hydrogen concentration
P	pressure
D	diffusion coefficient

ΔH_s	enthalpy of solution
E_m	migration energy
$\left(\frac{\Delta V}{V}\right)_{loc}$	local volume change in the vicinity of a defect
ℓ	angular momentum quantum number
η_ℓ	scattering phase shift between incident and scattered wave
Γ	denotes the representations of the cubic group belonging to the different ℓ
$L \equiv \ell, \Gamma$	
g_L	degeracy of the representation Γ
ϕ_L	Friedel phase shifts
$d_L(\underline{k})$	lifetime weight factor of the host lattice in the phase shift analysis
ΔZ	chemical valence difference of a defect
ΔZ_{eff}	effective charge of a defect (5.6)
ν	Poisson's ratio

References

/2.1/ I.M. Lifshitz and A.M. Kosevich
JETP 2, 636 (1956)

/2.2/ A.V. Gold
The Simon Fraser University, Lectures ed. J.F. Cochran
R.R. Haering, Gordon & Breach (1968)

/2.3/ P.T. Coleridge and I.M. Tempelton
J. of Phys. F, Metal Phys. 2, 643 (1972)

/2.4/ M.R. Halse
Phil. Trans. Roy. Soc. 265, 507 (1969)

/2.5/ M.J.G. Lee
Phys. Rev. 187, 901 (1969)

/2.6/ N.J. Coenen and A.R. de Vroomen
J. Phys. F. Metal Phys. 2, 487 (1972)

/2.7/ J.C. Shaw, J.B. Ketterson and L.R. Windmiller
Phys. Rev. B 5, 3894 (1972)

/2.8/ B. Segall
Phys. Rev. 125, 109 (1962)

/2.9/ G.A. Burdick
Phys. Rev. Lett. 7, 156 (1961)

/2.10/ J.S. Faulkner, H.L. Davis and H.W. Joy
Phys. Rev. 161, 656 (1967)

/2.11/ E.C. Snow
Phys. Rev. 171, 785 (1968)

/2.12/ Lengeler et al.
To be published

/2.13/ D.L. Martin
Phys. Rev. B 8, 5357 (1973)

/2.14/ M.J.G. Lee
Phys. Rev. B 2, 250 (1970)

/2.15/ J.W. Wilkins
"Observable many-body effects in metals" 1968 Nordita

/2.16/ L.I. Schiff
"Quantum Mechanics", McGraw Hill (1968)

/2.17/ A.D. Brailsford
Phys. Rev. 149, 456 (1966)

/2.18/ P. Soven
Phys. Rev. B 5, 260 (1972)

/2.19/ E.A. Stern
Phys. Rev. B 7, 1303 (1973)

/2.20/ E. Mann
Phys. Kondens. Materie, 12, 210 (1971)

/2.21/ I.M. Templeton and P.T. Coleridge
J. Phys. F: Metal Phys. 5, 1307 (1975)

/2.22/ P.T. Coleridge
J. Phys. F: Metal Phys. 5, 1317 (1975)

/2.23/ R.E. Doezema and F. Koch
Phys. Rev. B 6, 2071 (1972)

/2.24/ P. Haussler and S.J. Welles
Phys. Rev. 152,675 (1966)

/2.25/ S. Engelsberg and G. Simpson
Phys. Rev. B 2, 1657 (1970)

/2.26/ C.J. Palin
Proc. Roy. Soc. Lond. A 329, 17 (1972)

/3.1/ D. Shoenberg and P.J. Stiles
Proc. Roy. Soc. A281, 62 (1964)

/3.2/ R.W. Stark and L.R. Windmiller
Cryogenics 272 (1968)

/3.3/ M. Springford
Advances in Physics 20, 493 (1971)

/3.4/ D.A. Hill and C. Hwang
J. Sci. Inst. 43, 581 (1966)

/3.5/ D. Shoenberg
Phil. Trans. Roy. Soc. A 255, 85 (1962)

/3.6/ A. Fattah, V. Sorajic, W. Uelhoff
Berichte der KFA Jülich, JÜL-944-FF (1973) 8.5.4

/3.7/ K. Maier, C. Bassani and W. Schüle
Phys. Letters A 44, 539 (1973)

/3.8/ W. Schilling and K. Sonnenberg
J. Phys. F: Metal Phys. 3, 322 (1973)

/3.9/ B. Lengeler and R.R. Bourassa
to be published

/3.10/ E.O. Wollan, J.W. Cable and W.C. Koehler
J. Phys. Chrm. Solids 24, 1141 (1963)

/3.11/ J.E. Worsham, M.K. Wilkinson and C.G. Shull
J. Phys. Chem. Solids 3, 303 (1957)

/3.12/ W.R. Wampler, T. Schober and B. Lengeler
in press

/3.13/ C. Budin, A. Lucasson and P. Lucasson
Journale de Physique 25, 751 (1964)

/3.14/ R.B. McLellan
J. Phys. Chem. Solids 34, 1137 (1973)

/3.15/ C.L. Thomas
Trans. ALME 239, 485 (1967)

/3.16/ W. Eichenauer, W. Löser and H. Witte
Z. Metallkde. 56, 287 (1965)

/3.17/ W. Eichenauer and A. Pebler
Z. Metallkde. 48, 373 (1957)

/3.18/ W. Triftshäuser and T.D. McGervey
Appl. Phys. 6, 177 (1975)

/3.19/ R.O. Simmons and R.W. Balluffi
Phys. Rev. 129, 1533 (1963)

/3.20/ L. Katz, M. Guinan, and R.J. Borg
Phys. Rev. B 4, 330 (1971)

/5.1/ J.M. Ziman
Principles of the Theory of Solids, CUP (1972)

/5.2/ J.D. Eshelby
J. Appl. Phys. 25, 255 (1954)

/5.3/ F.J. Blatt
Phys. Rev. 108, 285 (1957)

/5.4/ F.J. Blatt
Physics of Electronic Conduction in Solids, McGraw Hill
(1968)

/5.5/ W.B. Pearson
"A Handbook of lattice spacings and structures of metals
and alloys", Academic Press (1958)

/5.6/ D.H. Lowndes, K.M. Miller, R.G. Poulson and M. Springford
Proc. R. Soc. London A 331 497 (1973)

/5.7/ R.G. Poulson, D.L. Randles and M. Springford
J. Phys. F: Metal Phys. 4, 981 (1974)

/5.8/ L. Huisman and J.A. Weiss
Solid State Comm. 16, 983 (1975)

/5.9/ B. Velicky, S. Kirkpatrick and H. Ehrenreich
Phys. Rev. 175, 747 (1968)

/5.10/ L. Hodges, R.E. Watson and H. Ehrenreich
Phys. Rev.B 5, 3953 (1972)

/5.11/ A. Bansil, H. Ehrenreich, L. Schwartz and R.E. Watson
Phys. Rev. 9, 445 (1974)

/5.12/ N.A.W. Holtzwarth and M.J.G. Lee
Phys. Cond. Matter 19, 161 (1975)

/5.13/ P.T. Coleridge, N.A.W. Holzwarth and M.J.G. Lee
Phys. Rev. B 10, 1213 (1974)

/5.14/ N.A.W. Holtzwarth
Phys. Rev. B 11, 3718 (1975)

/5.15/ J. Friedel
Berichte der Bunsengesellschaft, 76, 828 (1972)

/5.16/ A. Bansil, L. Schwartz and H. Ehrenreich
Phys. Cond. Matter 19, 39 (1975)

/5.17/ E. Wicke and G.H. Nernst
Z. Electrochem. 68, 224 (1964)

/5.18/ J. Korringa
Physica 13, 392 (1947)

/5.19/ W. Kohn and N. Rostoker
Phys. Rev. 94, 1111 (1954)

Acknowledgements

This work was carried out in the Group for Electronic Properties of the Institute für Festkörperforschung der Kernforschungsanlage Jülich GmbH.

I would especially like to thank Dr. B. Lengeler for his constant support and the many stimulating discussions during the course of the work and for his help in planning the project.

I would also like to thank Prof. Dr. W. Schilling for his interest in the work and for his support.

In addition I wish to express my thanks to Mr. J. Keppels whose technical assistance with the experiment was greatly appreciated, Mr. A. Fattah for providing the copper crystals, and Dr. K. Mika and Mr. K. Wingerath for their help with the data analysis.

Finally I would like to thank Mrs. H. Franken for typing the manuscript.